Title	Non-Equilibrium Molecular Dynamics Simulation Studies on Gas Permeation through Carbon Membranes
Author(s)	古川, 信一
Citation	大阪大学, 2000, 博士論文
Version Type	VoR
URL	https://doi.org/10.11501/3169474
rights	
Note	

Non-Equilibrium Molecular Dynamics Simulation Studies

on Gas Permeation through Carbon Membranes

Shin-ichi FURUKAWA

Division of Chemical Engineering

Department of Chemical Science and Engineering

Graduate School of Engineering Science

Osaka University

2000

Preface

This dissertation work was carried out under the supervision of Professor Tomoshige NITTA at the Division of Chemical Engineering, Department of Chemical Science and Engineering, Graduate School of Engineering Science, Osaka University from 1995 to 2000.

The objective of this work is to investigate gas permeation phenomena and separation mechanisms for carbon membranes at the molecular level by using the novel Non-Equilibrium Molecular Dynamics (NEMD) method developed in this study. The thesis consists of six chapters. Chapter 1 provides backgrounds of gas permeation through inorganic membranes and a review and fundamentals of the NEMD methods. In Chapter 2, a new NEMD method is developed and simulation results are reported that have explored the influence of the pore size and temperature on the permeation rate and separation factor. Chapter 3 deals with the effects of surface heterogeneity on gas permeation through carbon membranes having slit-shaped pores with random heterogeneous surfaces. In Chapter 4, permeation simulations are carried out for carbon membranes with belt-like heterogeneous surfaces to investigate the effects of the structurally different surface heterogeneity on gas permeation and permselectivity in comparison with the simulation results for random heterogeneous surfaces. In Chapter 5, effects of pore structures on gas permeation are investigated by using model carbon membranes with three different pore shapes composed of micro-graphite crystallites: diamond path, zigzag path and straight path. The major results of this work are summarized in Chapter 6.

The author hopes that the new molecular simulation method and molecular insights obtained in the present study would contribute to the analysis and understanding of transport phenomena through carbon membranes and in

the future to the development of molecular design systems of inorganic membranes.

Shin-ichi FURUKAWA

Division of Chemical Engineering
Department of Chemical Science and Engineering
Graduate School of Engineering Science
Osaka University
Toyonaka, Osaka 560-8531, Japan

Contests

Chapter 1
General Introduction

1.1 Motivation and Scope of the Present Work

Inorganic membranes, such as those composed of zeolite, silica gel and carbon, have several potential advantages, i.e. stability to high temperature, high pressure, and organic chemicals [Bhave, 1991; Hsieh, 1996; Burggraaf and Cot, 1996]. Therefore, gas separation processes based on the inorganic membranes have received much attention in petroleum refineries, chemical industries and power plants. In particular, development of inorganic membranes suitable for carbon dioxide removal processes has been a topic in some national projects.

In the recent decade, great progress has been achieved in developing inorganic membranes with high permselectivity [Matsukata and Kikuchi, 1997], which has brought a growing need for understanding the permeation phenomena and separation mechanisms of the membranes at the molecular level, hopefully to have some guiding principles for development of appropriate membranes suitable for separation of a specific gas mixture. Molecular simulation approaches that have been developing were considered to provide desirable knowledge on permeation through inorganic membranes.

In order to apply a molecular simulation technique to gas permeation phenomena, it was necessary to modify the conventional simulation techniques that had been developed for equilibrium systems. In the middle of 1990, Non-Equilibrium Molecular Dynamics methods, which suited for simulating the membrane permeation, were proposed [MacElroy, 1994; Heffelfinger, 1994; Furukawa, 1996]. The essential elements of these NEMD methods are the conventional molecular dynamics algorithm to make molecules move and the grand

canonical Monte Carlo algorithm [Cielinski, 1985] to keep the chemical potentials or the molecular densities in control regions with fixed volumes. The μVT-NEMD method developed by the author was first applied to the slit-shaped carbon membranes [Furukawa, 1996, 1997] and found to be a powerful tool to obtain the macroscopic properties, such as fluxes, pressures, and temperatures, and microscopic information, such as density and velocity profiles. The molecular simulation technique also makes it possible to observe the dynamical molecular behavior by simultaneous use of the computer graphics technique. The author hopes that in the near future, the time will come when the membrane design and characterization will be carried out by the molecular simulations.

The focus of this thesis is put on the investigation of permeation phenomena and separation mechanisms at the molecular level by using the μVT-NEMD method developed in this work. Before the description for the μVT-NEMD techniques, the fundamentals and some of phenomenological studies for gas transport on inorganic membranes will be explained in the next section.

1.2 Background for Gas Permeation through Inorganic Membranes

Permeation of molecules through inorganic porous membranes may be conducted by four transport mechanisms: Knudsen diffusion, capillary condensation, surface diffusion and molecular sieving [Koros and Fleming, 1993], which are schematically shown in **Fig. 1-1**. The permeation mechanism changes with a decrease in pore size of a membrane in order of Knudsen diffusion, the capillary condensation, the surface diffusion and the molecular sieving. Effective mechanisms for high permselectivity among the four may be the surface diffusion and the molecular sieving [Burggraaf and Cot, 1996].

Mass-transport through a microporous membrane may consist of five

steps as qualitatively depicted in **Figure 1-2** [Bakker, 1996].

1. Adsorption from the gas phase to the external surface.

2. Mass transport from the external surface into the pores.

3. Diffusion inside the pores.

4. Mass transport out of the pores to the external surface.

5. Desorption from the external surface to the gas phase.

In experimental studies of the mass-transport, steps 1 and 5 were generally assumed to be fast processes and other steps were considered as a lumped process. In order to explain the lumped process, the sorption-diffusion model has been used [Barrer, 1990; Uhlhorn, 1992; Kapteijn et al., 1994, 1995; de Lange et al., 1995; Shelekhin et al., 1995; Bakker et al., 1996, 1997; Keizer et al., 1998; Burggraaf, 1999]. The sorption-diffusion model describes transport phenomena in a membrane by the concepts of solubility and mobility, which is a well-known model representing separation mechanisms for organic membranes. Kapteijn et al. [1994] applied the generalized Maxwell-Stefan (GMS) theory, by adopting the surface diffusion model, to represent permeation phenomena for silicalite-1 membranes. The GMS theory provides a good rational and theoretical basis for diffusion inside porous media [Krishna, 1993]. Bakker et al. [1996, 1997] explained temperature dependence on permeation of pure light hydrocarbon gases through a silicalite-1 membrane by using the GMS model based on contribution of the surface and Knudsen diffusion for permeation. On the other hand, Nishiyama et al. [1997] proposed a simplified parallel diffusion model for permeation mechanisms of small molecules in zeolites. In the model, the total permeation in the pore was assumed to be the sum of two parallel paths which were mass flows in a gas-phase at the central region of a pore and in an adsorbed-phase along a pore wall.

The sorption-diffusion models mentioned above can describe the per-

meation rate through each experimentally synthesized membrane, but those have a few detailed information on permeation phenomena and separation mechanisms at the molecular level. In the next section, the basis and a short review of the NEMD techniques utilized for investigation of mass and energy flows are described.

1.3 Non-equilibrium molecular dynamics methods

The molecular simulation techniques, composed of the Monte Carlo (MC) and Molecular Dynamics (MD) methods [Allen and Tildesley, 1987; Frenkel and Smit, 1996], have become a powerful tool for investigating dynamic and static behavior of molecular systems. They have been utilized for investigating thermodynamic properties at equilibrium states of various molecular systems. The difference between the MC and MD methods is the way to generate system configurations. The MC method generates molecular configurations by use of random numbers and accepts them according to the probability density that is determined from a specified condition of the system, while the MD method generates configurations by calculating molecular movements through Newtonian equations of motion. The so called periodic boundary condition and minimum image convention are used to mimic the system of small number of molecules to the macroscopic ones. A schematic diagram representing the periodic boundary is shown in **Fig. 1-3** [Allen and Tildesley, 1987]. In order to apply the MD technique to the system undergoing pressure gradient, such as permeation through a membrane, it is necessary to modify the technique so that the non-equilibrium states are reproduced.

In the early 1980, the Non-Equilibrium MD (NEMD) method has been developed [Allen and Tildesley,1987; Evans and Morriss, 1984, 1990], which may be called the Hamiltonian-Driven Non-Equilibrium Molecular Dynamics

(HD-NEMD) method. The HD-NEMD method produced the non-equilibrium state by an addition of perturbation to the equations of motion. It was applied to calculate shear and bulk viscosities, [Wang and Cummings, 1993; Sarman, 1995] and thermal conductivities [Ravi and Murad, 1991]. Maginn et al. [1993] proposed a NEMD simulation method by using a different technique for the generation of a non-equilibrium state, which was called the Gradient Relaxation MD (GRMD) method. **Figure 1-4** shows schematic representation of the GRMD simulation cell. The GRMD method consisted of two equilibrium molecular simulation steps. In the first stage of a simulation, two equilibrium "subsystems" were prepared by MC and MD simulations in order to create the initial concentration gradient. In the second simulation, the MD simulation was carried out by use of the simulation cell composed of the two subsystems shown in Fig. 1-4. A transport diffusivity could be obtained by monitoring relaxation of the concentration gradient as a function of time. Therefore, by the GRMD simulation, the non-equilibrium and non-steady state was generated.

In the middle 1990, new NEMD methods were proposed which generated a non-equilibrium steady state in a simulation cell by modifying the boundaries. Therefore, they may be called the Boundary-Driven (BD-) NEMD method. The first BD-NEMD simulation was carried out by Hafskjold et al. [1993]. They investigated heat flows by using a simulation cell illustrated in **Fig. 1-5**. The simulation cell consists of two boxes arranged in mirror-image in order to satisfy the periodic boundary conditions in all directions. There are two control regions (H and C) in the simulation cell. The H-region is used for the addition of kinetic energy to the system, while the C-region is used for the removal of energy. As a consequence, a temperature gradient and an internal energy flux are generated in M-regions between the H- and C-regions. **Figure 1-6** shows profiles of temperature, density and mole fraction for a binary mixture in a half

simulation cell. The left-hand side indicates the H-region, while the opposite side is the C-region. The temperature decreased linearly from the H-region to the C-region. **Figure 1-7** shows profiles of total energy flux where the flux in the M-region was almost constant. This observation indicated that the simulation run achieved the steady state.

Heffelfinger and Swol [1994] proposed a different BD-NEMD technique, which was called the Dual Control Volume Grand Canonical MD (DCV-GCMD). **Figure 1-8** shows a schematic diagram of a simulation cell used for calculations of counter-current diffusion in a gas phase. Instead of using the periodic boundary conditions in the diffusion direction, two confining walls were placed at each end of the simulation cell. The DCV-GCMD method generates a non-equilibrium steady state by using dual control volumes where the chemical potentials are kept constant at two specified values by use of the grand canonical algorithm. The manipulation of molecular insertions and destructions in the two control volumes was applied at each MD time step. The number of molecular insertion and destruction operations has to be large enough to keep the chemical potential in each control volume at the given value, though it is desirable to be as small as possible to minimize CPU time. In their study, the number of the operations was set at 50. **Figure 1-9** shows density profiles in the simulation cell for a binary gas mixture. The density gradients were generated between each control volume. The density peaks at each end of the simulation cell were due to adsorption of the fluid on the wall. In the same year, MacElroy [1994] reported the first simulation of permeation of hard spheres across thin microporous membranes by using a similar technique of the DCV-GCMD method. Cracknell et al. [1995] employed the DCV-GCMD method for investigation of transport phenomena in the slit-shaped micropore. Furukawa et al. [1996] developed the μVT-NEMD method based on the BD-NEMD proposed by Hafskjold

et al. [1993], which generated non-equilibrium states having a difference in density for simulations of membrane permeation. Recently, Thompson and Heffelfinger [1999] have developed a modified DCV-GCMD method, which uses the difference in pressure, instead of the chemical potential, as the driving force.

It is worthy of noting that Heffelfinger and Ford [1998a and b] developed a massively parallel algorithm for the DCV-GCMD method, which runs on a super computer with parallel processors. The algorithm is essential if the NEMD simulations are applied to more computationally demanding systems and problems in order to shorten the calculation time.

1.4 Applications of the molecular simulations to studies of permeation phenomena and separation mechanisms for inorganic membranes

In the primary applications of the BD-NEMD methods to simulations of membrane permeation, simple models for fluids and membranes were chosen. MacElroy [1994] investigated permeation phenomena for hard-sphere dense fluid through the simple microporous membrane containing pores approximately four fluid particle diameters in size by using their GCMD method. The transport mechanism was described as slip flow rather than viscous shear flow in their simulation conditions.

Pohl et al. [1996, 1999] simulated gas permeation through thin silicalite membranes by the DCV-GCMD method. The permeation mechanism of He, H_2, CH_4 and Ar gases through the micorporous silica membrane was described as Knudsen diffusion. The permeabilities calculated from the simulation results were reported to be approximately 40 times greater than the experimental values. They ascribed this result to the distinction between the membrane struc-

tures of experiments and simulations. It is noted that the membrane model used in the permeation simulations is much thinner than membranes in the experiments since there is a limit in the available number of the molecules dealt with in the computer.

Takaba and co-workers [1996, 1997, 1998] investigated permeation phenomena and separation mechanisms of gases through several inorganic membranes, such as those composed of MgO, silicalite or zeolite, by the conventional MD with initial density gradient. In the case of CO_2 separation from the CO_2/N_2 gas mixture using the MgO membrane, they ascertained that there was an optimal range of affinity strength between permeating molecules and the membrane for the supreme separation because the much stronger affinity prevents the surface diffusion [Takaba, 1996]. Also, they obtained a new insight for molecular behavior in the membrane by using computer graphics, which is one of advantages of the molecular simulation. **Figure 1-10** shows molecular trajectories of *n*-butane permeation for a ZSM-5 membrane [Takaba, 1997]. They observed that the molecules permeated mainly through straight channels at low temperature, while those entered not only straight channels but also sinusoidal channels for diffusion at high temperature.

Furukawa et al. investigated the permeation of pure and mixed-gases through carbon membranes with different pore surfaces or different pore shapes [1996, 1997a, 1997b, 1999, 2000]; the results will be described in detail in Chapters 2 to 5.

MacElroy and Boyle [1999] employed NEMD simulations to investigate the transport of binary mixtures through a model carbon membrane of varying thickness. In their study, it was found that viscous flow contributions to the fluxes of the individual components of the mixture could be negligible, and that the cross-coefficients of diffusion appeared to play a relatively minor role in the

membrane separation process. As another information from the NEMD simulations, it was found that pore entrance/exit effects need to be taken into consideration for membrane design in the case of considerable thin membranes.

The applications of the NEMD technique to investigation of permeation phenomena and separation mechanisms have just begun. From now on, the molecular simulations need to deal with permeation systems close to the reality in order to investigate transport phenomena occurring in experimental systems.

In this thesis, there are two main topics, which are (1) development of the NEMD method suitable for membrane permeation and (2) investigation of permeation phenomena and separation mechanisms at the molecular level by using the NEMD technique. Permeation simulations are carried out for pure and mixed-gases composed of CH_4 and/or C_2H_6 through several model carbon membranes.

In Chapter 2, the μVT-NEMD method, which generates non-equilibrium states by a density difference as the driving force, is described in detail. By use of the μVT-NEMD method, the permeation simulations are carried out for slit-shaped carbon membranes with flat pore walls. Effects of the pore size and temperature on permeation fluxes and separation factors are investigated.

In Chapter 3, effects of surface heterogeneity on permeation phenomena and separation mechanisms are investigated by permeation simulations for slit-shaped carbon membranes with random heterogeneous surfaces, which are made by randomly removing a certain number of carbon atoms of the first graphite basal plane.

In Chapter 4, the permeation simulations are carried out for the slit-shaped carbon membranes with belt-like heterogeneous surfaces, in order to investigate effects of unavoidable potential barriers for permeation on permeation phenomena and separation mechanisms. The belt-like heterogeneous sur-

faces are made by removing carbon atoms on the first layer of the graphite basal plane in a line vertically to the permeation direction.

Chapter 5 is focused on effects of the pore shape on the permeation and separation of gases by using three model pores different in shape. They are characterized by the shape of cross sections: the diamond, zigzag and straight paths, all are composed of microcrystals of graphite basal planes.

Finally the major results obtained in this work are summarized in Chapter 6.

Reference

Allen, M.P. and D.J. Tildesley; Computer Simulation of Liquids, Clarendon Press, Oxford, 1987

Bakker, W.J.W., F. Kapteijn, J. Poppe and J.A. Moulijn; "Permeation characteristics of a metal-supported silicalite-1 zeolite membrane," *J. Mem. Sci.*, **117**, 57-78 (1996)

Bakker, W.J.W., J.P. van den Broeke, F. Kapteijn and J.A. Moulijn; "Temperature dependence of one-component permeation through a silicalite-1 membrane," *AIChE J.*, **43**, 2203-2214 (1997)

Barrer, R.M.; "Porous crystal membranes; " *J. Chem. Soc. Faraday Trans.*, **86**, 1123-1130 (1990)

Bhave, R.R. (ed.); Inorganic Membranes, Synthesis, Characterization, and Application, Van Nostrand Reinhold, New York, USA, 1991.

Burggraaf, A.J. and L. Cot (Ed.); Fundamentals of Inorganic Membrane Science and Technology, Elsevier, Amsterdam, 1996.

Burggraaf A.J.; "Single gas permeation of thin zeolite (MFI) membranes: theory and analysis of experimental observations," *J. Mem. Sci.*, **155**, 45-65 (1999)

Cielinski, M.M., M.S. Thesis, University of Maine, Orono, USA (1985)

Cracknell, R.F., D. Nicholson and N. Quirke; "Direct molecular dynamics simulation of flow down a chemical potential gradient in a slit-shaped micropore," *Phys. Rev. Lett.*, **74**, 2463-2466 (1995)

Evans, D.J. and G.P. Morriss; "Non-newtonian molecular dynamics," *Phys. Rep.*, **1**, 297-344 (1984)

Evans, D.J. and G.P. Morriss; Statistical Mechanics of nonequilibrium liquids, Academic Press, London. 1990

Frenkel, D. and B. Smit; Understanding Molecular Simulation, From Algorithm

to Applications, Academic Press, San Diego, 1996

Furukawa, S., T. Shigeta and T. Nitta; "Non-equilibrium molecular dynamics for simulating permeation of gas mixtures through nanoporous carbon membrane," *J. Chem. Eng. Japan*, **29**, 725-728 (1996)

Furukawa, S. and T. Nitta; "Computer simulation studies on gas permeation through nanoporous carbon membranes by non-equilibrium molecular dyanmics," *J. Chem. Eng. Japan*, **30**, 116-122 (1997a)

Furukawa, S., K. Hayashi and T. Nitta; "Effects of surface heterogeneity on gas permeation through slit-like carbon membranes by non-equilibrium molecular dynamics simulation," *J. Chem. Eng. Japan*, **30**, 1107-1112 (1997b)

Furukawa, S., T. Sugahara and T. Nitta; "Non-equilibrium MD studies on gas permeation through carbon membranes with belt-like heterogeneous surfaces, *J. Chem. Eng. Japan*, **32**, 223-228 (1999)

Furukawa, S. and T. Nitta; "Non-equilibrium molecular dynamics simulation studies on gas permeation across carbon membranes with different pore shape composed of micro-graphite crystals," *J. Mem. Sci.*, (2000) submitted

Hafskjold, B., T. Ikeshoji and S.K. Ratkje; "On the molecular mechanism of thermal diffusion in liquids," *Molec. Phys.*, **80**, 1389-1412 (1993)

Heffelfinger, G.S. and F. van Swol; "Diffusion in Lennard-Jones fluids using dual control volume grand canonical molecular dynamics simulation (DCV-GCMD)," *J. Chem. Phys.*, **100**, 7548-7552 (1994)

Heffelfinger, G.S. and D.M. Ford; "Massively parallel dual control volume grand canonical molecular dynamics with LADERA I. Gradient driven diffusion in Lennard-Jones fluid," *Mole. Phys.*, **94**, 659-671 (1998a)

Heffelfinger, G.S. and D.M. Ford; "Massively parallel dual control volume grand canonical molecular dynamics with LADERA II. Gradient driven through polymers," *Mole. Phys.*, **94**, 673-683 (1998b)

Hsieh, H.P.; Inorganic Membranes for Separation and Reaction, Elsevier, Amsterdam, 1996.

Kapteijn, F., W.J.W. Bakker, G. Zheng and J.A. Moulijn; "Temperature- and occupancy-dependent diffusion of n-butane through a silicalite-1 membrane," *Microporous Mater.*, **3**, 227-234 (1994)

Kapteijn, F., W.J.W. Bakker, G. Zheng, J. Poppe and J.A. Moulijn; "Permeation and separation of light hydrocarbons through a silicalite-1 membrane Application of the generalized Maxwell-Stefan equations," *Chem. Eng. J.*, **57**, 145-153 (1995)

Keizer, K., A.J. Burggraaf, Z.A.E.P. Vroon and H. Verwij; "Two component permeation through thin zeolite MFI membranes," *J. Mem. Sci.*, **147**, 159-172 (1998)

Koros, W.J. and G.K. Fleming; "Membrane-based gas separation," *J. Mem. Sci.*, **83**, 1-80 (1993)

Krishna, R.; "A unified approsch to the modelling of intraparticle diffusion in adsorption processes," *Gas Sep. Purif.*, **7**, 91-104 (1993)

de Lange, R.S.A., K. Keizer and A.J. Burggraaf; "Analysis and theory of gas transport in microporous sol-gel derived ceramic membranes," *J. Mem. Sci.*, **104**, 81-100 (1995)

MacElroy, J.M.D.; "Nonequilibrium molecular dynamics simulation of diffusion and flow in thin microporous membranes," *J. Chem. Phys.*, **101**, 5274-5280 (1994)

MacElroy, J.M.D. and M.J. Boyle; "Nonequilibrium Molecular Simulation of a Model Carbon Membrane Separation of CH_4/H_2 Mixtures," *Chem. Eng. J.*, **74**, 85-97 (1999)

Maginn, E.J., A.T. Bell and N. Theodorou; "Transport diffusivity of methane in silicalite from equilibrium and nonequilibrum simulations," *J. Phys. Chem.*,

97, 4173-4181 (1993)

Matsukata, M. and E. Kikuchi; "Zeolitic membranes: synthesis, properties and prospects," *Bull. Chem. Soc. Japan*, **70**, 2341-2356 (1997)

Mizukami, K., H. Takaba, N. Ito, M. Kubo, A. Fahmi and A. Miyamoto; "Permeability of Ar and He through an inorganic membrane; A molecular dynamics study," *App. Sur. Sci.*, **119**, 330-334 (1997)

Nishiyama, N., K. Ueyama and M. Matsukata; "Gas permeation through zeolite-alumina composite membranes," *AIChE J.*, **43**, 2724-2730 (1997)

Pohl, P.I., G.S. Heffelfinger and D.M. Smith; "Molecular dynamics computer simulation of gas permeation in thin silicalite membranes," *Molec. Phys.*, **89**, 1725-1731 (1996)

Pohl, P.I. and G.S. Heffelfinger; "Massively parallel molecular dynamics simulation of gas permeation across porous silica membranes," J. Mem. Sci., **155**, 1-7 (1999)

Ravi, P. and S. Murad; "Thermal conductivity of continuous, semi-continuous and discrete mixtures using nonequilibrium molecular dynamics," *Mol. Sim.*, **7**, 325-334 (1991)

Sarman, S.; "Nonequilibrium molecular dynamics of liquid crystal shear flow," *J. Chem. Phys.*, **103**, 10378-10386 (1995)

Shelekhin, A.B., A.G. Dixon and Y.H. Ma; "Theory of gas diffusion and permeation in inorganic molecular-sieve membranes," *AIChE J.*, **41**, 58-67 (1995)

Takaba, H., K. Mizukami, M. Kubo, A. Stirling and A. Miyamoto; "The effect of gas molecule affinities on CO_2 separation from the CO_2/N_2 gas mixture using inorganic membranes as investigated by molecular dynamics simulation," *J. Mem. Sci.*, **121**, 251-259 (1996)

Takaba, H., R. Koshita, K. Mizukami, Y. Oumi, N. Ito, M. Kubo, A. Fahmi and A. Miyamoto; "Molecular dynamics simulation of *iso-* and *n*-butane perme-

ations through a ZSM-5 type silicalite membrane," *J. Membrane Sci.*, **134**, 127-139 (1997)

Takaba, H., K. Mizukami, M. Kubo, A. Fahmi and A. Miyamoto; "Permeation dynamics of small molecules through silica membranes: Molecular dynamics study," *AIChE J.*, **44**, 1335-1343 (1998)

Thompson, A.P. and G.S. Heffelfinger; "Direct molecular simulation of gradient-driven diffusion of large molecules using constant pressure," *J. Chem. Phys.*, **110**, 10693-10705 (1999)

Uhlhorn, R.J.R., K. Keizer and A.J. Burggraaf; "Gas transport and separation with ceramic membranes. Paret I. Multilayer diffusion and capillary condensation," *J. Mem. Sci.*, **66**, 259-269 (1992)

Wang, B.Y. and P.T. Cummings; "Non-equilibrium molecular dynamics calculation of the shear viscosity of carbon dioxide/ethane mixtures," *Mol. Sim.*, **10**, 1-11 (1993)

(a) Knudsen diffusion
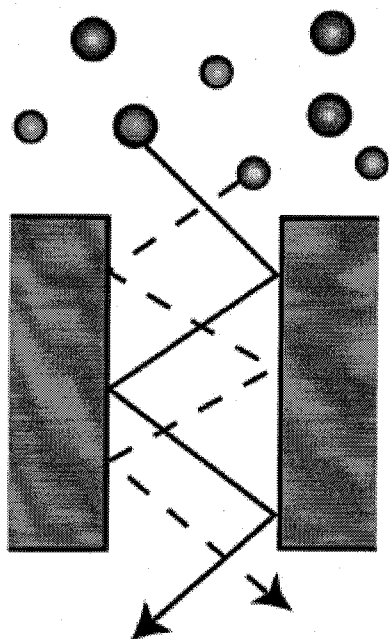
(b) capillary condensation
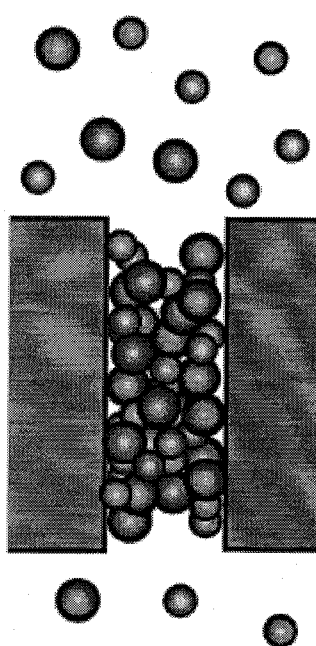
(c) surface diffusion
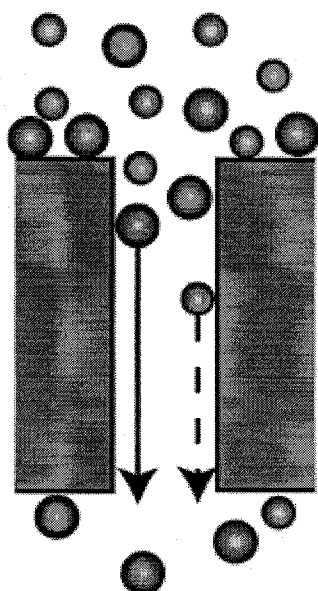
(d) molecular sieving
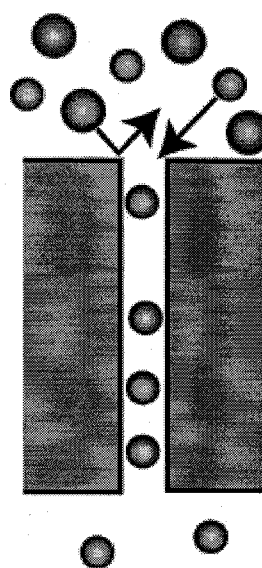
Figure 1-1   Schematic diagrams of four transport mechanisms for porous
membranes

①　　②　　　　③　　　④　⑤
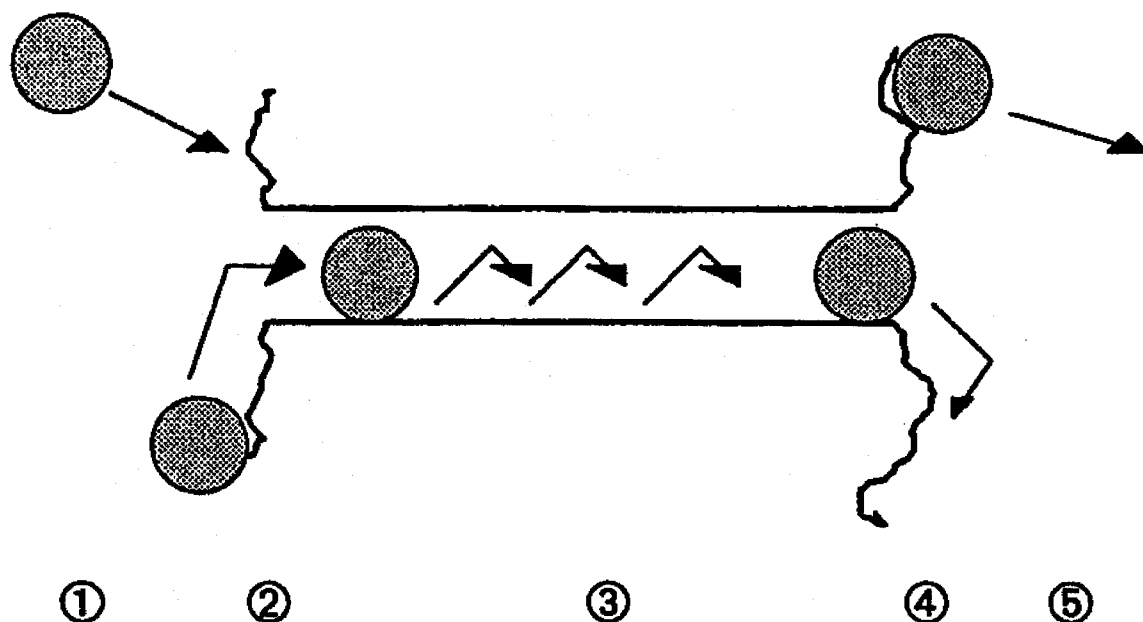
Figure 1-2　Schematic diagrams of a mass-transfer model for an inorganic membrane: steps 1, 2, 3, 4 and 5 , respectively, adsorption from the gas phase to the external surface, mass transport from the external surface into the pores, diffusion inside the pores, mass transport out of the pores to the external surface and desorption from the external surface to the gas phase [Bakker, 1996]
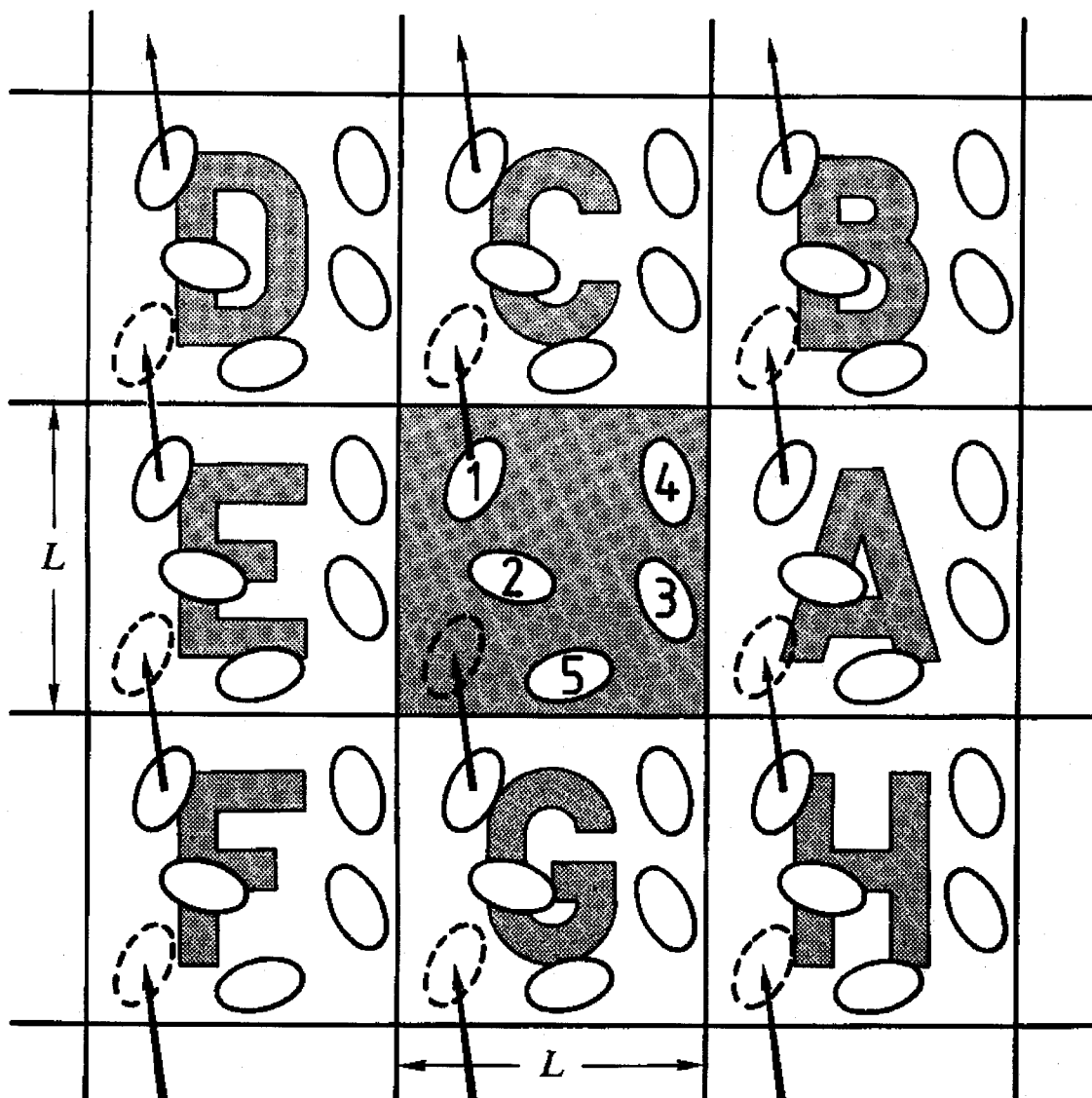
Figure 1-3   Schematic diagram of a two-dimensional periodic boundary system
[Allen and Tildesley, 1987]

i1   i2

```
      Periodic Image          Parent Cell          Periodic Image
```
y=0   y=L

-x
 y
z

Concentration Profile, t=0

Concentration Profile, t=t'
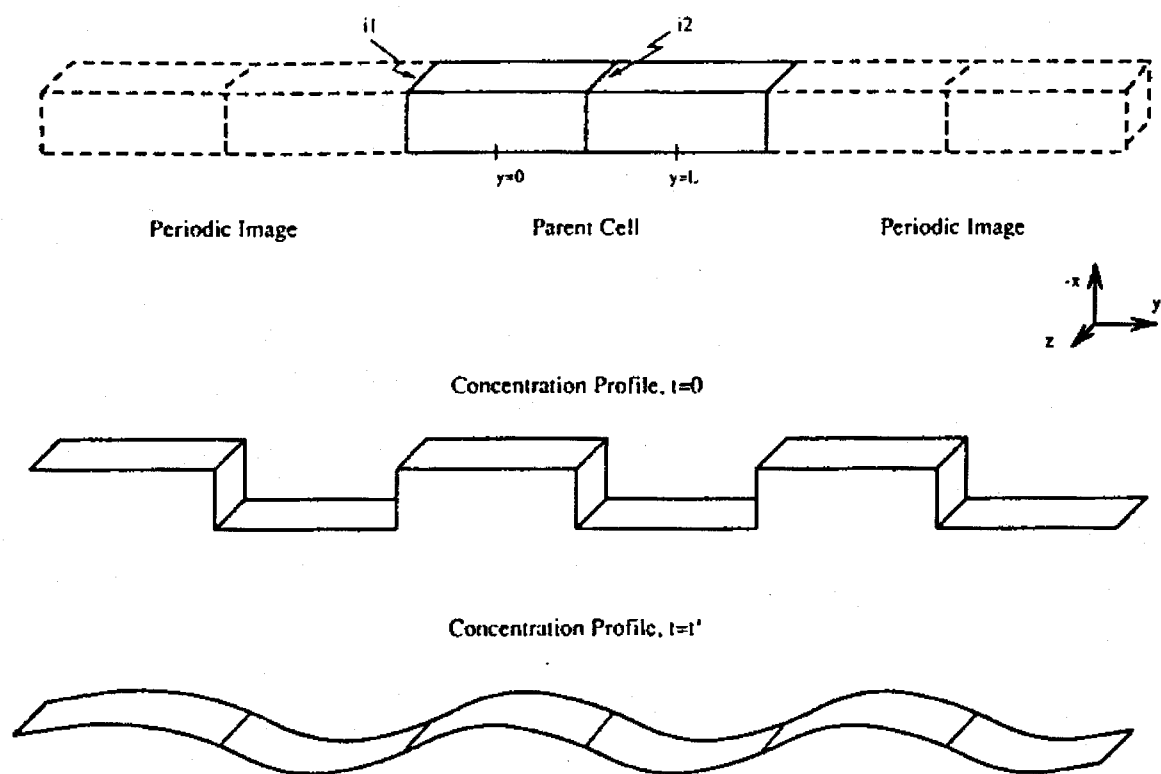
Figure 1-4   Schematic representation of the GRMD simulation cell, with periodic images shown along the direction of the concentration gradient. Shown below this are two hypotential concentration profiles at initial time and at some later time. [Maginn, 1993]
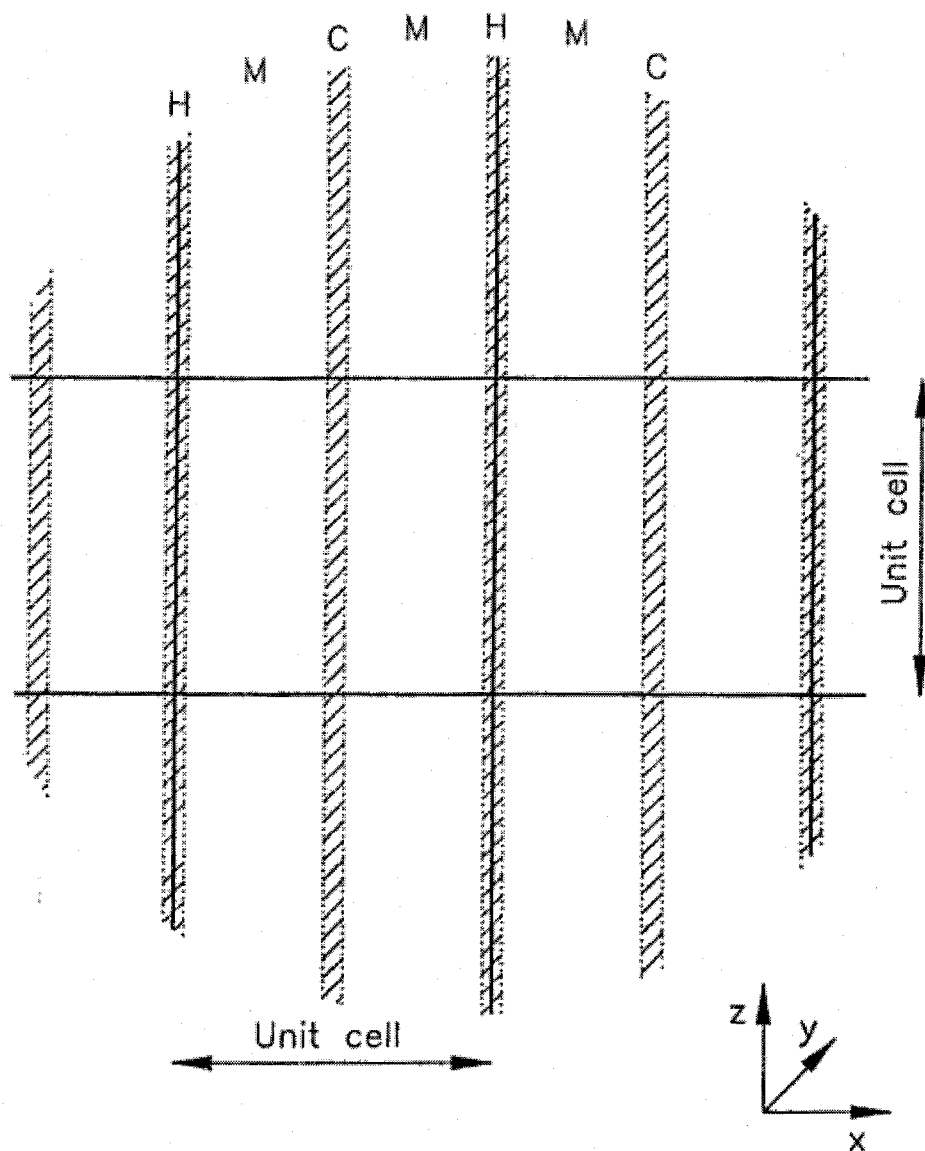
Figure 1-5 Layout of the cubic system showing the periodic boundary conditions and the hot (H), cold (C), and middle (M) regions [Hafskjold, 1993]
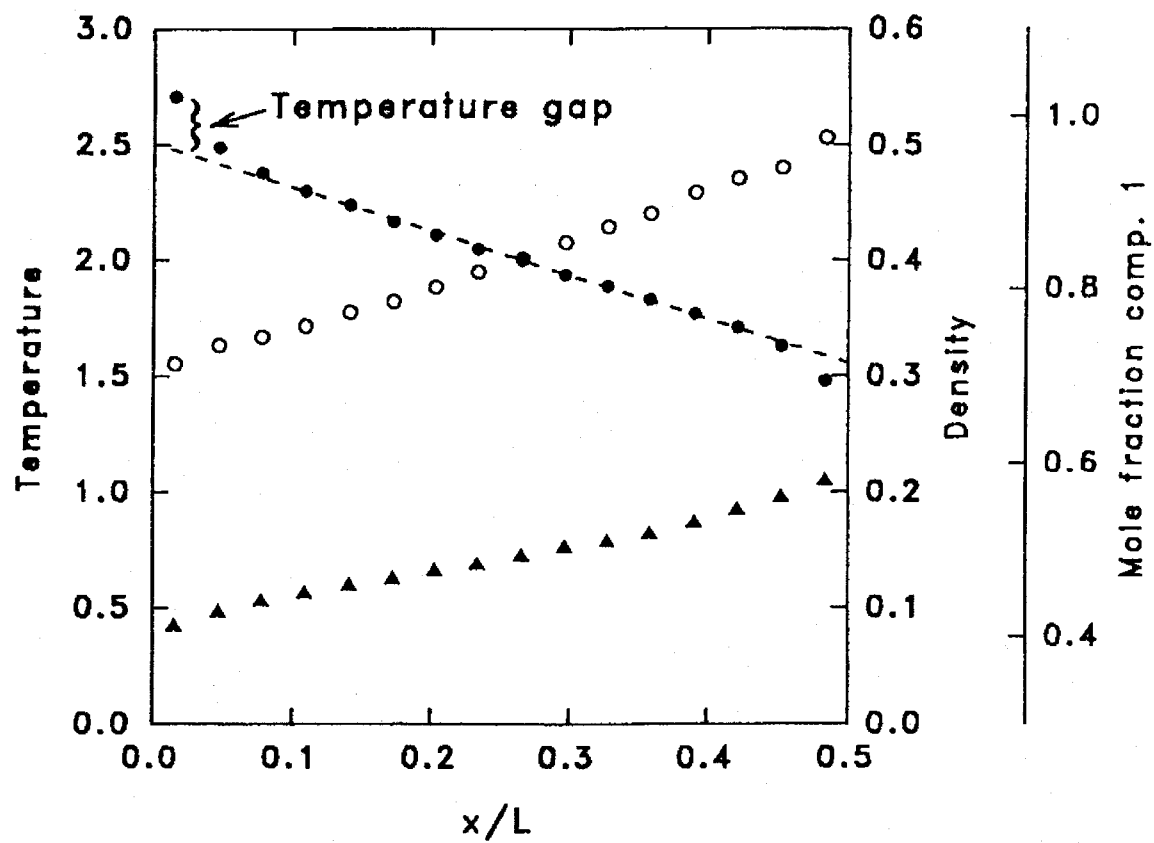
Figure 1-6   Temperature (●), density (○), and mole fraction of component 1
(heavy component) (△) as functions of simulation cell length in
the *x*-direction [Hafskjold, 1993]
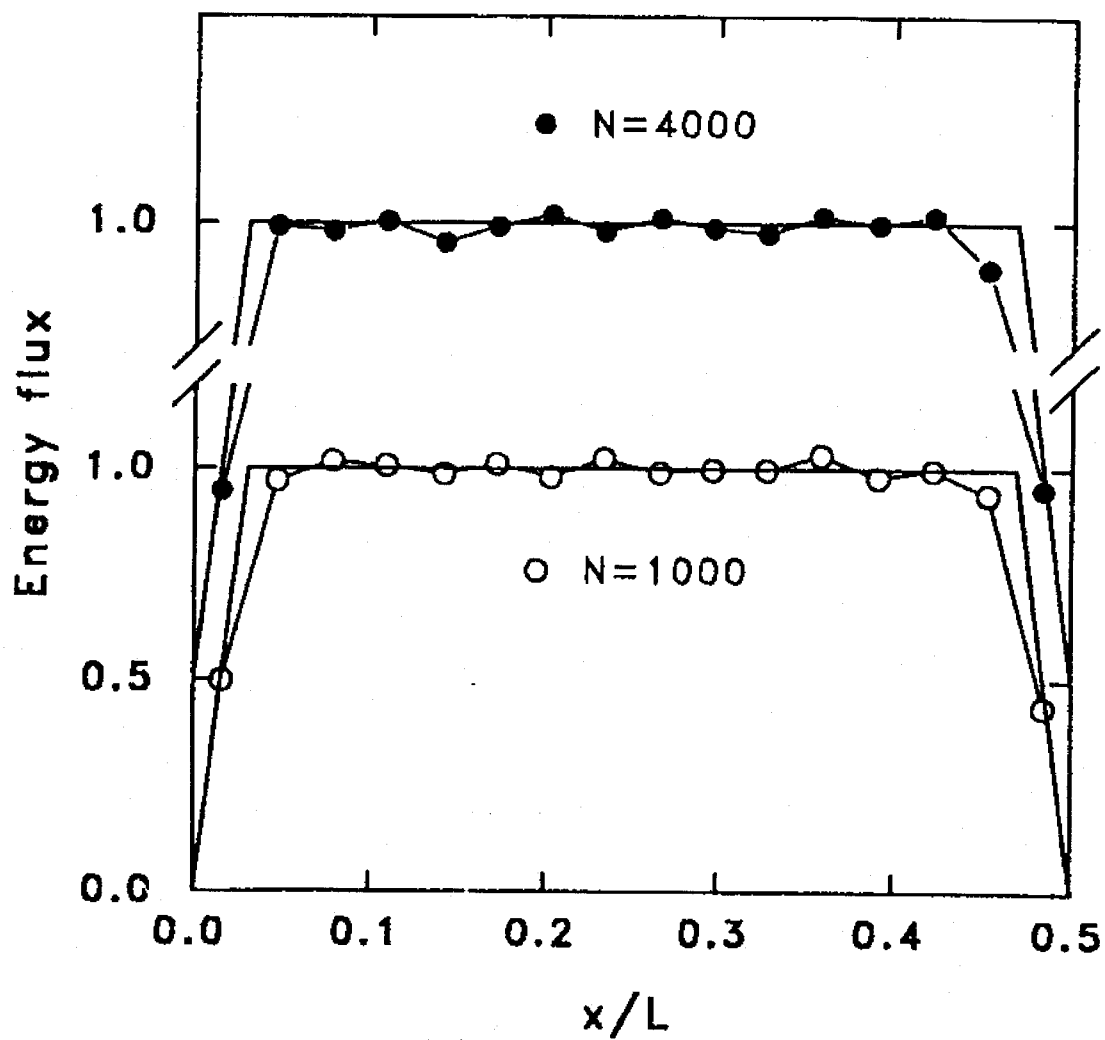
Figure 1-7   Total energy flux computed with a non-cubic 1000 particle system
and a cubic 4000 particle system as function of length of simulation
cell in the x-direction [Hafskjold, 1993]
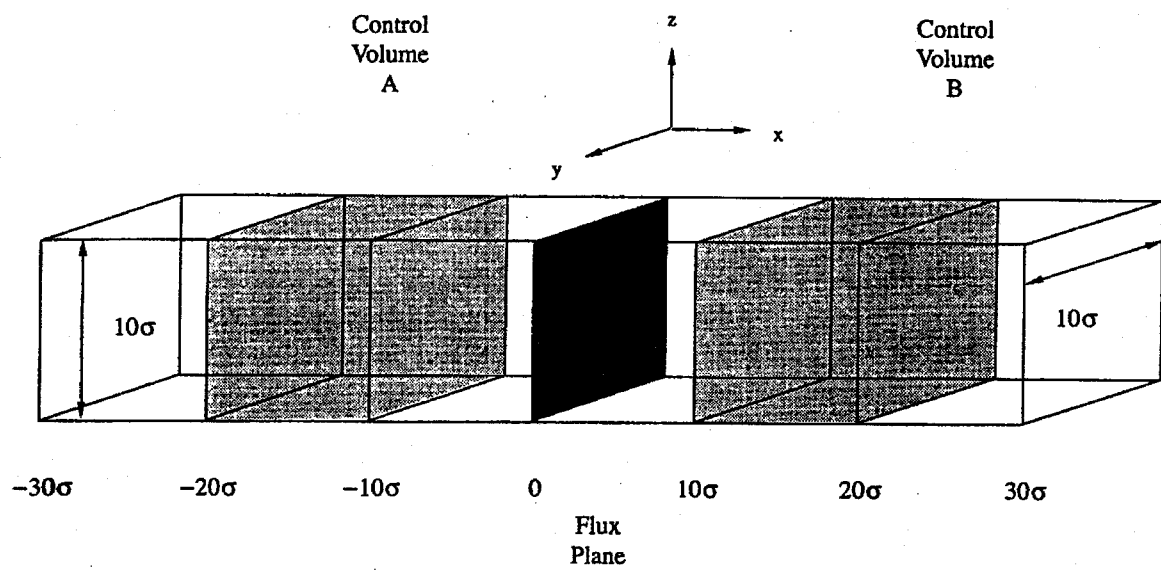
Figure 1-8   Schematic drawing of the DCV-GCMD system [Heffelfinger and Swol, 1994]
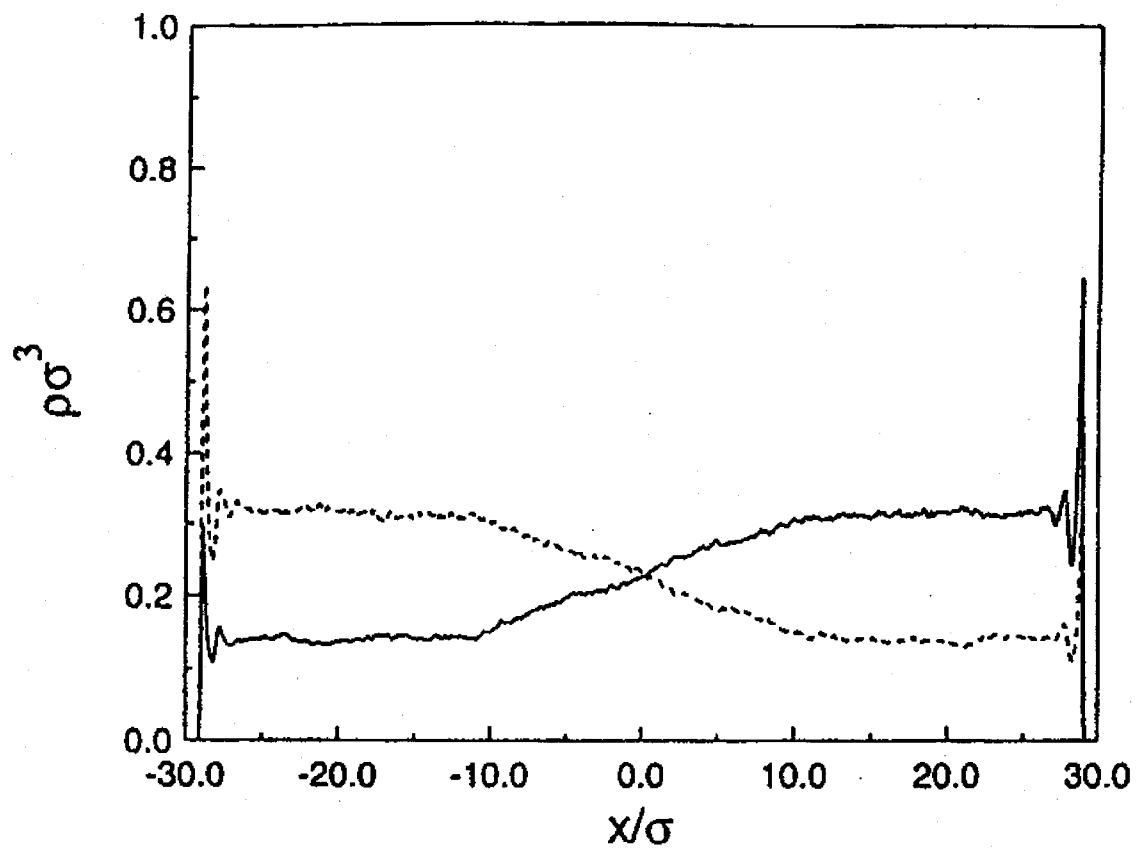
Figure 1-9   Density profiles in the simulation cell. The x coordinates of control
volumes are -20 and -10, and 10 and 20 [Heffelfinger and Swol,
1994]
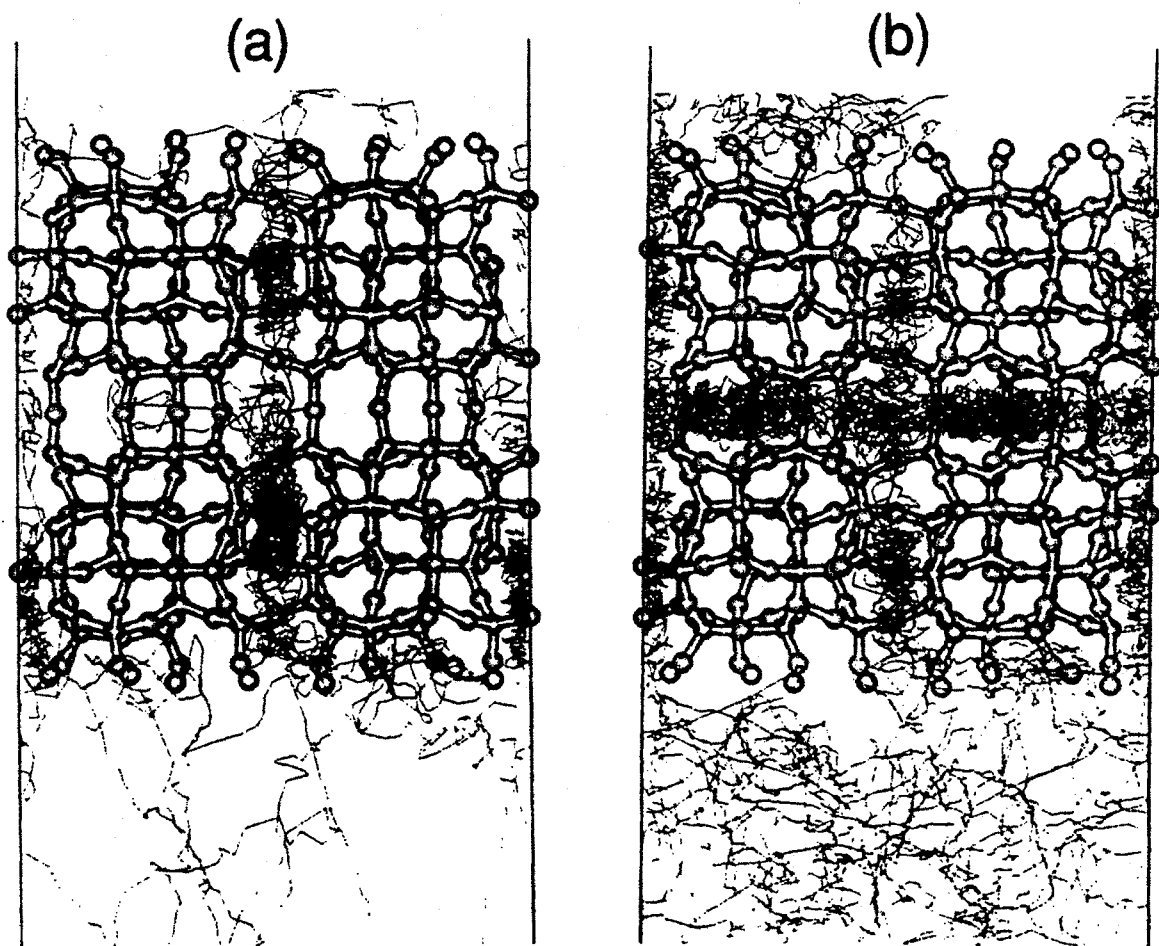
Figure 1-10 Molecular trajectories of *n*-butane for a ZSM-5 membrane at different temperatures: (a) 373 K, (b) 773 K, from side view (100) [Takaba, 1997]

Chapter 2
Development and Applications of
Non-Equilibrium Molecular Dynamics Method
for Simulation of Membrane Permeation

2.1 Introduction

Inorganic porous membranes have received much attention because of their potential advantages for gas separations: the stability to high temperature and high pressure, the high selectivity, and the high rate of transport [Kimura, 1994]. According to Uhlhorn and Burggraaf [1991], the most promising direction is the development of microporous membranes with pore sizes between 0.5 and 2.0 nm. They also pointed out that the important mechanisms of this kind of membranes are molecular sieving and activated surface transport since high selectivity is expected even at high temperatures through these permeation mechanisms.

Two types of microporous carbon membranes have been reported: the molecular sieving membranes [Chen and Yang, 1994; Suda and Haraya, 1995] and nanoporous membranes with selective adsorption followed by surface diffusion [Rao and Sircar, 1993]. The paper of the latter carbon membranes firstly demonstrated interesting characteristics that selectivities of propane and butane to hydrogen increased much more than the ratios of pure gas permeabilities. Their data are considered to suggest that competitive adsorption can play a significant role in permeation through microporous membranes.

Computer simulation techniques have been widely used for studying pVT-relations, phase equilibria and transport phenomena, by connecting the molecular information to both macroscopic properties and microscopic struc-

tures [Allen, 1987]. The Non-Equilibrium Molecular Dynamics (NEMD), which has become getting popular in recent years, is the most appropriate technique for simulating the permeation phenomena since permeation occurs through a membrane with two ends exposed to fluids at different pressures. Theoretical background and simulation algorithms of NEMD were reviewed in the text of Evans and Morriss [1990]. Recently, Ikeshoji and Hafskjold [1993, 1994] developed a new NEMD algorithm, so called the Boundary-Driven NEMD (BD-NEMD), which was attractive since the algorithm was simple and easy to extend to heterogeneous systems, such as pores with wall surfaces.

This chapter is firstly described details of the μVT-NEMD method and the permeation model characterized by the slit-shaped pores composed of energetically homogeneous plane surfaces. Next, the simulated results are provided for permeation fluxes, density profiles and the permselectivities to see how they are affected by the slit width and the temperature. Discussion will be given mainly from the viewpoint of adsorption effects on gas permeation since the present permeation model has been constructed under the assumption of the local adsorption equilibrium with feed and permeating gases at two sides of the carbon membrane.

2.2 Simulation Method

2.2.1 Simulation cell for the μVT-NEMD

Figure 2-1 shows the schematic diagram of the simulation cell used in the present work. The elemental cell is a rectangular box having sides L_x, L_y, and L_z. The parallel wall surfaces are located on the top and the bottom xy-planes as shown in the figure. L_z is the distance between two surfaces passing through the carbon centers of the basal planes exposing directly to the pore

space. The cell is divided into $2n$ subcells in the x-direction; subcells No. 1 and $2n$ are presumed to be high density (called H-region) while subcells No. n and $n+1$ to be low density (L-region). Other subcells are called M-region. The membrane thickness L is half length of side L_x. In the x- and y-directions, the periodic boundaries [Allen and Tildesley, 1987] are used for molecular moves and calculations of intermolecular forces. In the z-direction, molecules are confined inside the box since the two walls are modeled to be semi-infinite. The pore width W_p is defined as the distance subtracted from L_z by σ_{ss}, the van der Waals diameter of carbon atom consisting of the wall surface and used for the specification of pore size.

The heart of the μVT-NEMD is to maintain the density (ρ_p) and the composition (x_1) in the H-region at specified values that are in equilibrium with the bulk feed gas at a given pressure. In the present work, the pressure in the H-region is set at $P_H = 0.5$ MPa. The values for ρ_p and x_1 have been determined by using the μVT-MC method [Allen and Tildesley, 1987; Nitta and Yoneya, 1995] before starting the NEMD calculations. The chemical potential of component k in fluid phase, which is required in the μVT-MC simulation, is calculated as

$$\mu_k^* = \mu_k / kT + 3\ln\left(\Lambda_k / \sigma_{11}\right) = \ln\left(y_k \rho_f^*\right) \tag{2-1}$$

where Λ_k is the thermal de Broglie wavelength and ρ_f^* ($= \sigma_{11}^3 \rho_f = \sigma_{11}^3 P_H/kT$) is the reduced density of bulk gas at pressure P_H. The ideal gas is presumed in Eq. (2-1).

2.2.2   The μVT-NEMD

The leap-frog method of Verlet [Allen and Tildesley, 1987] was used for

the NEMD calculation. The temperature of wall surfaces was presumed to be the same since the thermal conductivity of graphitic carbon is high. The molecular velocities are rescaled independently in three directions, v_x, v_y and v_z, at each time step so as to keep the temperature of molecules in each subcell to be at a specified value (T). Let v_i and v_i', respectively, denote the velocity and the rescaled velocity of i-th molecule in one direction, then v_i' in the L-th subcell is calculated from v_i as

$$v_i' = v_i \left(\frac{1}{2} N^{(L)} kT \right) \bigg/ \left(\frac{1}{2} \sum_{j \in (L)} m_j v_j^2 \right) \qquad (2\text{-}2)$$

where $N^{(L)}$ is the number of molecules in the L-th subcell and m_j is the mass of j-th molecule.

Another velocity correction was made at each 20 time steps so as to set the total momentum at zero ($\sum_i m_i v_i = 0$). The rescaled velocity v for this correction is calculated as

$$v_i' = v_i - \left(\sum_i m_i v_i \right) \bigg/ N m_i \qquad (2\text{-}3)$$

where N is the total number of molecules in a simulation box.

The time step was 0.01 ps. The 30,000 steps were discarded and the next 30,000 steps were collected in order to have good statistics. The length L_y was chosen so as to keep 500 - 2,000 molecules in the box when a stationary state has reached.

For each NEMD calculation step, densities of each component in the H-region are kept at the values that are in equilibrium with the feed gas. The insertion and destruction algorithms of the μVT-MC method are implemented for this purpose, i.e. a molecule is created at a random position in the H-region or a randomly selected molecule in the H-region is removed. The creation or destruction trial of a molecule is accepted with a probability P_{create} or P_{destr} as

$$P_{create} = \min\left\{1, \frac{z_{i,H} V_H^*}{N_{i,H}+1} \exp(-\beta\Phi_i)\right\} \tag{2-4}$$

$$P_{destr} = \min\left\{1, \frac{N_{i,H}}{z_{i,H} V_H^*} \exp(\beta\Phi_i)\right\} \tag{2-5}$$

$$\Phi_i = \sum_j \phi_{ij}(r) + \sum_s \phi_{is}(r) \tag{2-6}$$

where Φ_i is the potential energy of the trial molecule i, $\phi_{ij}(r)$ and $\phi_{is}(r)$ the potential energies between fluid molecules i and j and molecule (i) -membrane surface (s), respectively, $z_{i,H} = \exp(\mu_i^*) / \Lambda_i^3$ the absolute activity, $V_H^* = V_H / \sigma_{11}^3$ the reduced volume of the H-region, $N_{i,H}$ the number of molecules in the H-region, and $\beta = 1 / kT$. When molecules are inserted in the H-region, their velocities are allotted to a certain value around the specified temperature by use of random numbers or the Gaussian distribution, and then the temperature corrections are made for the subcell. These operations are repeated until the density in the H-region becomes at a given value. The molecules which enter into the L-region are removed immediately.

2.2.3 Potential model

The model system is a binary mixture of methane and ethane diffusing through the slit-shaped pores composed of graphite planes. The 12-6 Lennard-Jones (LJ) potential is used for representing intermolecular interactions between molecules.

$$\phi_{ij}(r) = 4\varepsilon_{ij}\left[\left(\frac{\sigma_{ij}}{r}\right)^{12} - \left(\frac{\sigma_{ij}}{r}\right)^{6}\right] \tag{2-7}$$

where r is the distance between molecules i and j and ε_{ij} and σ_{ij} are potential parameters for a pair of i and j. The 10-4-3 potential is used for interactions between a molecule and a wall surface [Steele, 1974].

$$\phi_{is}(z) = 4\pi A_{is}\left[\frac{2}{5}\left(\frac{\sigma_{is}}{z}\right)^{10} - \left(\frac{\sigma_{is}}{z}\right)^{4}\right] - \frac{\sigma_{is}^{4}}{3\Delta(z + 0.61\Delta)^{3}} \tag{2-8}$$

where z is the distance between molecule i and the pore wall, A_{is} $(= \varepsilon_{is}\sigma_{is}^{2}/a_{s})$ a constant, a_{s} the surface area of graphite basal unit, and Δ the spacing between adjacent graphite basal planes. The above potential is called a structureless surface model, where the surface exerts a force on each molecule in the direction perpendicular to the surface and totally no force in two horizontal directions.

The LJ parameters used in the present work are the same as those used in the previous works for calculating the adsorption isotherms in slit-shaped

pores, for pure methane and ethane [Nitta, 1993, 1995] and for mixed-gases [Nozawa and Nitta, 1993]. The cross parameters are calculated from the Lorentz-Berthelot rule: that is, the geometric mean for ε_{ij} and the arithmetic mean for σ_{ij}.

2.2.4   Mass and number fluxes

The mass fluxes of component k downward in the x-direction is calculated in each subcell as

$$j_k^{(L)} = \frac{1}{V^{(L)}} \left\langle \sum_{i \in k} m_i \left(v_{x,i}^{(L)} - v_{x,0} \right) \right\rangle \tag{2-9}$$

where $V^{(L)}$ is the volume of the L-th subcell, $v_{x,i}^{(L)}$ the velocity of i-th molecule in the L-th subcell and $v_{x,0}$ the barycentric velocity of the system. The number flux of component k is calculated as

$$J_k^{(L)} = j_k^{(L)} / m_k \tag{2-10}$$

In the μVT-MC and the μVT-NEMD calculations, dimensionless variables (denoted by superscript *) reduced by the parameters of methane (component 1) were used. The relation between the mass flux and the number flux is given as

$$J_k^{(L)*} = j_k^{(L)} \frac{\sigma_{11}^3}{m_k} \left(\frac{m_1}{\varepsilon_{11}} \right)^{0.5} = \frac{j_k^{(L)*}}{m_k^*} \tag{2-11}$$

2.3 Results and Discussion

Since the proposed μVT-NEMD method is novel, simulations of pure gas permeation were first conducted by choosing ethane for a permeating gas since ethane was the dominant component in pores for permeation of a mixture of methane and ethane. Simulations of pure ethane permeation were performed at $T = 298$ K and $\Delta P = 0.5$ MPa by varying the slit width $W_p{}^*$. The membrane thickness (diffusion length) L was fixed to 25.03 nm after several trials.

2.3.1 Permeation of pure ethane

Figure 2-2 shows snapshots of ethane configurations in pores of four different slit widths, $W_P{}^* = 3, 4, 6$ and 8. At a first glance, a line of molecules are seen near the upper and the lower surfaces through the x-direction and also many molecules are gathering in the middle region at the left-hand side of the pore. The left-hand side is the high-pressure (H-) region where the pore density of ethane is kept to be in equilibrium with the feed gas at P_H by use of the μVT ensemble technique; that is, the possibility of molecules appearing or disappearing in the H-region is mainly determined by the Boltzmann factor involving the potential energy that each molecule feels. Molecules having appeared in the center are attracted from the two wall surfaces; therefore, they move toward either of the two surfaces to join a line of molecules in monolayers during a travel from the left-hand side (H-region) to the right-hand side (L-region). When the pore is as narrow as $W_P{}^*=3$, many molecules appear in the center of the pore, crossing between two monolayer regions. This is because the potential difference for an ethane molecule to feel in the center and in the monolayer becomes small when the slit width becomes narrow.

Figure 2-3 shows the density profile and the number flux averaged in each subcell for pores of different slit widths. The ordinates, ρ_p^* and J^*, are shown in logarithmic scale. The density of the L-region, which is kept at zero during the simulation, is, therefore, not shown in the figure. The density curves decrease from the H-region to the L-region as shown in Fig. 2-3a; they change almost linearly in the M- region. The number fluxes calculated in the M-region are almost constant as shown in Fig. 2-3b, which indicates that dynamically stationary states have been achieved in each simulation run. Both the curves of ρ_p^* and J^* decrease with increasing slit width. This is because the pore density in the H-region decreases with increasing slit width due to weakening in the attractive potential exerted from the opposite surface.

It is noteworthy that the fluxes of ethane (J_2^*) shown in Fig. 2-3b are approximately 10^4 times larger than the values estimated from the experimental permeability of ethane through a carbon membrane [Rao adn Sircar, 1993] by taking into account the void fraction and the tortuosity factor of pores of the carbon membrane. The large difference between the simulated and the experimental fluxes may indicate that the pore structure of the carbon membrane that Rao and Sircar provided is characterized to have the activation energy for mass transport in the direction of permeation.

Figure 2-4 shows an interesting feature of the velocity distribution calculated in subcells No. 2 and No. 15 for the slit pore of $W_p^* = 6$ and $L = 25.03$ nm. The histogram of open bars in subcell No. 2 is slightly asymmetric while that of the filled bars in subcell No. 15 is highly asymmetric, indicating that most molecules have positive velocities (a downward flow). The histograms in Fig. 2-4 are acceptable for understanding the simulation results showing high density in upstream and low density in downstream with constant molar flux. It is also noted that collisions in the x-direction occur even in subcell No. 15 since

there are 17 % molecules moving upward (negative velocities).

2.3.2 Permeation of mixed gas

For simulations of mixed-gas permeation, a binary mixture of methane (1) + ethane (2) and a slit-shaped pore of $W_p{}^* = 6$ and $L = 25.03$ nm are chosen. The pore densities of each component in equilibrium with the feed mixed-gas ($y_1 = 0.5$, $P_H = 0.5$ MPa) have been calculated at temperatures, 298.2, 400, 500 and 600 K, by using the μVT ensemble MC method. **Figure 2-5** shows the pore densities of methane and ethane for an equimolar mixture (solid lines) and those for pure gases (broken lines) against the reciprocal temperature. For pure gases, the density of ethane ($\square$) is always larger than that of methane ($\blacksquare$), and they increase with decreasing temperature. At high temperatures, the densities of ethane ($\bigcirc$) and methane ($\bullet$) for an equimolar mixture are nearly half the densities of pure ethane ($\square$) and pure methane ($\blacksquare$), respectively, which straightly reflects the fact that the partial pressures of an equimolar mixture are half the total pressure. On the other hand, at low temperatures like 298.2 K, the density of ethane of a mixture ($\bigcirc$) becomes much higher than half the density of pure ethane while the methane density ($\bullet$) decreases much less than half the density of pure methane [Nozawa and Nitta, 1993]. The suppression of methane adsorption is a typical characteristic of competitive adsorption of stronger adsorbate, ethane in the present case, preferentially covering the monolayer of the surface. On the other hand, the reason why the higher density of ethane is observed in the mixed-gas adsorption is on the fact that the adsorption isotherm of pure ethane is convex upward on the plots of the pore density against the pressure; that is, the pore density of ethane decreases much less than the expectation calculated from the Henry law when the partial pressure decreases.

The μVT-NEMD simulations were performed for an equimolar feed gas permeation through $P_H = 0.5$ MPa and $P_L = 0$. **Figure 2-6** shows a snapshot of molecular configurations of methane (●) and ethane (○) in the simulation cell at $T = 298.2$ K. The lower picture indicates that the surface flow occurs in the permeation of mixed-gas as well as in the pure ethane as shown in Fig. 2-2. In the lower picture, three methane molecules located outside the monolayer are distinguishable; however, in the upper picture, methane molecules exist almost randomly in monolayers, as do ethane molecules.

Figures 2-7a and 2-7b show the logarithm of the density profiles and the number fluxes of methane (filled keys) and ethane (open keys) for the mixed-gas permeation at different temperatures through the slit-shaped pore of $W_p^* = 6$ and $L = 25.03$ nm. The density profiles against the diffusion distance resemble those of pure ethane; that is the densities decrease from H-region to L-region and in the middle region they decrease almost linearly in the semilogarithmic scale. The number fluxes are nearly constant for each run and they decrease with increasing temperature due to the decrease in pore densities.

The permeabilities of methane and ethane are calculated from

$$\hat{P}_k = \frac{\bar{J}_k \cdot L}{\Delta P \cdot y_k} \tag{2-12}$$

They are shown in **Fig. 2-8** against the reciprocal temperature, together with the permeability of pure gases (broken lines). The curves of $\hat{P}$ decrease with increasing temperature; for example, $\hat{P}$ (600K) / $\hat{P}$ (298K) = 0.27 for ethane, which is much smaller than the expectation, 0.70, calculated from the Knudsen diffusion mechanism. It is interesting to see that $\hat{P}_{ethane}$ for the mixture (○) is slightly

larger than that for pure ethane ($\square$) over the whole range of temperature, while $\hat{P}_{\text{methane}}$ for the mixture ($\bullet$) is considerably smaller than that for pure methane ($\blacksquare$). The values of $\hat{P}$ calculated in the present model are affected by two factors: the pore densities at the feed-side of membrane and the diffusivity (or the kinematic viscosity in the case of surface flow). Generally speaking, the magnitude of $\hat{P}$ increases when the relative magnitude of pore density or diffusivity of each component increases. At low temperatures, it is observed that a significant decrease in $\hat{P}$ for methane and an increase in $\hat{P}$ for ethane, both of which are attributable to the changes of pore density; that is, the density of methane decreases due to the competitive adsorption and that of ethane increases due to the convex nature of the adsorption isotherm as discussed previously. At higher temperatures, however, the reason why $\hat{P}$ for methane decreases and that for ethane slightly increases may be the changes of the diffusivities of each component; that is, the total density of the mixed-gas becomes lower than that of pure ethane, which results in the increase in the diffusivity. On the other hand, it is higher than that of pure methane, which results in the decrease in the diffusivity.

The separation factor α_{21} for permeation is calculated from the number fluxes and the feed compositions as

$$\alpha_{21} = \frac{\bar{J}_2 / \bar{J}_1}{y_2 / y_1} \tag{2-13}$$

The equilibrium separation factor $\alpha_{21}^{(\text{eq})}$ was also calculated as

$$\alpha_{21}^{(\text{eq})} = \frac{\rho_{2,\text{p}} / \rho_{1,\text{p}}}{y_2 / y_1} \tag{2-14}$$

They are shown in **Fig. 2-9** together with the ratio of the permeability of pure ethane to that of pure methane. It is noted that all the separation factors decrease with increasing temperature and that the curves of α_{21} and $\alpha_{21}^{(eq)}$ are almost identical, which shows that the separation through the present permeation mechanism is controlled by the adsorption equilibrium densities attained in the H-region. The difference between α_{21} and $\hat{P}_2/\hat{P}_1$ is also remarkable. The permeability ratio remains almost constant over the wide range of temperature while the curve for α_{21} significantly increases with decreasing temperature where adsorption of ethane becomes large so as to cover the monolayer of the surface.

2.4 Summary

The μVT-NEMD method, a combination of the μVT-MC and the boundary-driven NEMD, has been applied to simulating permeation of pure- and mixed-gas through membranes with slit-shaped pores under the assumption of the local adsorption equilibrium at the ends of the membrane. Methane and ethane are selected for permeating gases. This method gives constant mass fluxes for each component in subcells, which indicates that a dynamically stationary state has been achieved for a system with two boundaries, one side is in equilibrium with a feed gas and another is zero in density. To reach the stationary state, however, it usually takes longer time than conventional equilibrium MD; approximately 50,000 - 60,000 time steps computations and 500 - 2,000 molecules in a cell are required for obtaining better statistics in the NEMD.

The simulation results obtained from the assumption of the local adsorption equilibrium indicate that the gas permeation mechanism through membranes with slit-shaped pores may be called the selective adsorption followed

by surface diffusion (or flow in the case of flat surface walls) as properly stated by Rao and Sircar [1993]. Dynamical behavior of molecules in simulation boxes was well observed by using computer graphics animations.

Under a constant feed pressure condition, the mass flux for pure- and mixed-gas permeation decreases significantly with increasing temperature because of the decrease in the pore density which is in equilibrium with a feed gas. In the case of binary mixture permeation, the competitive adsorption plays an important role in enhanced selectivity of more adsorptive substance, ethane in case of a mixture of methane and ethane. The role of the competitive adsorption becomes more significant as the temperature decreases.

The fluxes calculated with the present pore model are found to be extraordinarily large, compared to the experimental values estimated from the permeabilities of a carbon membrane provided by Rao and Sircar [1993]. The flat surface presumed in the present work may be the major reason for the large fluxes. Further studies by the μVT-NEMD simulation method will be useful to separately explore many factors influencing the permeability and the permselectivity, such as mass transport resistances at two ends, surface heterogeneity, pore geometry, molecular size, and interaction potential as well as temperature, pressure, and fluid composition.

Nomenclature

j_k = mass flux for component k, [kg m^{-2} s^{-1}]

J_k = number flux for component k [mol m^{-2} s^{-1}]

L = membrane thickness ($= L_x/2$) [m]

L_x, L_y, L_z = lengths of a simulation box in x-, y-, and z-directions [m]

m = mass of a molecule [kg]

N = number of molecules [-]

P = pressure [Pa]

P_{create} = transitional probability for insertion operation [-]

P_{destr} = transitional probability for destruction operation [-]

$\hat{P}$ = permeability [mol m m^{-2} s^{-1} Pa^{-1}]

r = distance [m]

T = temperature [K]

V = volume [m^3]

v = velocity [m s^{-1}]

$\bar{v}$ = average velocity [m s^{-1}]

v_0 = barycentric velocity [m s^{-1}]

W_p = pore width [m]

y = mole fraction of feed gas [-]

z = perpendicular distance between a molecule and a surface [m]

$z_{i,H}$ = absolute activity of component i in the H-region [-]

α_{21} = selectivity defined by fluxes [-]

$\alpha_{21}^{(eq)}$ = selectivity defined by equilibrium densities [-]

β = $1/kT$ [J^{-1}]

ε = LJ energy parameter [J]

$\varPhi$	= potential energy	[J]
ϕ	= potential energy	[J]
Λ	= thermal de Broglie wavelength	[m]
μ	= chemical potential	[J]
ρ	= number density	[m^{-3}]
σ	= LJ size parameter	[m]

<Subscripts>

1	= methane
2	= ethane
ij	= pair of molecules i and j
k	= component k
H	= high pressure region
L	= low pressure region
p	= pore phase
s	= solid surface

<Superscripts>

| * | = dimensionless quantity |
| (L) | = L-th subcell |

Reference

Allen, M.P. and D.J. Tildesley; Computer Simulation of Liquids, Clarendon Press, Oxford, England (1987)

Chen, Y.D. and R.T. Yang; "Preparation of Carbon Molecular Sieve Membrane and Diffusion of Binary Mixtures in the Membrane," *Ind. Eng. Chem. Res.*, **33**, 3146-3153 (1994)

Evans, D.J. and G.P. Morriss; Statistical Mechanics of Nonequilibrium Liquids, Academic Press, England (1990)

Hafskjold, B., T. Ikeshoji, and S.K. Ratkje; "On the Molecular Mechanism of Thermal Diffusion in Liquids," *Molec. Phys.*, **80**, 1389-1412 (1993)

Ikeshoji, T. and B. Hafskjold; "Non-equilibrium Molecular Dynamics Calculation of Heat Conduction in Liquid and through Liquid-Gas Interface," *Molec. Phys.*, **81**, 251-261 (1994)

Kimura, S.; "Glowing Future of Inorganic Membranes," *The J. the Surface Finishing Society of Japan*, **45**, 1080-1083 (1994)

Nitta, T., M. Nozawa and Y. Hishikawa; "Monte Carlo Simulation of Adsorption of Gases in Carbonaceous Slitlike Pores," *J. Chem. Eng. Japan*, **26**, 266-272 (1993)

Nitta, T. and J. Yoneya; "Computer Simulations for Adsorption of Benzene Diluted in Supercritical Carbon Dioxide," *J. Chem. Eng. Japan*, **28**, 31-37 (1995)

Nozawa, M. and T. Nitta; "Computer simulation of Adsorption of Binary LJ Fluids in a Slitlike Pore," *Chem. Eng. Symp. Ser., Japan*, **35**, 119-124 (1993)

Rao, M.B. and S. Sircar; "Nanoporous Carbon Membranes for Separation of Gas Mixtures by Selective Surface Flow," *J. Mem. Sci.*, **85**, 253-264 (1993)

Steele, W.A.; The Interaction of Gases with Solid Surfaces, Pergamon Press,

Oxford, England (1974)

Suda, H. and K. Haraya; "Molecular Sieving Effect of Carbonized Kapton Polyimide Membrane," *J. Chem. Soc., Chem. Commun.*, 1179-1180 (1995)

Uhlhorn, R.J.R. and A.J. Burggraaf; "Gas Separations with Inorganic Membranes," in Inorganic Membranes: Synthesis, Characterization, and Application by Bhave, R.R (ed.); Van Nostrand Reinhold, New York, USA (1991)
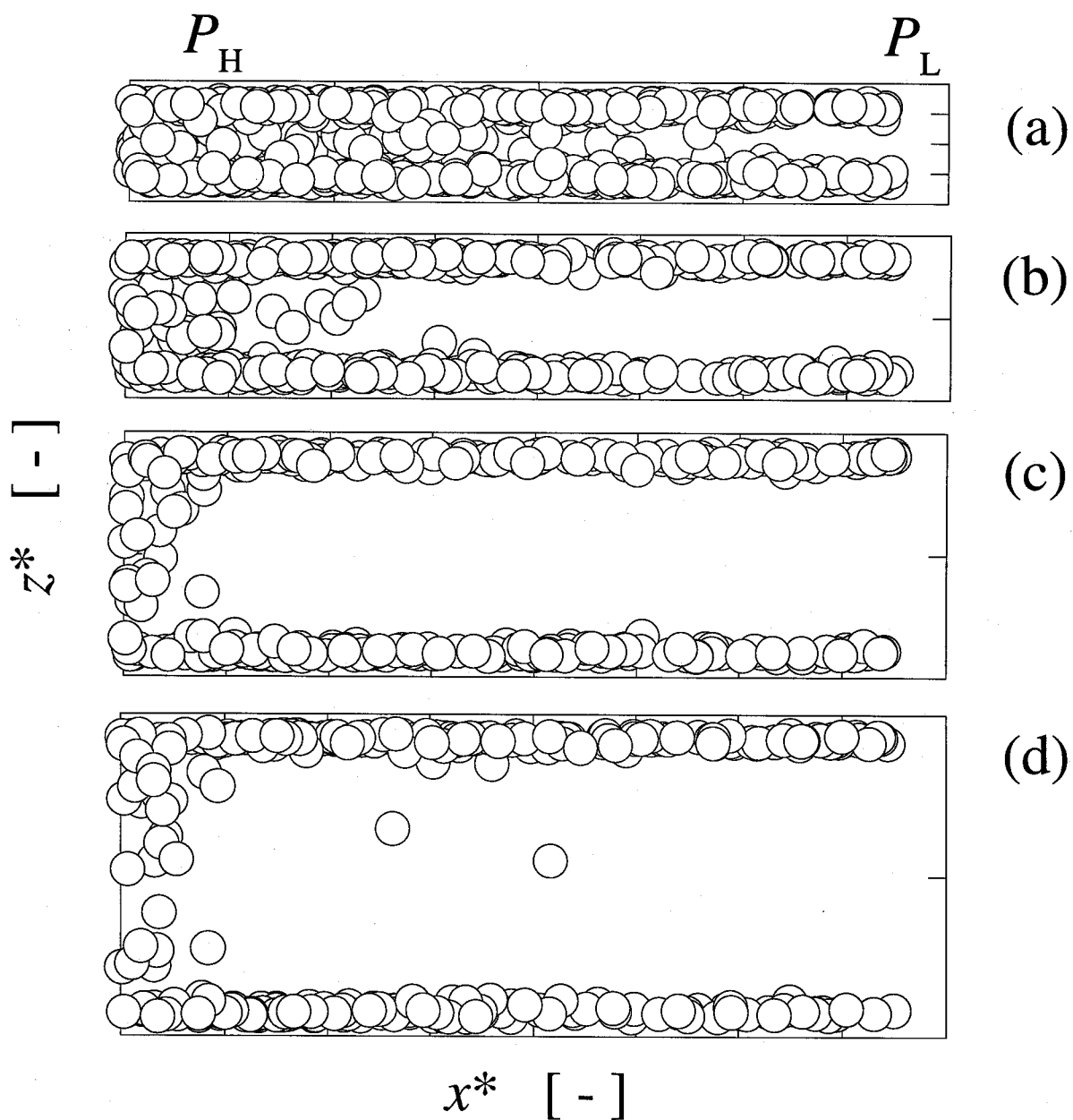
Figure 2-1   Schematic diagram of simulation cell

Figure 2-2 Snapshots in half simulation cell for C_2H_6 at $T = 298.2$ K and $\Delta P =$
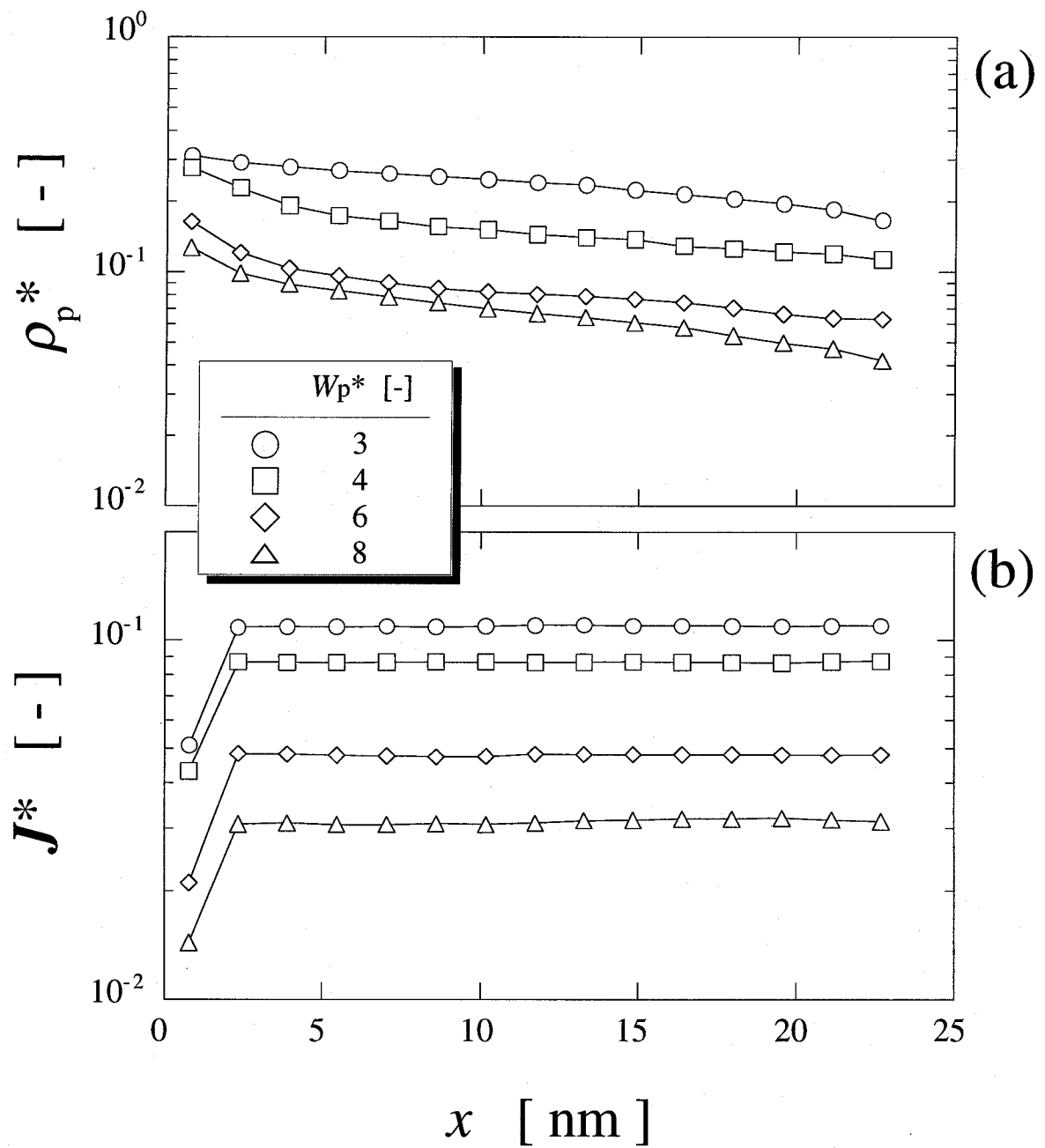0.5 MPa for different values of W_p^*: (a) 3, (b) 4, (c) 6, (d) 8

Figure 2-3 Effect of slit width W_p^* on density and number flux profiles of C_2H_6 for $L = 25.03$ nm at $T = 298.2$ K and $\Delta P = 0.5$ MPa
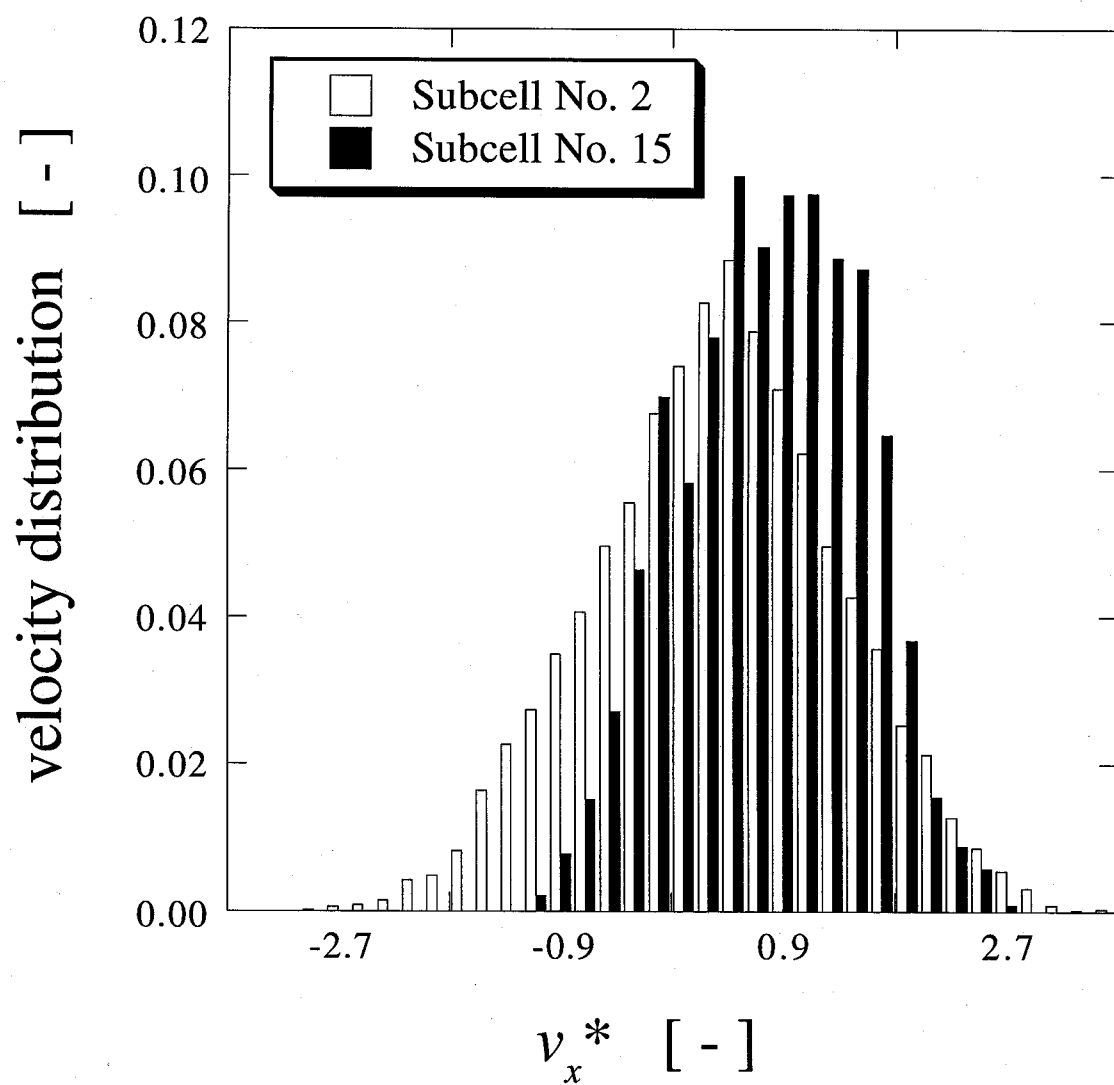
Figure 2-4   Distribution of velocity of C_2H_6: $W_p^* = 6$, $L = 25.03$ nm at $T = 298.2$ K and $\Delta P = 0.5$ MPa
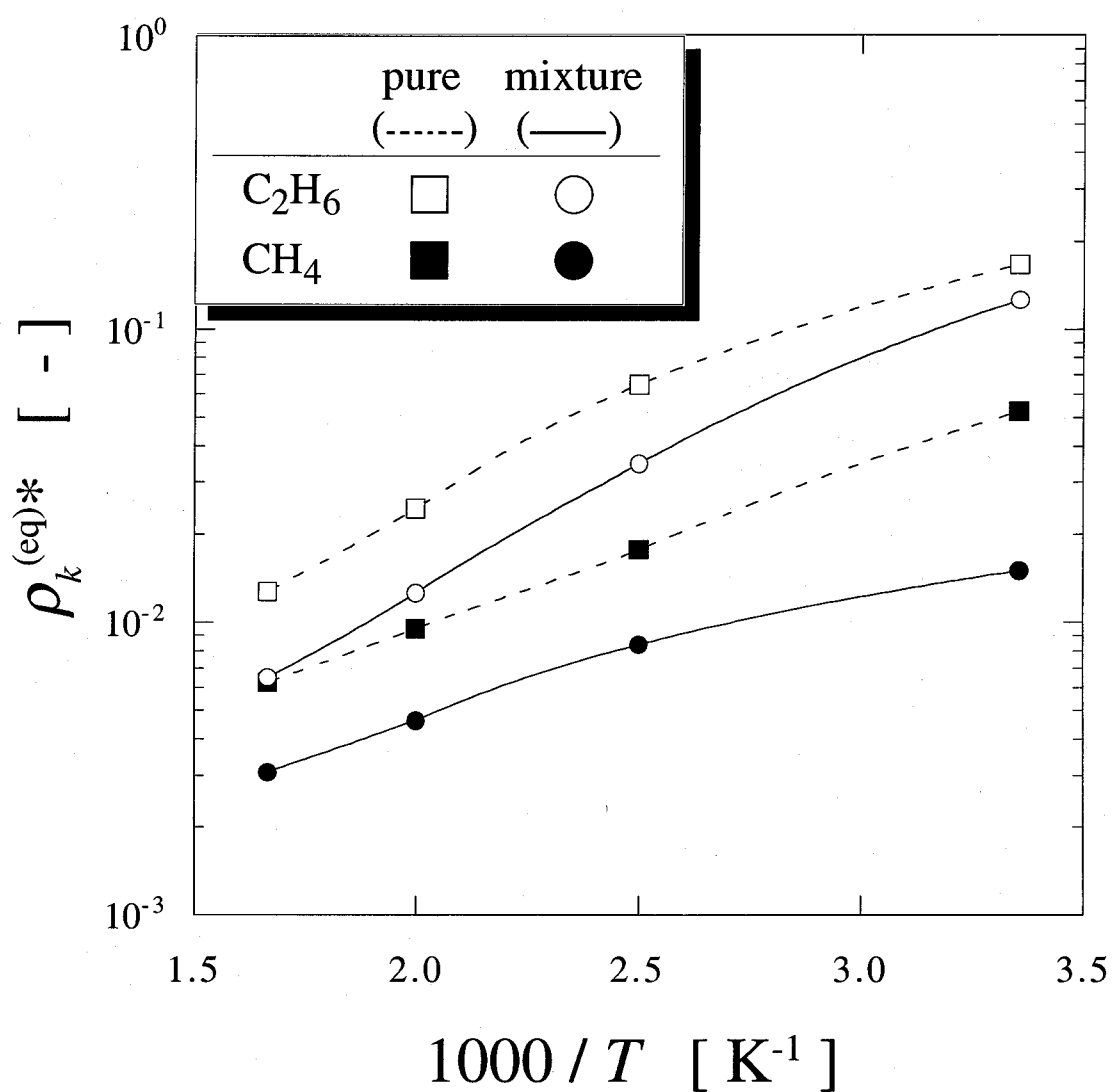
Figure 2-5 Temperature dependence of pore density in equilibrium with bulk gas of CH_4 and C_2H_6 for pure and equimolar mixed gases at $\Delta P = 0.5$ MPa for a slit pore of $W_p^* = 6$
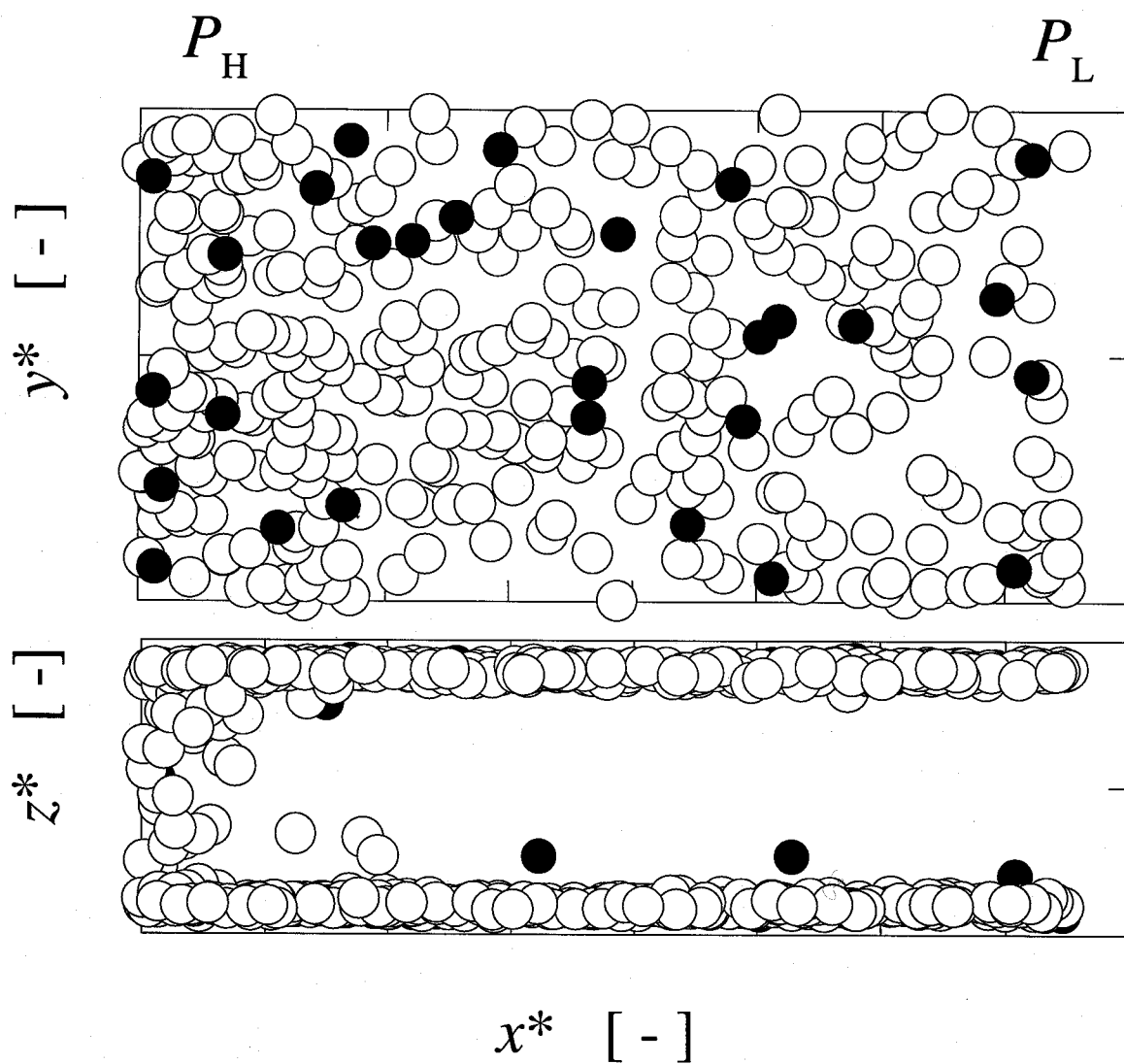
Figure 2-6 Snapshot of CH_4 and C_2H_6 in a simulation cell of $W_p^* = 6$ and $L = $ 25.03 nm for a mixture of $y_1 = 0.5$: $T = 298.2$ K, $\Delta P = 0.5$MPa
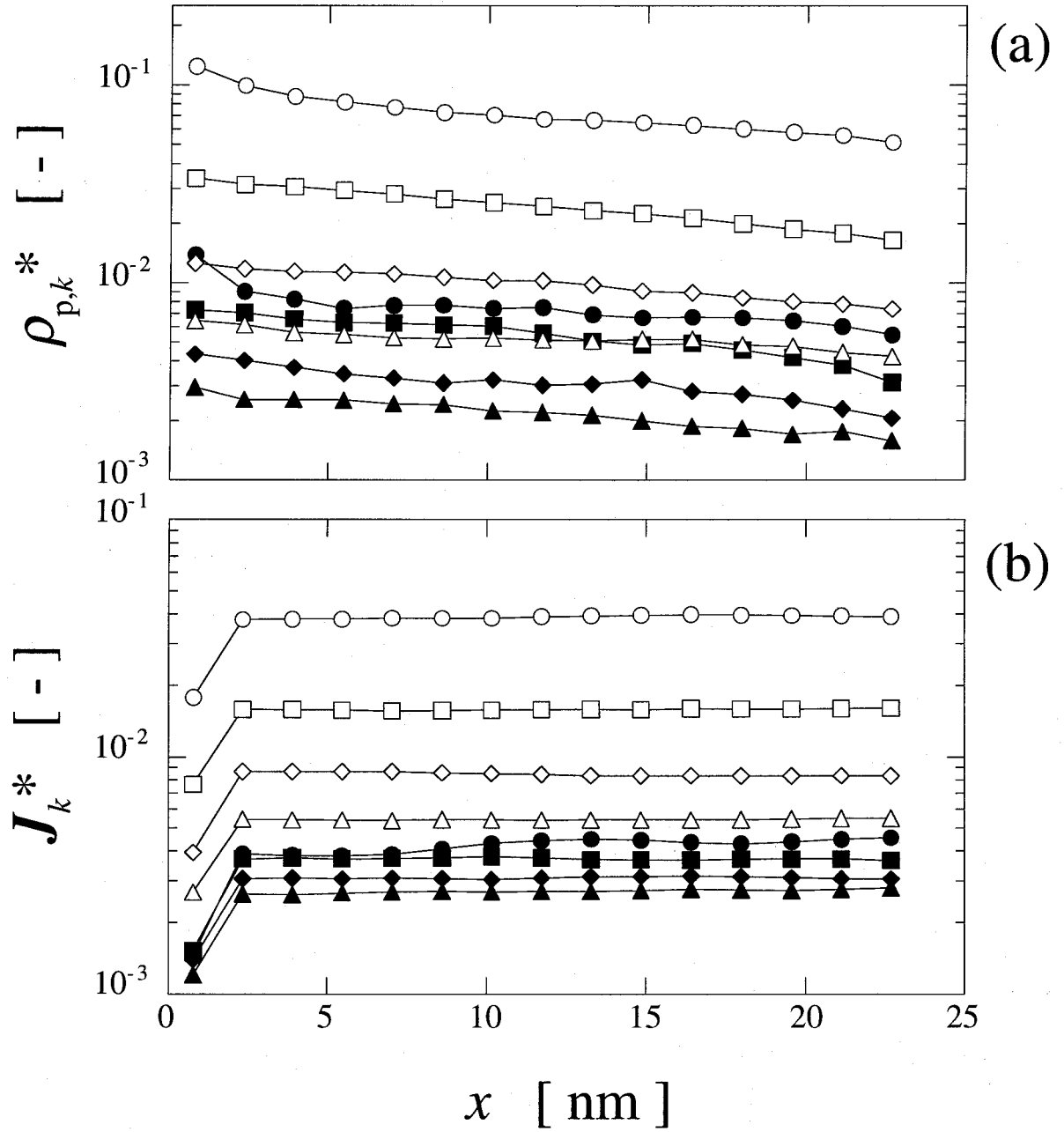
Figure 2-7   Density and number flux profiles of CH_4 and C_2H_6 mixture (y_1 = 0.5) for L = 25.03 nm and W_p^* = 6 at ΔP = 0.5 MPa and different temperatures: T = 298.2(●, ○), 400(■, □), 500(◆, ◇), 600K(▲, △)
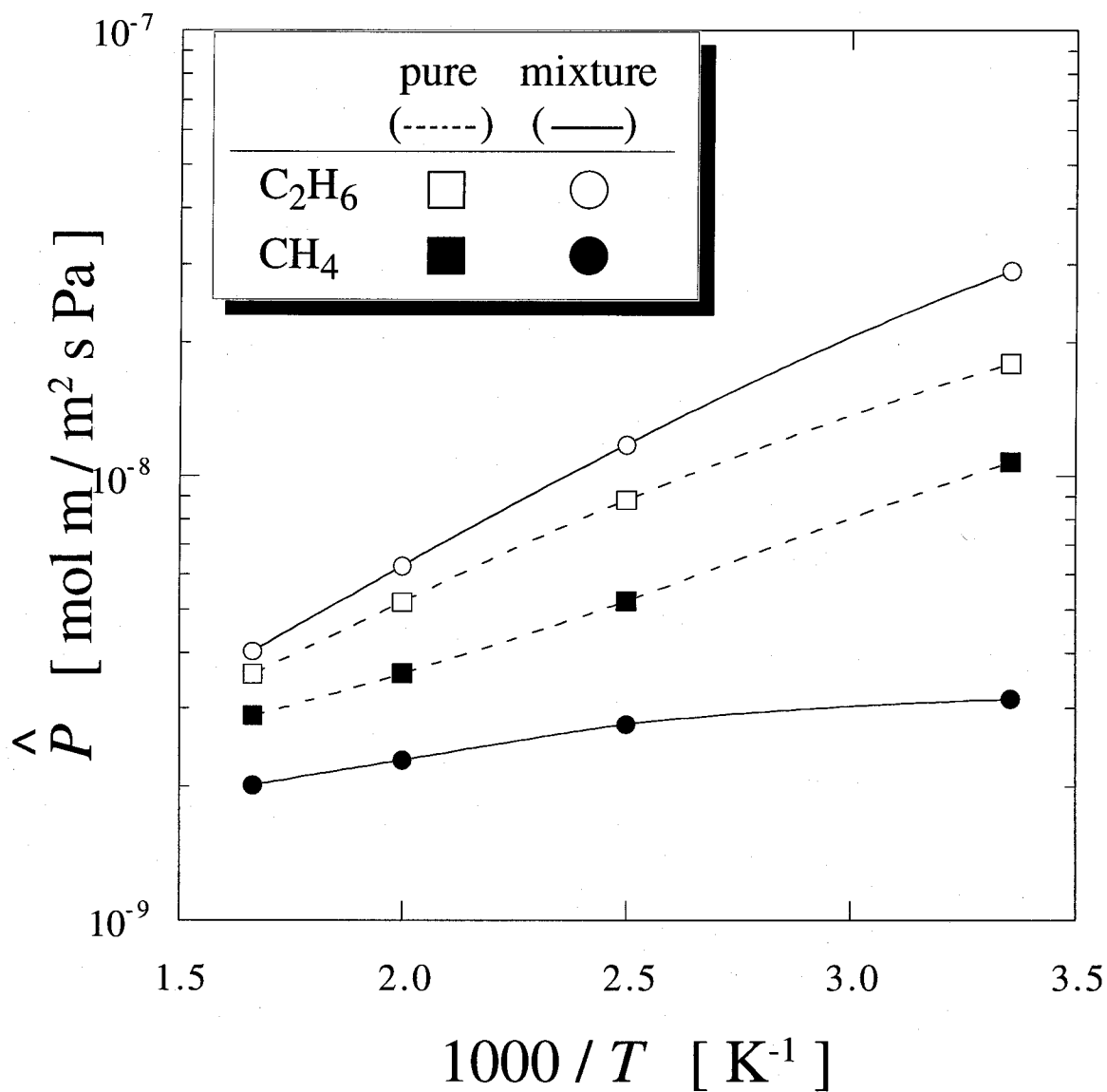
Figure 2-8 Temperature dependance of permeability of CH_4 and C_2H_6 for pure and equimolar mixed gases at $\Delta P = 0.5$ MPa for a slit pore of W_p^* = 6

Figure 2-9 Effect of temperature on separation factors and permeability ratio for $L = 25.03$ nm and $W_p{}^* = 6$ at $\Delta P = 0.5$ MPa

Chapter 3
Effects of Surface Heterogeneity on Gas Permeation through Carbon Membranes with Random Heterogeneous Surfaces

3.1 Introduction

In the previous chapter, the simulation results are reported on permeation of gases in slit-shaped pores of nearly flat surfaces composed of graphite basa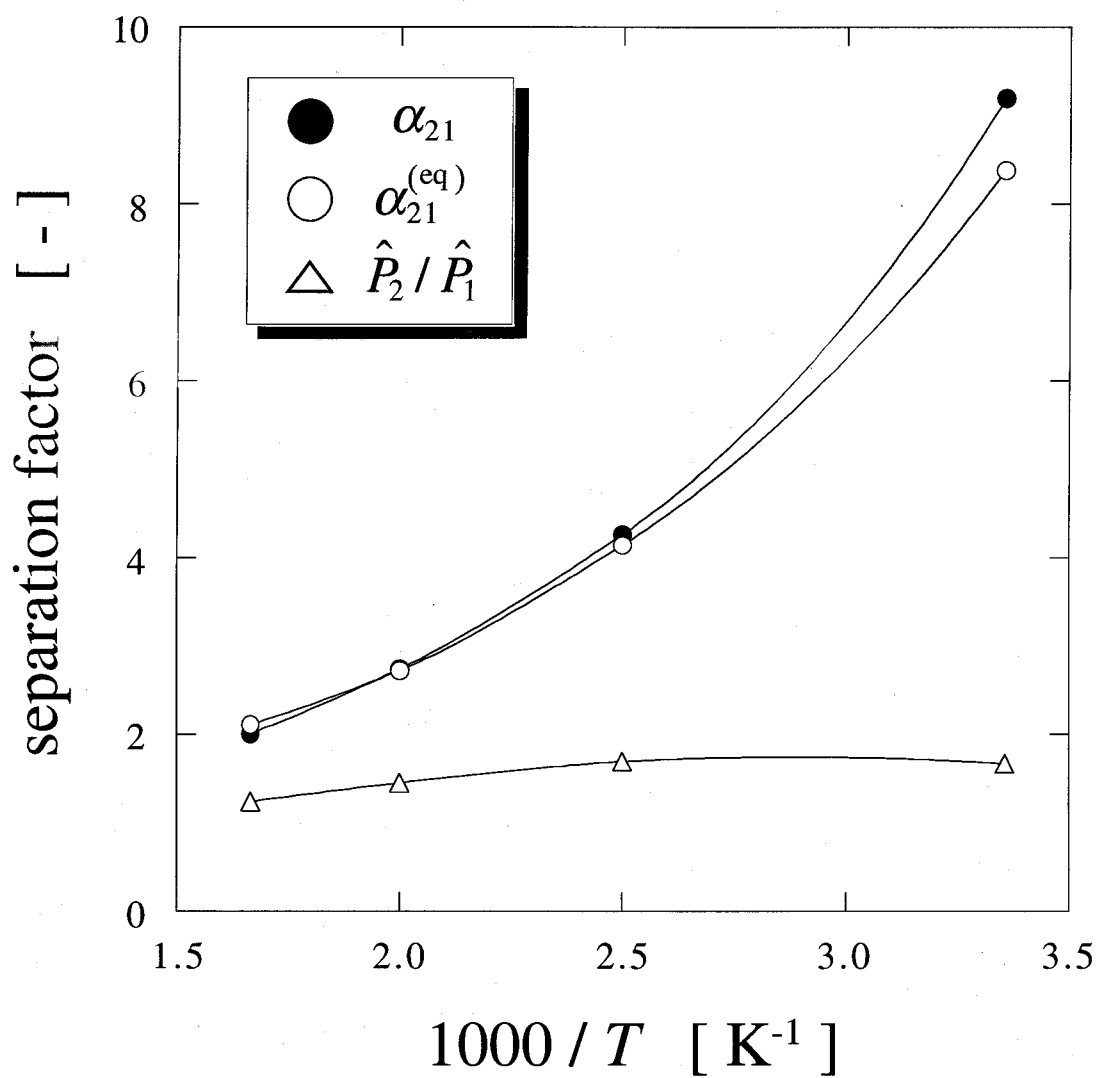l planes. The calculated permeation fluxes of ethane were found to be approximately 10^4 times larger than the values estimated from the experimental data of permeability through a carbon membrane reported by Rao and Sircar [1993]. There would be many factors to decrease the permeation rate of gases in micropores: surface heterogeneity, connectivity of channels, and energy barriers at the feed and permeation sides of membranes. According to a recent review of Steele [1997], computer simulation studies of surface diffusion on heterogeneous surfaces are just beginning; for example, there have been reported simulations of diffusion on nearly flat surfaces, surfaces with steps or grooves. Recently, Riccardo and Steele [1996] reported molecular dynamic simulations of diffusion of argon adsorbed on amorphous surfaces of titanium dioxide, which was roughened by deleting varying numbers of oxides at random from the outer layer of the solid. The amorphous surfaces will be denoted as random heterogeneous surfaces compared to another extreme class of heterogeneous surfaces, patchwise surfaces.

The present chapter describes the extension of the previous simulation studies on gas permeations through carbonaceous membranes to investigate the effect of surface heterogeneity on permeation fluxes. The slit-shaped pores are modeled to have random heterogeneous surfaces composed of graphite planes;

permeating gases are methane and ethane.

3.2 Simulation Mmethod

3.2.1 The μVT-NEMD

The μVT-NEMD method described in chapter 2 was employed for simulating permeation of gases through a membrane. Since details are given in the previous chapter, a brief description of the method will be given. **Figure 3-1** shows a schematic diagram of a simulation cell. There are two controlling regions: H-regions and L-regions. Throughout a simulation run, the density (ρ_H) and the composition (x_1) in the H-region are kept constant at specified values that are in equilibrium with a feed gas at a given pressure (P_H) and a composition (y_1) while the densities of the L-region are kept at zero (i.e. $P_L = 0$). The insertion and destruction algorithms of the μVT-MC method are implemented for maintaining the densities in the H-regions. Molecules move from the H-region to the L-region through a conventional molecular dynamics (leap-frog) algorithm. The molecules which enter into the L-region are removed immediately. In the x- and y- directions, the periodic boundaries and the minimum image convention [Allen and Tildesley, 1987] are used for molecular movements and intermolecular force calculations. The molecular velocities are rescaled independently in three directions at each time step so as to keep the temperature of molecules in each subcell to be at a specified value (T).

The time step was set at 0.01 ps. The 60,000 steps were discarded, and the next 40,000 steps were collected for ensemble averaging. In a simulation run, the length of the simulation cell in the y-direction (L_y) was adjusted so as to contain about 500 to 2,000 molecules in the elementary cell.

3.2.2 Random heterogeneous surfaces

The upper and lower surfaces in Fig. 3-1 are the slit-shaped pore surfaces composed of graphite basal planes. The circles shown in Fig. 3-1 represent carbons in the first basal planes; heterogeneous surfaces are made by randomly removing a certain number of carbons of the first planes. The site fraction of the removed carbons is denoted as f_b, which is a measure of the surface heterogeneity.

$$f_b = \frac{\text{number of carbons removed}}{\text{number of carbons on a graphite plane}} \qquad (3\text{-}1)$$

The value of f_b is varied from 0.0 to 0.2. Intermolecular interactions between molecules and those between molecule and carbon atoms on the first plane of the wall are represented by the 12-6 LJ potential function as

$$\phi_{ij}(r) = 4\varepsilon_{ij}\left[\left(\frac{\sigma_{ij}}{r}\right)^{12} - \left(\frac{\sigma_{ij}}{r}\right)^{6}\right] \qquad (3\text{-}2)$$

where r is the distance between molecules i and j (or molecule i and atom j), and ε_{ij} and σ_{ij} are potential parameters for a pair of i and j. Removal of carbon atoms was done only for the first basal planes; the second and more inside graphite planes were presumed to remain. Therefore, their interactions with molecule i are represented by the 10-4-3 potential [Steele, 1974].

$$\phi_{is}(z) = 4\pi A_{is}\left[\frac{2}{5}\left(\frac{\sigma_{is}}{z}\right)^{10} - \left(\frac{\sigma_{is}}{z}\right)^{4}\right] - \frac{\sigma_{is}^{4}}{3\Delta(z+0.61\Delta)^{3}} \qquad (3\text{-}3)$$

where A_{is} ($= \varepsilon_{is}\sigma_{is}^{2}/a_s$) is a constant, a_s the surface area of a graphite basal unit, Δ the spacing between adjacent graphite basal planes, and z is the distance between molecule i and the second graphite plane. Methane and ethane are chosen as permeating gases. The LJ parameters for the two gases and the carbon are summarized in **Table 3-1**, which are the same as those used in the previous chapter.

Figure 3-2 shows examples of the lowest potential surface for a ethane molecule to feel on two surfaces characterized by the site fraction $f_b = 0.0$ and 0.192. In the case where $f_b = 0.0$, the lowest potential energy surface is nearly flat, while in the case where $f_b = 0.192$, it shows many peaks and hollows. Therefore, molecules permeating through the membrane must feel the rough wall structure. It is noted here that 388 carbons were used for the flat graphite plane from which carbons were removed to get rough walls. The wall thus obtained at a specified value of f_b was used periodically in the simulation of permeation on the rough surface.

3.3 Results and Discussion

3.3.1 Effect of site fraction

Molecular simulations of pure- and mixed-gas permeations were performed for exploring the effect of surface heterogeneity on permeation and selectivity. Pure gases are methane and ethane, and a binary gas is a mixture of methane (1) + ethane (2) whose composition is set at $y_1 = 0.8$ (a methane-rich gas mixture). All simulations in subsection 3.3.1 were performed by varying the site fraction f_b under the following conditions: $T = 298$ K, $P_H = 0.5$ MPa, $W_p = 2.347$ nm, and $L_{mem} = 25.58$ nm.

Figure 3-3 shows examples of typical trajectories of an ethane molecule projected on the *xy*-plane observed in a simulation of pure ethane permeation. When the surface heterogeneity increases, a molecule changes its direction due to collisions with the heterogeneous sites randomly distributed on the surface, which may result in slow permeation rate. **Figures 3-4a** to **3-4e** show snapshots of molecular configurations for permeations of the binary mixture in four pores with different site fractions. Figures 3-4a and 3-4b are a top view and a side view, respectively, for f_b = 0.0 while Figures 3-4c to 3-4e are side views for f_b = 0.041, 0.094 and 0.185, respectively. The left-hand side hatch denotes the feed-gas side of the pore (H-region) and the right-hand side hatch denotes the low-pressure side (L-region) where the density is kept at zero. Figure 3-4 clearly indicates that molecular movements are characterized by "surface flow". In addition, it was observed that molecules occasionally appear in the center region of a pore due to collisions with heterogeneous sites when the surface heterogeneity increases.

Figure 3-5 shows profiles of (a) densities and (b) molar fluxes of the binary mixture permeating in slitpores of different f_b against the permeating direction. The densities decrease from the H-region to the L-region almost linearly. On the other hand, the molar fluxes are almost constant, which indicates that dynamically stationary states have been achieved in each simulation run. In Fig. 3-5a, the data points at the left-hand side of each curve represent the pore density, ρ_H, which is in equilibrium with the feed gas at P_H. Although the mixed-feed gas is methane-rich (y_1=0.8), the pore density in the feed side is ethane-rich. The suppression of methane adsorption is a typical characteristic of competitive adsorption of stronger adsorbate, ethane in the present case, which preferentially covers the monolayer of the surface. The decrease in total pore density ρ_H with increasing f_b is ascribed to the decrease in the average potential

energy that each molecule feels from the surface walls, due to the lack of carbons on the first planes of graphite walls.

Both curves of densities (Fig. 3-5a) and molar fluxes (Fig. 3-5b) decrease with increasing f_b. However, it is noted that the decrease in molar fluxes is much greater than that in densities: for an example, the molar flux for $f_b = 0.185$ is about one fifth value for $f_b = 0.0$. The mass-transfer coefficient was calculated in order to understand the effect of surface heterogeneity on the permeation rate in terms of the permeation resistance.

$$\bar{J}_k = k_k \left(\rho_{H,k} - \rho_{L,k} \right) \tag{3-4}$$

or

$$k_k = \bar{J}_k / \rho_{H,k} \quad \left(\because \rho_{L,k} = 0 \right) \tag{3-5}$$

where $\bar{J}$ is the average of molar flux, k is the mass-transfer coefficient, and subscript k denotes component k. **Figure 3-6** shows the curves of k and ρ_H for pure gases against the site fraction. It is noteworthy that the mass-transfer coefficients of pure methane and pure ethane decrease significantly with a small increase in f_b while ρ_H decreases almost linearly. A remarkable effect of surface heterogeneity introduced in the present model surface is the decrease in the mass-transfer coefficient or the increase in permeation resistance, which is attributable to collisions of each molecule onto heterogeneous sites. The pure gas mass-transfer coefficients of methane are always larger than those of the ethane which might be ascribed to the larger diffusivity (or mobility) of methane than that of ethane.

Figure 3-7 shows the curves of k and ρ_H for the mixed-gas against the site fraction. The mass-transfer coefficients of two gases also decrease significantly with a small increase in f_b. However, it is interesting to see the fact that each curve for the mass-transfer coefficient is almost identical and the same as that for pure ethane shown in Fig. 3-6. The suppression in diffusivity of methane molecules may be due to collisions with ethane molecules having a larger mass and slower velocities.

It is also noteworthy that the curve for ρ_H of methane decreases much less than the expectation from the decrease in the partial pressure of methane (i.e. $y_1 = 0.8$): the values of ρ_H for methane in mol/L are 2.79 for pure and 0.96 for the mixed-gas in the case of $f_b = 0.0$. This is due to the competitive adsorption of ethane as mentioned previously. The values of ρ_H for ethane in mol/L are 5.26 for pure and 2.45 for the mixed-gas ($y_2 = 0.2$ and $f_b = 0.0$). The rather small decrease in ρ_H for ethane in the mixed gas is due to the shape of adsorption isotherm (adsorption against pressure) of ethane, the curve of which is concave upward rather than linear at the pressure of interest.

The separation factor α_{21} for permeation is calculated from the number fluxes and the feed compositions as

$$\alpha_{21} = \frac{\bar{J}_2/\bar{J}_1}{y_2/y_1} \qquad (3\text{-}6)$$

The equilibrium separation factor ($\alpha_{21}^{(eq)}$) and the ratio of permeability of pure ethane to that of pure methane ($\hat{P}_2/\hat{P}_1$) were calculated. The $\alpha_{21}^{(eq)}$ is defined by the pore densities and compositions at the feed side as

$$\alpha_{21}^{(eq)} = \frac{\rho_{H,2}/\rho_{H,1}}{y_2/y_1} \qquad (3\text{-}7)$$

and $\hat{P}_k$ for component k is defined as

$$\hat{P}_k = \bar{J}_k L_{\text{mem}} / (P_H - P_L)$$ (3-8)

Figure 3-8 shows the separation factors against site fraction f_b. The separation factors decrease with increasing f_b and that the curves of α_{21} and $\alpha_{21}^{(eq)}$ are almost identical. Therefore, if the feed side of the membrane is locally in equilibrium with the feed gas, the selectivity is almost controlled by the adsorption equilibrium densities at the feed side. It is noted that the difference between α_{21} and $\hat{P}_2/\hat{P}_1$ is remarkable. The major cause of this difference is the competitive adsorption of ethane to methane.

3.3.2 Effects of temperature and pressure

Figure 3-9 shows the effect of temperature on mass-transfer coefficients and densities of pure ethane permeation through pores of two site fractions: $f_b = 0.0$ and 0.2. Each curve for the mass-transfer coefficients increases with increasing temperature while each curve for ρ_H decreases. It is noted that the mass-transfer coefficient at $T = 600$ K is two times larger than that at $T = 298$ K while ρ_H at $T = 600$ K is one tenth of ρ_H at $T = 298$ K. Therefore, the permeation rate significantly decreases with increasing temperature if the permeation is controlled by the local adsorption equilibrium at the feed side (adsorption controlling permeation).

Figure 3-10 shows the effect of pressure at the feed side, P_H, on the mass-transfer coefficient and the pore density, ρ_H, of pure ethane permeation through pores of two site fractions: $f_b = 0.0$ and 0.2. The curves of ρ_H for the two

pores increase with an increase in P_H, being convex upward, while the mass-transfer coefficients are almost constant. Therefore, the permeation flux will increase proportionally with increasing ρ_H, but it will increase nonlinearly with an increase in P_H when the permeating gas such as ethane is strongly adsorbed.

3.4 Summary

The μVT-NEMD method, a combination of the μVT-MC and the boundary-driven NEMD, has been applied to simulating permeation of pure- and mixed-gases through membranes with slit-shaped pores composed of heterogeneous surfaces under the assumption of the local adsorption equilibrium at the ends of the membrane. The random heterogeneous surfaces were modeled by randomly removing a certain number of carbons of the first graphite basal plane. Methane and ethane were selected for permeating gases.

The dynamic behavior of gas molecules permeating through slit-shaped pores, with and without surface heterogeneity, may be characterized as the selective adsorption followed by surface diffusion (or flow) as properly stated by Rao and Sircar [1993]. It was observed that molecules were found more frequently in the center region of the pore with an increase in the surface heterogeneity since molecules were apt to climb potential barriers made by heterogeneous sites.

The mass-transfer coefficients, defined by the ratio of the molar flux to the pore density at the feed side, were found to decrease significantly with a small increase in the surface heterogeneity because of an increase in frequency of changes in direction due to molecular collisions onto heterogeneous sites. The mass-transfer coefficient of methane in pure gas permeation was larger than that of ethane. In the case of mixed-gas permeation, however, the mass-

transfer coefficient of methane decreased and became almost identical to that of ethane; in other words, methane molecules collided with surrounding ethane molecules in such a way that the mass-transfer coefficient became almost the same as that of ethane. It is also worthy of noting that, in the mixed-gas permeation, the permeation of methane was much suppressed by ethane molecules due to the competitive adsorption of ethane at the feed side.

The pore densities at the feed side of membrane, ρ_H, decreased with increasing temperature and it increased with increasing the feed pressure. On the other hand, the mass-transfer coefficients increased with increasing temperature while they were almost constant for different feed gas pressures. As a whole, the permeation fluxes decreased with increasing temperature and they increased with increasing pressure regardless of surface heterogeneity. These may be typical characteristics for permeation of gases controlled by adsorption at the feed side.

Lastly, the permeability $\hat{P}$ decreased with increasing site fraction f_b in the present surface model; the value of for $f_b = 0.2$ was about one fifth value of $\hat{P}$ for $f_b = 0.0$. However, it is still three order times larger in magnitude than the estimated values of for the carbon membranes reported by Rao and Sircar [1993]. Therefore, real carbon membranes may have structures that provide much larger resistances for permeation of gases than the resistances obtained in the present random heterogeneous surface model.

Nomenclature

a_s	= surface area of a graphite basal unit	[m²]
f_b	= site fraction	[-]
J	= molar flux	[mol m⁻² s⁻¹]
k_B	= Boltzmann constant	[J K⁻¹]
L_{mem}	= membrane thickness ($= L_x/2$)	[m]
L_x, L_y, L_z	= lengths of a simulation box in x, y, and z-directions	[m]
m	= mass of a molecule	[kg]
P	= pressure	[Pa]
$\hat{P}$	= permeability	[mol m m⁻² s⁻¹ Pa⁻¹]
r	= distance	[m]
T	= temperature	[K]
W_p	= pore width	[m]
V	= volume	[m³]
y	= mole fraction of feed gas	[-]
z	= perpendicular distance between a molecule and a surface	[m]

α_{21}	= selectivity defined by fluxes	[-]
$\alpha_{21}^{(eq)}$	= selectivity defined by equilibrium densities	[-]
ε	= LJ energy parameter	[J]
ρ	= density	[mol m⁻³]
σ	= LJ size parameter	[m]

<Subscripts>

1	= methane
2	= ethane

ij = pair of molecules i and j

k = component k

H = high pressure region

L = low pressure region

s = solid surface

<Super Subscripts>

(L) = L-th subcell

Reference

Allen, M. P. and D. J. Tildesley; Computer Simulation of Liquids, Clarendon Press, Oxford, England (1987)

Rao, M. B. and S. Sircar; "Nanoporous Carbon Membranes for Separation of Gas Mixtures by Selective Surface Flow," *J. Mem. Sci.*, **85**, 253-264 (1993)

Riccardo, J. L. and W. A. Steele; "Molecular Dynamics Study of Tracer Diffusion of Argon Adsorbed on Amorphous Surfaces," *J. Chem. Phys.*, **105**, 9674-9684 (1996)

Steele, W. A.; The Interaction of Gases with Solid Surfaces, Pergamon Press, Oxford, England (1974)

Steele, W. A.; "Computer Simulation of Surface Diffusion in Adsorbed Phases," *Studies in Surface Science and Catalysis*, **104**, 451-485 (1997)

Table 3-1   L-J parameters

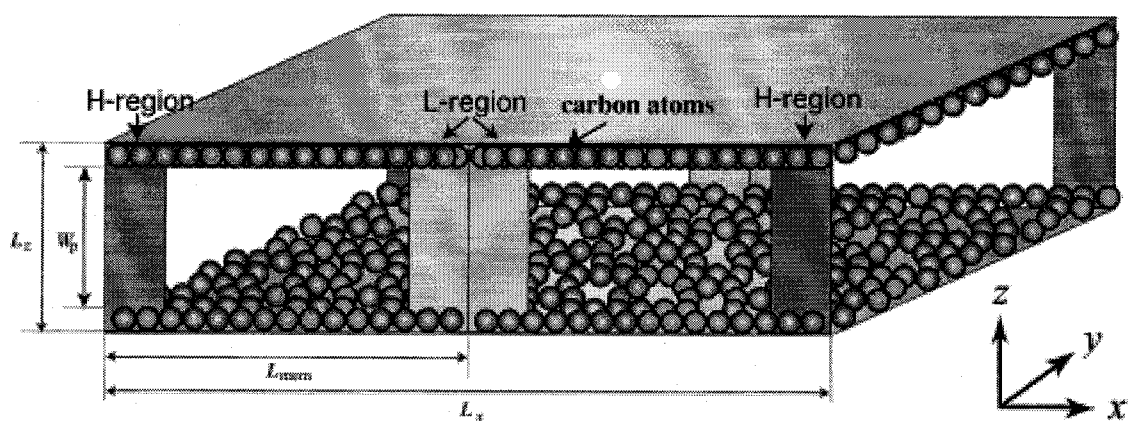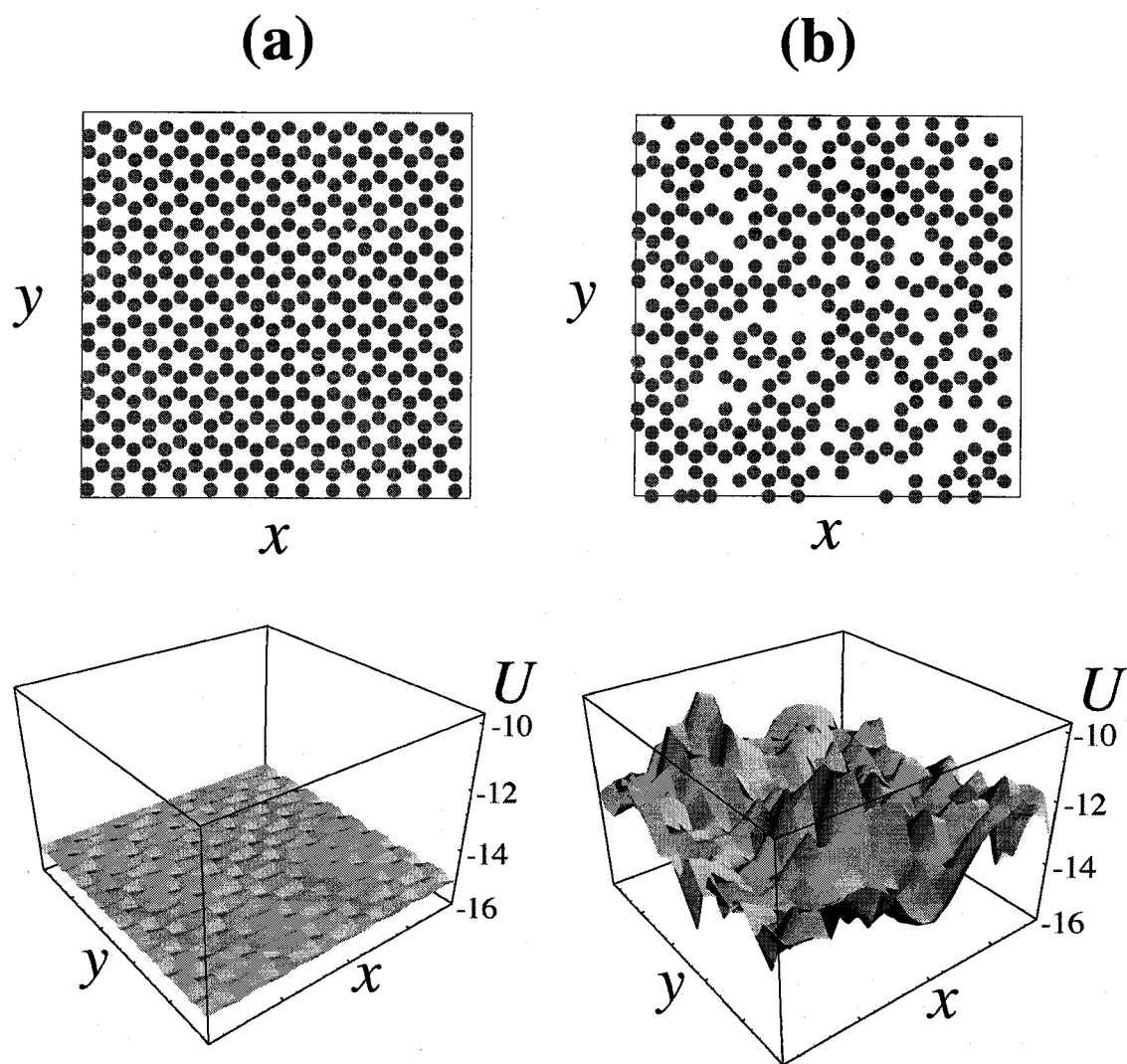|	σ [nm]	ε/k_B [K]
methane	0.3911	141.3
ethane	0.4496	226.2
carbon	0.340	28.0

Figure 3-1　Schematic diagram of simulation cell

Figure 3-2 Structures of random heterogeneous surfaces and lowest potential energy surface for ethane: f_b = (a) 0.0, (b) 0.192; numbers for U are given in kJ mol^{-1}
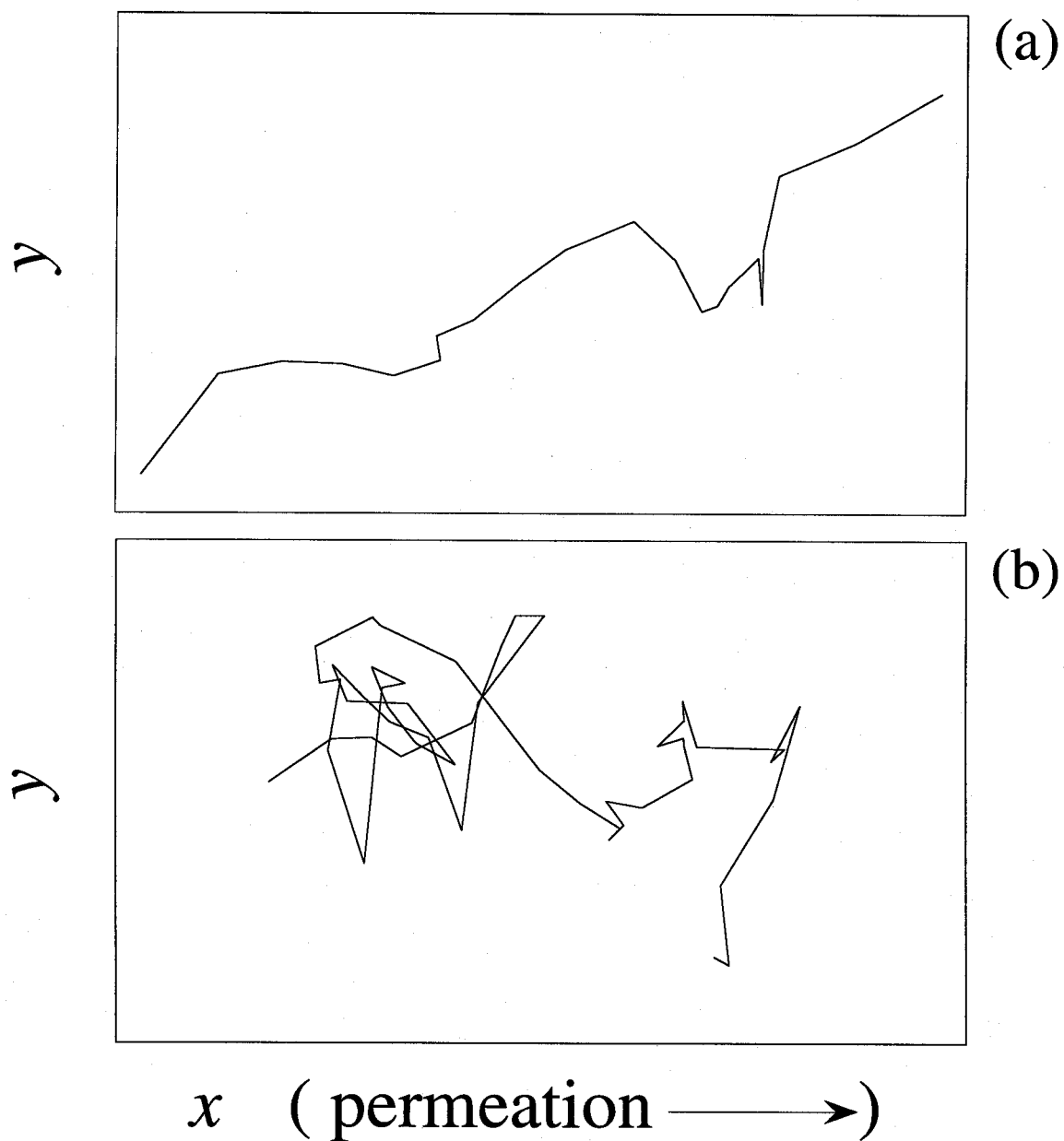
Figure 3-3 Trajectories of ethane molecule through random heterogeneous carbon membrane; Δt = (a) 20 ps, (b) 50 ps, f_b = (a) 0.0, (b) 0.192, ΔP = 0.5 MPa, T = 298 K, W_p = 2.347 nm
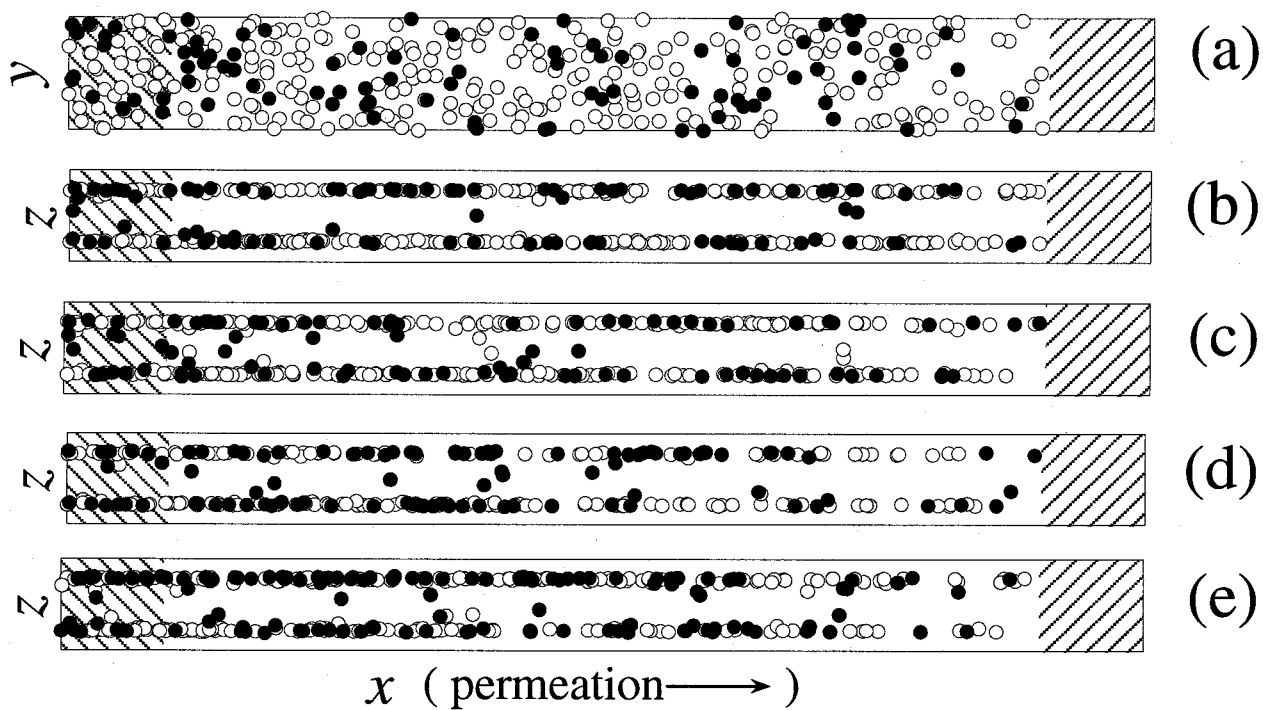
Figure 3-4 Snapshots of molecular configurations for permeation of binary
mixture ($\bullet$: methane, $\bigcirc$: ethane); f_b = (a,b) 0.0, (c) 0.041, (d) 0.094,
(e) 0.185, ΔP = 0.5 MPa, T = 298 K, W_p = 2.347 nm
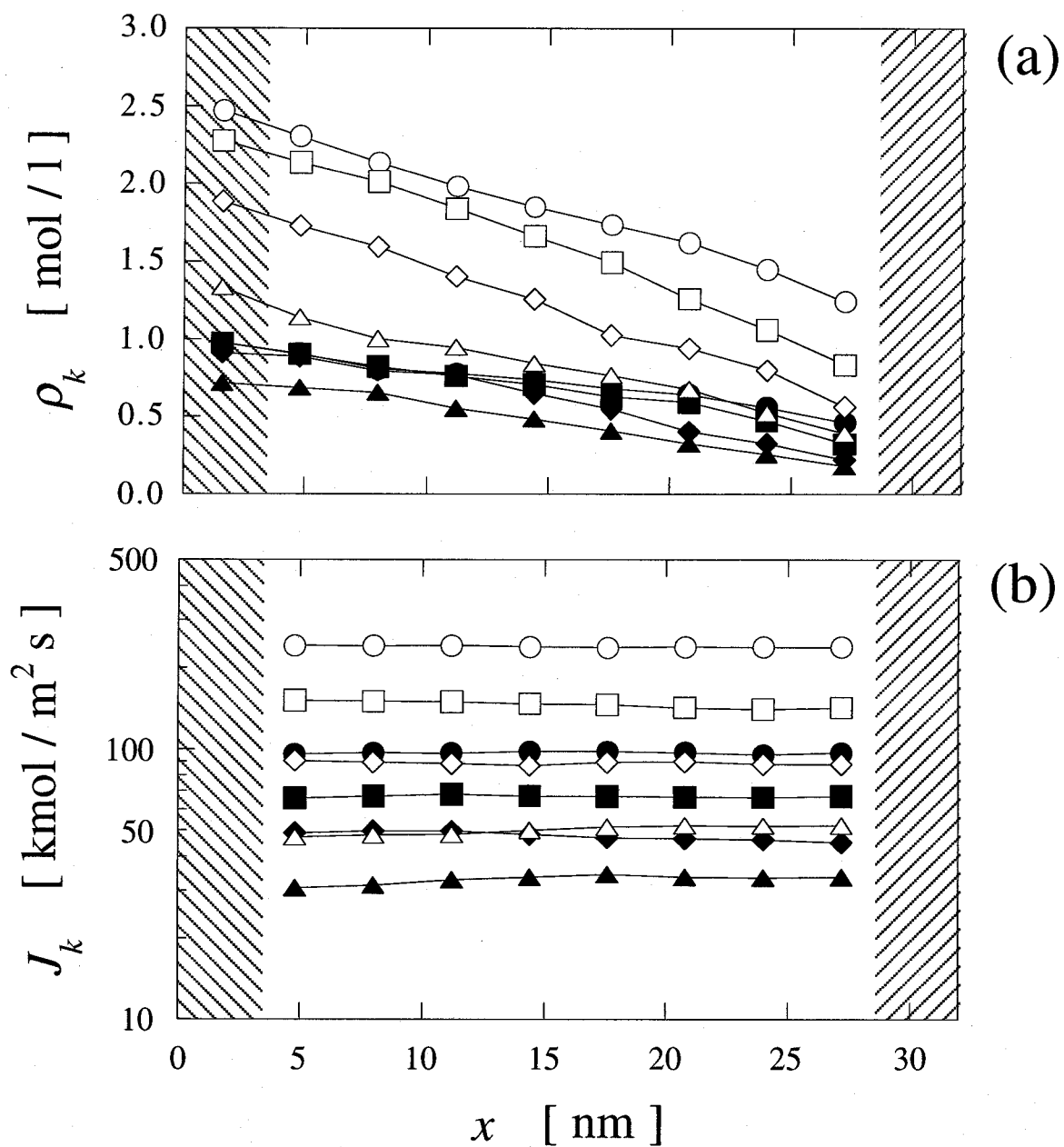
Figure 3-5   Profiles of (a) density and (b) molar flux of binary mixture (methane <closed keys> : 0.8 + ethane <open keys> : 0.2); f_b = ($\bullet$, $\bigcirc$) 0.0, ($\blacksquare$, $\square$) 0.041, ($\blacklozenge$, $\lozenge$) 0.094, ($\blacktriangle$, $\triangle$) 0.185, ΔP = 0.5 MPa, T = 298 K, W_p = 2.347 nm
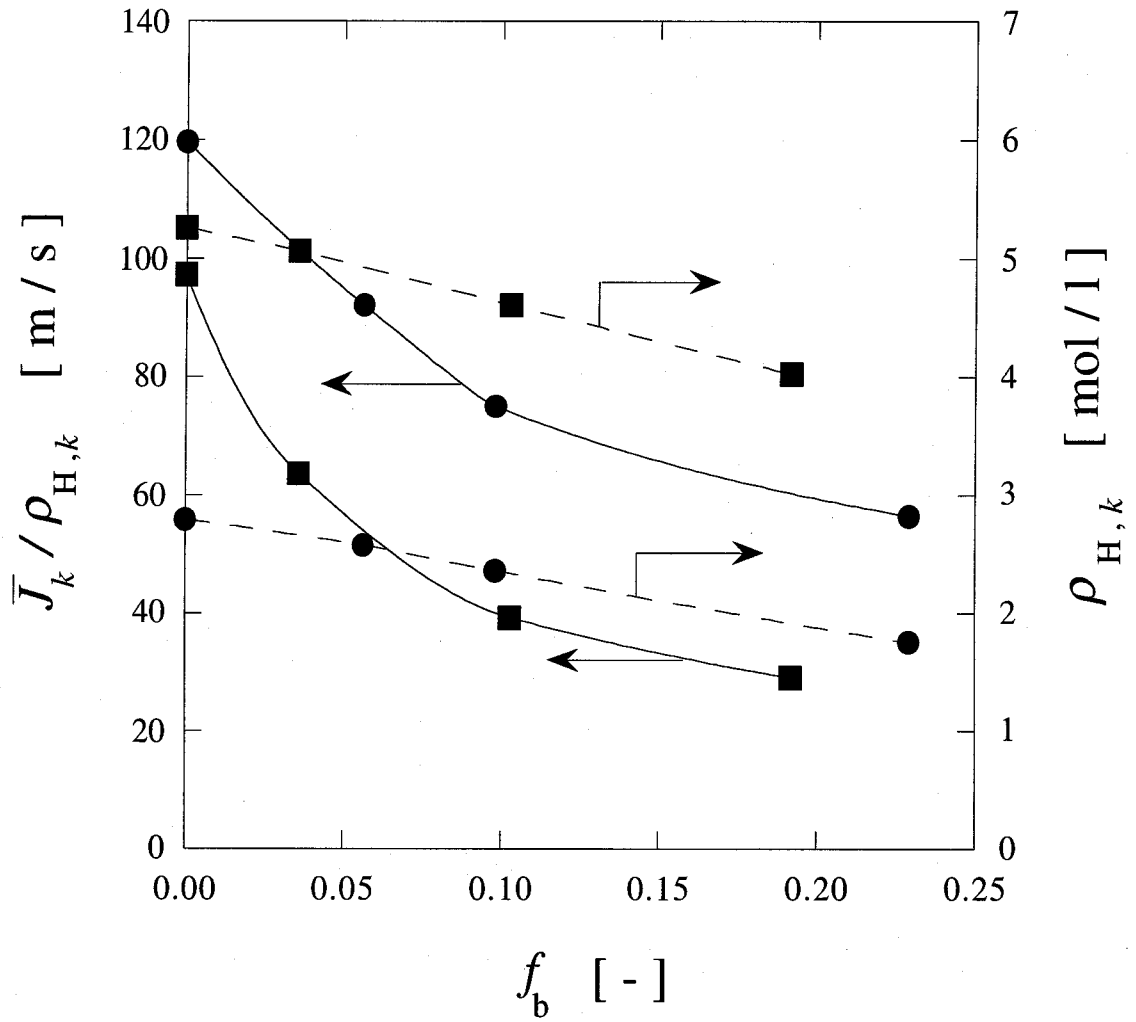
Figure 3-6 Effect of site fraction f_b on $\overline{J} / \rho_H$ and ρ_H of pure gases (● : methane, ■ : ethane); $\Delta P = 0.5$ MPa, $T = 298$ K, $W_p = 2.347$ nm
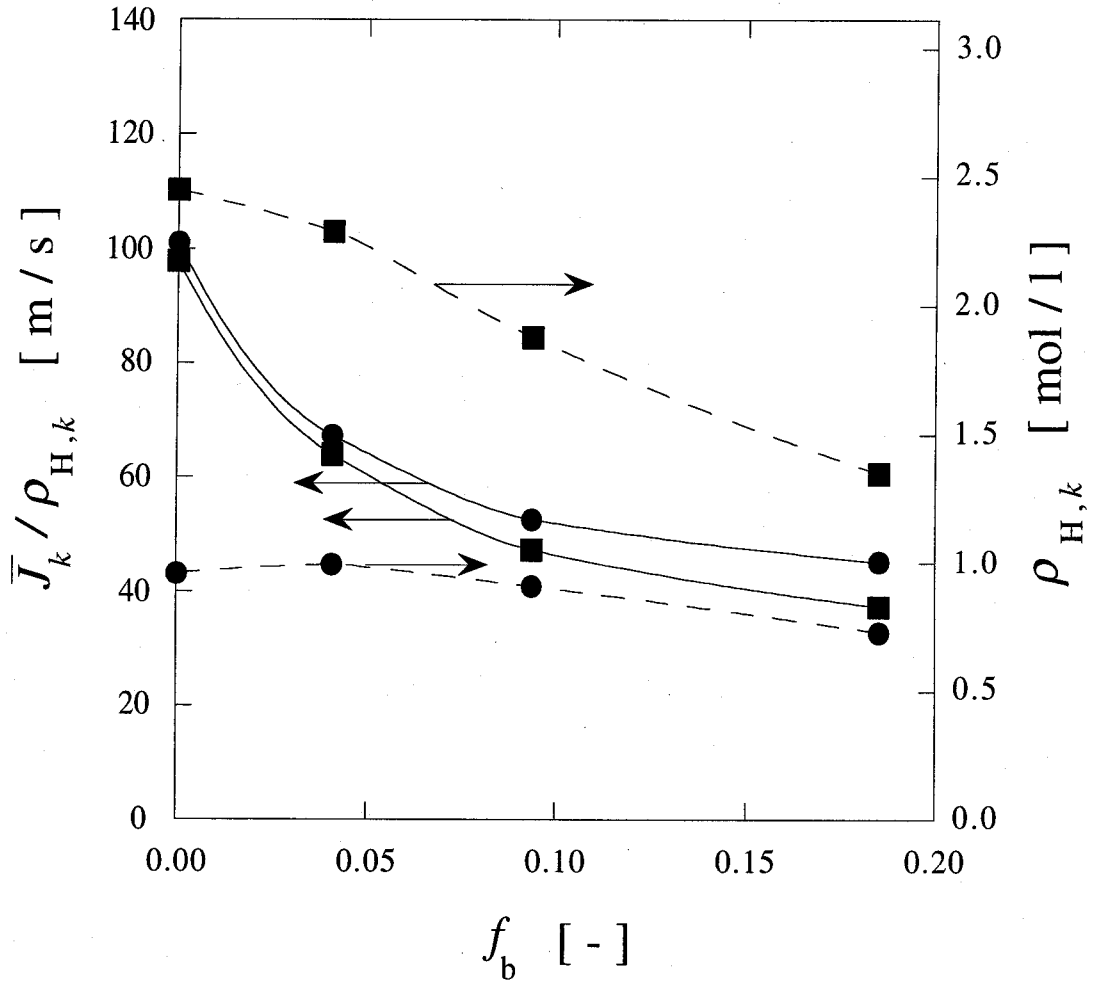
Figure 3-7   Effect of site fraction f_b on $\bar{J} / \rho_H$ and r_H of binary mixture (● :
methane, ■ : ethane); $\Delta P = 0.5$ MPa, $T = 298$ K, $W_p = 2.347$ nm
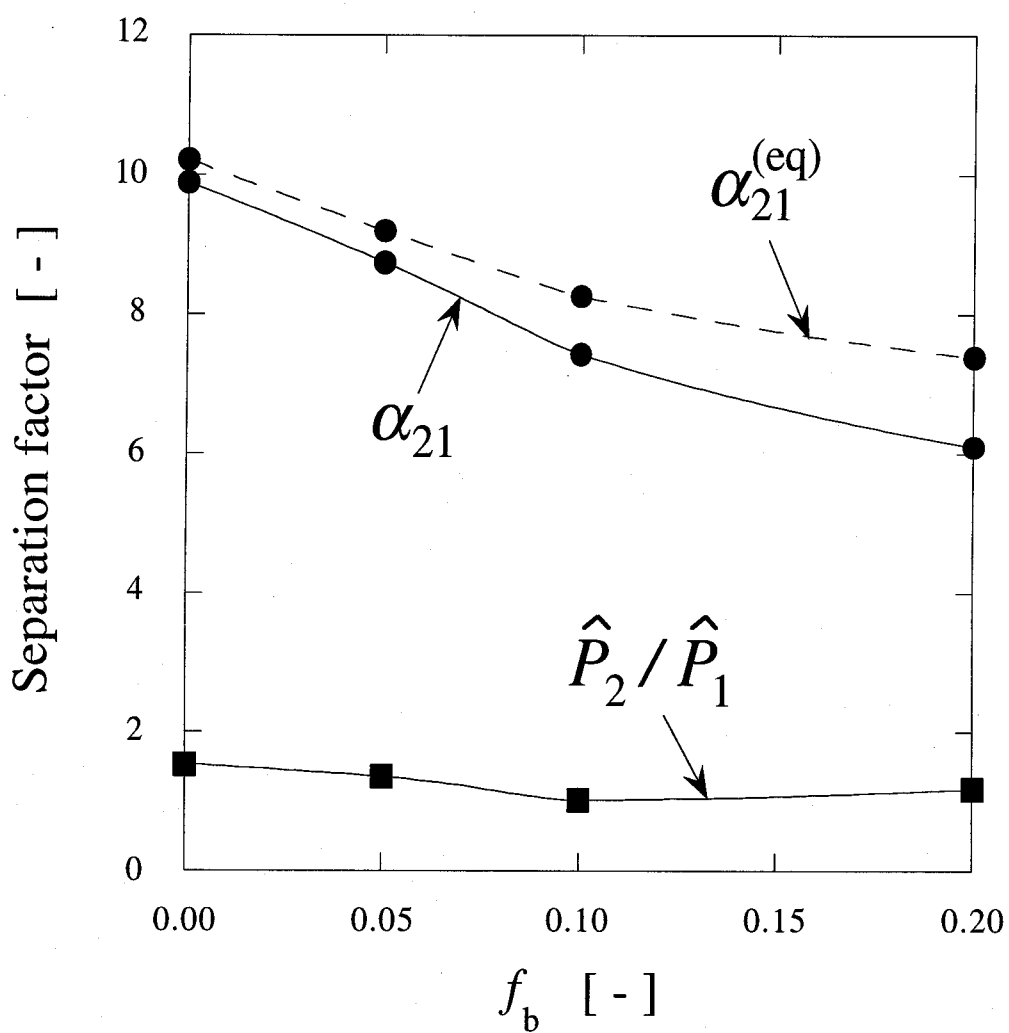
Figure 3-8 Effect of site fraction f_b on separation factors; $\Delta P = 0.5$ MPa, $T = 298$ K, $W_p = 2.347$ nm
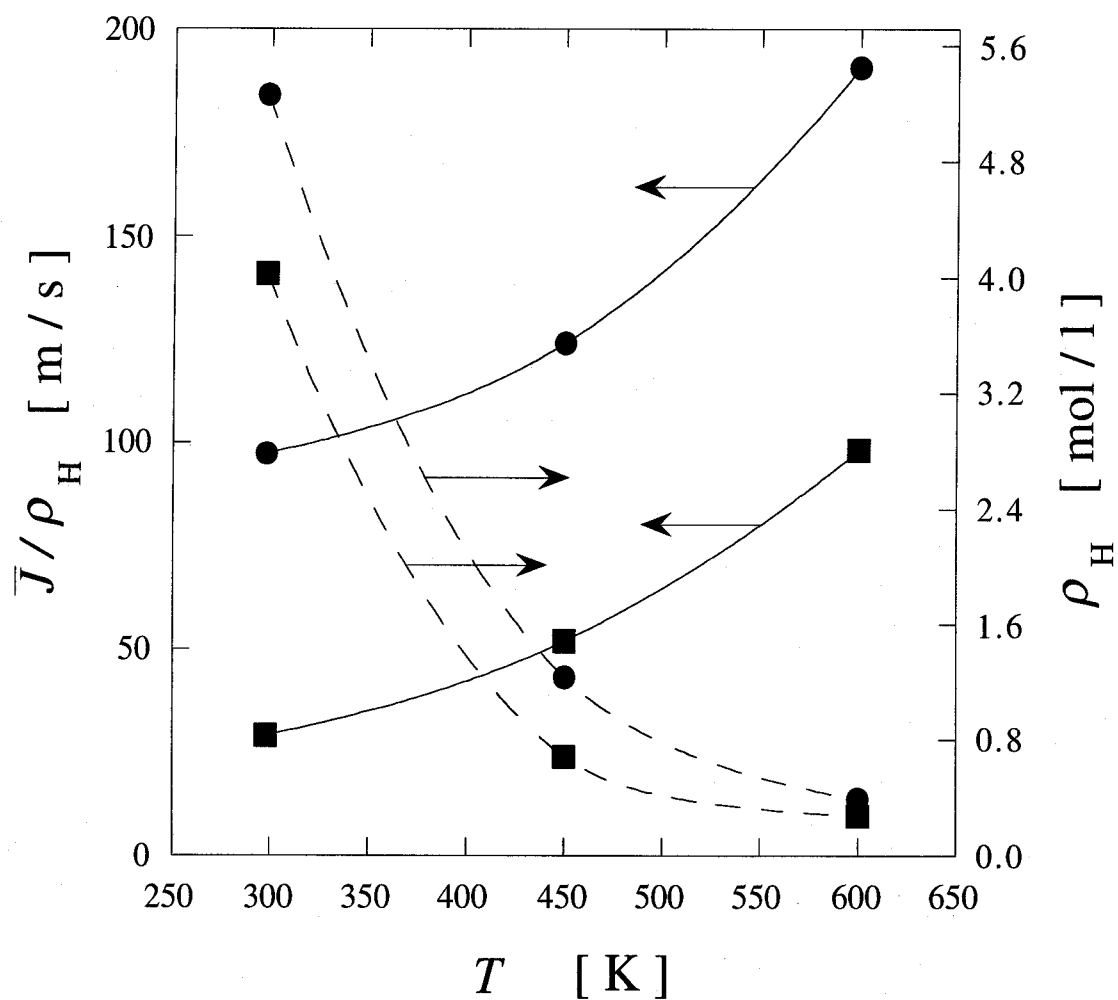
Figure 3-9　Effect of temperature on $\overline{J} / \rho_{\mathrm{H}}$ and ρ_{H} of pure ethane; $f_{\mathrm{b}} =$ (●) 0.0, (■) 0.20, $\Delta P = 0.5$ MPa, $W_{\mathrm{p}} = 2.347$ nm
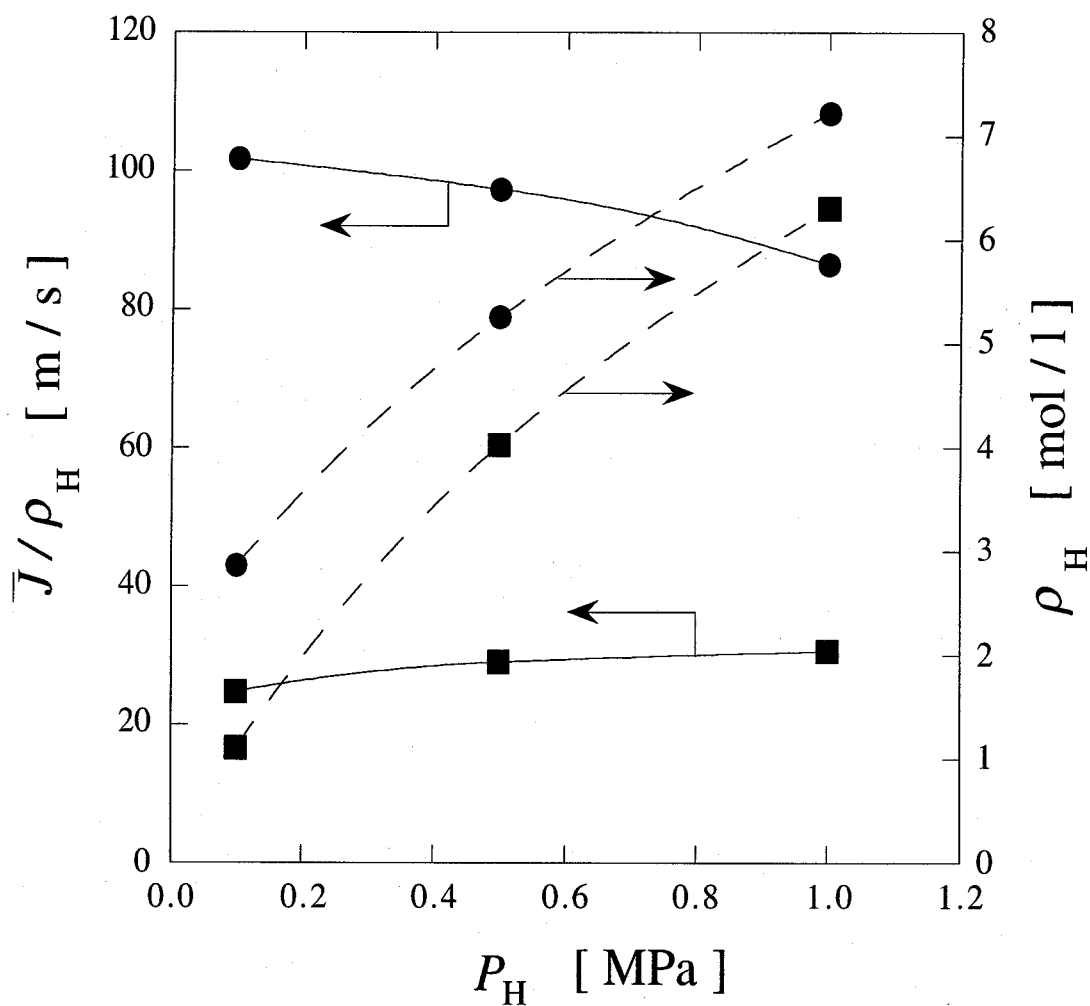
Figure 3-10 Effect of pressure at H-region on $\overline{J} / \rho_H$ and ρ_H of pure ethane; f_b = (
●) 0.0, (■) 0.20, T = 298 K, W_p = 2.347 nm

Chapter 4
Gas Permeation through Carbon Membranes
with Belt-like Heterogeneous Surfaces

4.1 Introduction

Chapter 3 dealt with the effects of surface heterogeneity on gas permeation through carbon membranes with slit-shaped pores having random heterogeneous surfaces. An interasting feature of the simulation results was a large decrease in permeation fluxes due to an increase in frequency of molecular collisions onto the heterogeneous sites. The densities in equilibrium with feed gases decreased almost linearly with the increase in surface heterogeneity, though the decrease was not so large as that in permeation fluxes. In the case of a binary mixture, permselectivity of a more adsorptive substance, which was much larger than the ideal separation factor, was found to change only slightly with an increase in the surface heterogeneity.

Zeolites are known to have cages and/or channel intersections connected to each other by channels or windows [Catlow, 1992]. At the channels or windows, there are usually potential barriers for permeating molecules; that is, permeating molecules must climb over the potential barriers in order to move to adjacent cages or channel intersections. This situation for permeating molecules is different from permeation through the slit-shaped pore with random heterogeneous surfaces where molecules can move to avoid higher potential barriers. In order to mimic the potential barriers that molecules must overcome, a new surface model with belt-like potential barriers is made in a computer.

The present chapter focuses on gas permeation through carbon membranes composed of heterogeneous surfaces with belt-like potential barriers.

Comparisons are made with simulation results for the belt-like and random heterogeneous surfaces to investigate the effects of surface heterogeneity and surface structures on gas permeation.

4.2 Simulation Method

4.2.1 The mVT-NEMD

The μVT-NEMD method was employed for simulating permeation of gases through a membrane. **Figure 4-1** shows a schematic diagram of the simulation cell used in the present chapter. The pore width (W_p) is defined as the distance subtracted from the distance between the centers of carbon atoms on the first layer of each surface wall by the van der Waals diameter of carbon atom. There are two symmetrical boxes, which have two controlling regions: H-regions and L-regions, in the simulation cell in order to satisfy the periodic boundary condition [Allen and Tildesley, 1987]. Throughout the simulation run, the densities and the compositions in the H-regions are kept constant so as to be in equilibrium with the feed gas at a given pressure and composition, while those in the L-regions are kept at zero. The insertion and destruction algorithms of the μVT-MC method are implemented for maintaining the densities in the H-regions. Molecules move from an H-region to an L-region through a conventional molecular dynamics (leap-frog) algorithm. The molecules which enter into the L-regions are removed immediately. The molecular velocities are rescaled independently in three directions after 20 steps so as to keep the temperature at a specified value (T). The time step is 10 fs. The 10,000 steps is discarded and the next 30,000 steps is collected for ensemble averaging. In a simulation run, the length of the y-direction (L_y) is adjusted so as to contain about 1,000 to 2,000 molecules in the elementary cell.

4.2.2 Belt-like heterogeneous surfaces

The upper and lower surfaces in Fig. 4-1 are the slit-shaped pore surfaces composed of graphite basal planes. The belt-like heterogeneous surfaces are made by removing carbon atoms on the first layer in a line vertically to the x-direction (permeate direction). Intermolecular interactions between molecule-molecule and between molecule-carbon atom on the first plane of the wall are represented by the 12-6 Lennard-Jones (LJ) potential function as

$$\phi_{ij}(r) = 4\varepsilon_{ij}\left[\left(\frac{\sigma_{ij}}{r}\right)^{12} - \left(\frac{\sigma_{ij}}{r}\right)^{6}\right] \tag{4-1}$$

where r is the distance between molecules i and j (or molecule i and atom j); ε_{ij} and σ_{ij} are potential parameters for a pair i and j. The second and subsequent graphite planes are presumed to be left intact. So, their interactions with permeating molecule i are represented by the 10-4-3 potential [Steele, 1974].

$$\phi_{is}(z) = 4\pi A_{is}\left[\frac{2}{5}\left(\frac{\sigma_{is}}{z}\right)^{10} - \left(\frac{\sigma_{is}}{z}\right)^{4}\right] - \frac{\sigma_{is}^{4}}{3\Delta(z+0.61\Delta)^{3}} \tag{4-2}$$

where A_{is} $(=\varepsilon_{is}\sigma_{is}^{2}/a_{s})$ is a constant, a_{s} the surface area of a graphite basal unit, Δ is the spacing between adjacent graphite basal planes, and z is the distance between permeating molecule i and the second graphite plane. Pure and mixed gases of methane (1) and ethane (2) are used as permeating gases; the LJ param-

eters for the two gases and the carbon are summarized in **Table 4-1**. The potential parameters for each gas are determined from the critical constants (T_c, P_c) by using the relations for the pure LJ fluid [Nicolas, 1979]. Those for solid carbon are taken from the work of Steele [1973, 1974]. The cross parameters are calculated from the Lorentz-Berthelot rule. **Figures 4-2a** and **4-2b** show a schematic diagram of one unit of surface carbons and the minimum potential energy surface for an ethane molecule exerted from the upper and lower surfaces, respectively. The length of the unit in the x-direction was fixed at 4.181 nm. It is observed that a split peak of potential energy around the area of removed carbon atoms. Therefore, the permeating molecules must climb up this potential hill, which is called the potential barrier, in order to permeate through the pore. A downward cusp of the split peak is due to interactions exerted from the edge carbons and the second graphite plane carbons. As a measure of surface heterogeneity, the potential barrier designated as $\Delta E_B/kT_0$ are used, where ΔE_B is the difference between the highest and the lowest potential energies for an ethane molecule on the minimum potential energy surface and T_0 is 298 K. **Figures 4-3a** to **4-3e** show schematic diagrams of five configurations of carbon atoms on the first layer used in the present work. Figure 4-3a is an original graphite carbon surface, and Figs. 4-3b to 4-3e are unit surfaces made by removing one to four lines of carbon atoms sequentially. The d_b is defined as the minimum distance between centers of edge carbon atoms, and the characteristic potential barriers $(\Delta E_B/kT_0)$ are listed in the figure caption. It is noted that the permeation molecules cannot completely drop in the belt-like gaps since the effective belt widths $(d_b^e = d_b - \sigma_{carbon})$ are always smaller than the van der Waals diameters of each permeation molecule. It is also noted that the lowest potential energies for methane and ethane molecules are -11.82 kJ/mol and -17.79 kJ/mol, respectively. Five surface units are arranged in the permeate direction (x-direction) as

shown in Fig. 4-1, including the H-region and the L-region. Therefore, three middle units are considered to be free from the end effects due to manipulation of insertion/destruction of molecules.

4.3 Results and Discussion

4.3.1 Effect of the potential barrier

Simulations have been carried out for pure- and mixed-gases permeation through slit-shaped pores with belt-like heterogeneous surfaces, and the simulation results are compared with those for random heterogeneous surfaces described in the previous chapter. The pure gases chosen are methane and ethane, and the binary gas is a mixture of methane (1) + ethane (2) whose composition is set at $y_1 = 0.8$. All simulations in this section are performed by varying the potential barrier under the following conditions: $T = 298$ K, $P_H = 0.5$ MPa, $W_p = 2.347$ nm. **Figures 4-4a** and **4-4b** show snapshots for pure ethane molecules permeating through slit-shaped pores (a) with the graphite basal plane surfaces ($\Delta E_B = 0.0$) and (b) with the surface of the belt-like potential barrier: $\Delta E_B/kT = 2.98$. The left hand side is the H-region and the right hand side is the L-region. The openings in the top and bottom bars in Fig. 4-4b represent the regions where carbon atoms are removed. They clearly suggest that molecular movement in the two pores is characterized by the surface flow. In Fig. 4-4b, it is observed that many molecules appear in the center region of the pore near the location of potential barriers, indicating that they climb up and down the potential barriers.

Figures 4-5a and **4-5b** show profiles of densities and molar fluxes for permeation of pure ethane gas through carbon membranes with various potential barriers: $\Delta E_B/kT = 0.0$, 1.10, 1.94, 2.56 and 2.98. In these figures, the areas with oblique lines on the left and right sides indicate the H-region and the L-

region, respectively; the five gray bars indicate regions where carbon atoms are removed. The densities decrease from the H-region to the L-region. The densities in the four gray regions where the potential barriers are located decrease largely, and the decrease is larger as the potential barrier is higher. On the other hand, the molar fluxes are almost constant, which indicates that dynamically stationary states have been achieved in each simulation run. The molar flux decreases with increasing potential barrier. Other simulation runs for pure methane and for a mixed gas also show the same tendency as shown in Figs. 4-5a and 4-5b.

The permeation resistance (R) as shown in Eq. (4-3) is defined by use of the molar flux (J) and the density difference ($\rho_H - \rho_L$), which represents the driving force for mass transfer in the pore.

$$J = \frac{1}{R}(\rho_H - \rho_L) \tag{4-3}$$

Figures 4-6a and 4-6b show effects of the potential barrier ($\Delta E_B/kT$) on the density at the H-region (ρ_H) and the permeation resistance (R) for permeation of pure gases. The ρ_H decreases slightly with increasing $\Delta E_B/kT$ due to the decrease in adsorption power of the surface. The ρ_H of ethane is always larger than that of methane because the adsorption energy of ethane is larger than that of methane. On the other hand, R increases with increasing $\Delta E_B/kT$. The permeation resistance at $\Delta E_B/kT = 2.98$ is about 10 times larger than that at zero potential barrier. The R of ethane is always larger than that of methane because the values of ΔE_B for methane are approximately 23—28 % smaller than those for ethane.

Figures 4-7a and 4-7b show effects of the $\Delta E_B/kT$ on the ρ_H and the R

for permeation of the mixed gas that $y_1 = 0.8$. The ρ_H of methane is almost constant, while that of ethane decreases with increasing $\Delta E_B/kT$. On the other hand, the two R curves for methane and ethane increase with increasing $\Delta E_B/kT$, though they are slightly different with those in the case of pure gas permeation. First, the two R curves are almost coincident when the $\Delta E_B/kT$ is less than 1.0, which suggests that the diffusion rates of each component are determined by the total density in the pore when the surface heterogeneity is small. In the case of a random heterogeneous surface, the same result as above mentioned was obtained as shown in the previous chapter. Secondly, a notable result shown in Fig. 4-7b is the large decrease in R for methane to permeate in the mixed gas when the potential barrier is high; that is, $\Delta E_B/kT = 2.98$. This fact is difficult to explain at the present moment.

The separation factor of permeation α_{21} is calculated from the molar fluxes and the compositions of the feed gas as

$$\alpha_{21} = \frac{J_2/J_1}{y_2/y_1} \tag{4-4}$$

The equilibrium separation factor $\alpha_{21}^{(eq)}$ and the ratio of permeability of pure ethane to that of methane, $\hat{P}_2/\hat{P}_1$ are also calculated; $\alpha_{21}^{(eq)}$ is defined by use of the pore densities at the H-region for the binary system and compositions of the feed gas as

$$\alpha_{21}^{(eq)} = \frac{\rho_{H,2}/\rho_{H,1}}{y_2/y_1} \tag{4-5}$$

and $\hat{P}_k$ for component k is defined as

$$\hat{P}_k = J_k L_{\text{mem}} / \left(P_{k,\text{H}} - P_{k,\text{L}} \right)$$ (4-6)

Figure 4-8 shows the effects of $\Delta E_\text{B}/kT$ on the separation factors. It is noted that the difference between α_{21} and $\hat{P}_2/\hat{P}_1$ is remarkable. This is ascribed to the competitive adsorption of ethane and methane. α_{21} decreases with increasing $\Delta E_\text{B}/kT$, while $\alpha_{21}^{(\text{eq})}$ has high values in the region of high potential barrier. Therefore, permselectivity is influenced by both adsorption equilibrium and mass transfer rates in the pore. In the case of a random heterogeneous surface (**Figure 4-9**), the curves of α_{21} and $\alpha_{21}^{(\text{eq})}$ decrease with increasing surface heterogeneity (f_b), and they are almost identical. The symbol f_b indicates the site fraction of the carbons randomly removed from the first graphite basal planes. In the case of a random heterogeneous surface, the permeating molecules can move to avoid the potential barrier, while permeating molecules must climb over the potential barriers produced on the belt-like heterogeneous surfaces. Therefore, mass transfer rate would become the deterministic factor for the separation of gases in the case of belt-like heterogeneous surfaces compared to the random heterogeneous surfaces.

4.3.2 Effect of temperature

Figures 4-10a and **4-10b** show the effect of temperature on the density at the H-region (ρ_H) and the molar flux (J) for pure ethane gas through a carbon membrane with a belt-like potential barrier ($\Delta E_\text{B} = 7.38$ kJ/mol) under various temperatures; $T = 298, 400, 500$ and 600 K. The ρ_H curve decreases with increasing T since the adsorption is an exothermic process. On the other hand, the

J curve has a minimum point at about 510 K. At temperatures lower than 510 K, the controlling factor of ethane permeation may be the adsorption density at the feed side, which decreases monotonically with increasing temperature. On the other hand, at temperatures higher than 510 K, the large increase of mass transfer rate of ethane may become the dominant factor for permeation. It should be noted that a similar experimental result was reported for ethane permeation through a silicalite membrane by Bakker et al. [1996], who reported that the permeance of ethane had a minimum value at about 600 K.

4.4 Summary

The dynamic behavior of permeating molecules through slit-shaped pores, with and without surface heterogeneity, may be characterized as selective adsorption followed by surface flow. In the case of high potential barrier surfaces, many molecules found in the center region of a pore near the belt-like potential barriers since they had to climb up and down.

The permeation resistance (R) increases almost exponentially with an increase in the potential barrier of each gas. The R for ethane is always larger than that for methane since the potential barrier for ethane is larger. In the case of a binary system, the R curves for methane and ethane are almost the same when $\Delta E_B/kT$ is less than 1.0; almost the same result has been obtained in the case of random heterogeneous surfaces. This may indicate that permeation rates of each mixed component are determined by the total density in the pore when the surface heterogeneity is weak, regardless of random or belt-like heterogeneous surfaces. However, in the case of belt-like heterogeneous surfaces, a large decrease in R for methane in the mixed gas permeation has been observed when the potential barrier is high. The explanation of this observation needs

further investigations.

The separation factor (α_{21}) is almost the same as the equilibrium separation factor ($\alpha_{21}^{(eq)}$) when $\Delta E_B/kT$ is small; however, it sharply decreases toward the ideal separation factor ($\hat{P}_2/\hat{P}_1$) when $\Delta E_B/kT$ increases. Therefore, in the case of belt-like heterogeneous surfaces, the separation factor is influenced by the mass transfer rates in the pore as well as the adsorption equilibrium. It is noted that, in the case of a random heterogeneous surface, the curves of α_{21} and $\alpha_{21}^{(eq)}$ are almost identical, and they slightly decrease with increasing surface heterogeneity.

Lastly, the curve of the molar flux of pure ethane against T has a minimum point where T is approximately 510 K. This observation may be interpreted as follows: at lower temperatures, the controlling factor of gas permeation may be adsorption density at the feed side, which decreases monotonically with increasing temperature. On the other hand, at higher temperatures, the increase of mass transfer rate causes the increase in molar flux.

Nomenclature

d_b	= minimum distance between centers of edge carbons	[m]
d_b^e	= effective belt width	[m]
f_b	= site fraction	[—]
J	= permeate flux	[mol m^{-2} s^{-1}]
L_{mem}	= membrane thickness	[m]
L_x, L_y, L_z	= lengths of simulation cell in x, y and z-directions	[m]
N_A	= Avogadro constant	[mol^{-1}]
P	= pressure	[Pa]
P_c	= critical pressure	[Pa]
$\hat{P}$	= permeability	[mol m m^{-2} s^{-1} Pa^{-1}]
r	= distance	[m]
R	= permeation resistance	[s m^{-1}]
T	= temperature	[K]
T_c	= critical temperature	[K]
W_p	= pore width	[m]
y	= mole fraction of feed gas	[—]
z	= perpendicular distance	
	between a molecule and the second graphite plane	[m]
α_{21}	= separation factor defined by the permeate fluxes	[—]
$\alpha_{21}^{(eq)}$	= separation factor defined by equilibrium densities	[—]
ΔE_B	= potential barrier	[J]
ε	= LJ energy parameter	[J]
ϕ	= potential energy	[J]
ρ	= density	[mol m^{-3}]

σ = LJ size parameter   [m]

<Subscripts>

1   = methane

2   = ethane

H   = H-region of simulation cell

k = component k

L   = L-region of simulation cell

s = carbon atom

References

Allen, M. P. and D. J. Tildesley; Computer Simulation of Liquids, Clarendon Press, Oxford, England (1987)

Bakker, W. J. W., F. Kapteijn, J. Poppe and J. A. Moulijn; "Permeation Characteristics of a Metal-Supported Silicalite-I Zeolite Membrane," *J. Mem. Sci.*, **117**, 57-78 (1996)

Catlow, C. R. A.; Modelling of Structure and Reactivity in Zeolites, Academic Press, London, England (1992)

Nicolas, J. J., K. E. Gubbins, W. B. Streett and D. J. Tildesley; "Equation of State for the Lennard-Jones Fluid," *Molec. Phys.*, **37**, 1429-1454 (1979)

Steele, W. A.; "The Interaction of Gases with Solid Surfaces," *Surface Sci.*, **36**, 317-352 (1973)

Steele, W. A.; The Interaction of Gases with Solid Surfaces, Pergamon Press, Oxford, England (1974)

Table 4-1   L-J parameters

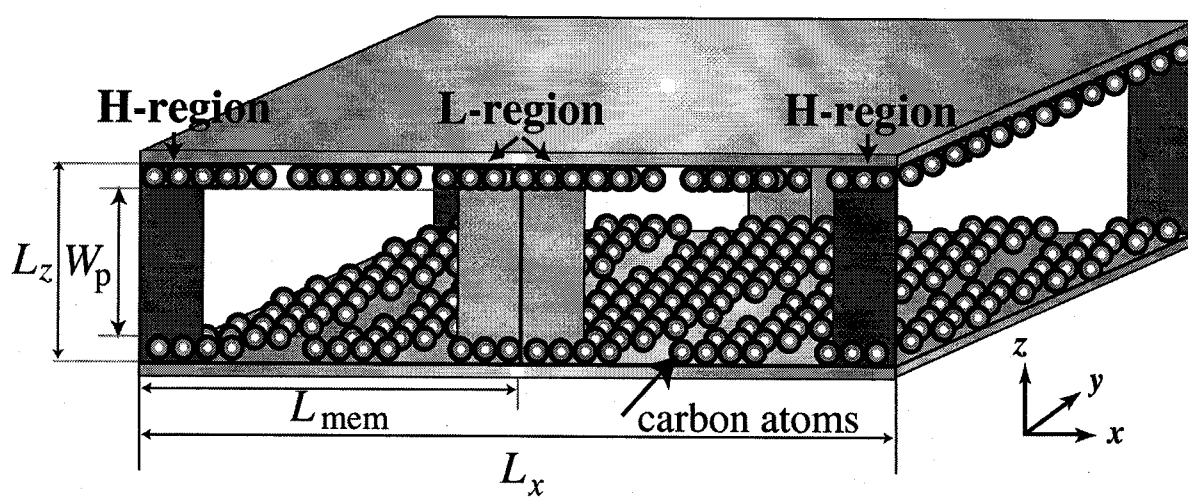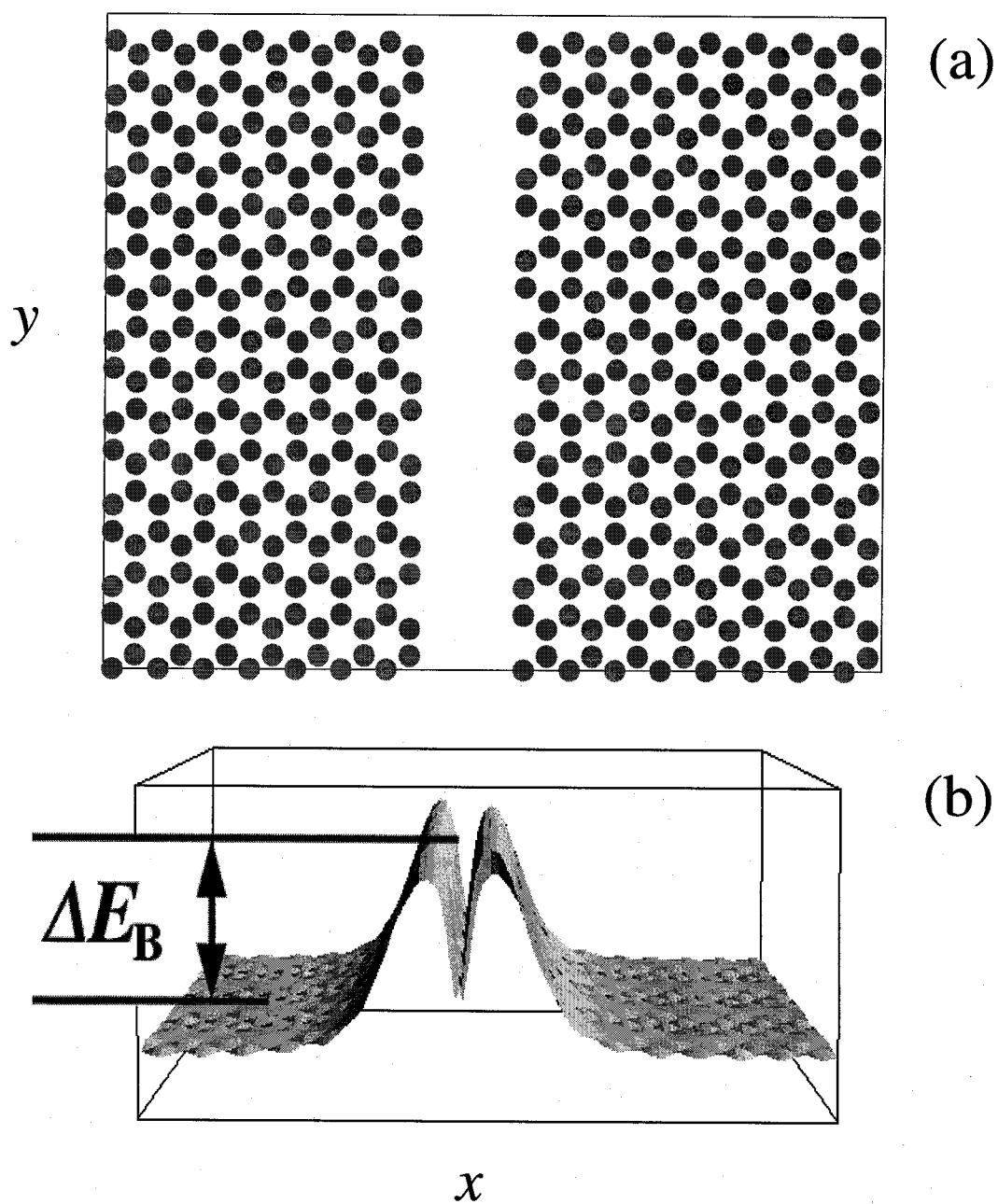|	σ [nm]	ε/k_B [K]
methane	0.3911	141.3
ethane	0.4496	226.2
carbon	0.340	28.0

Figure 4-1   Schematic diagram of simulation cell

Figure 4-2   (a) schematic diagram of carbon configuration and (b) minimum potential energy surface for molecule to feed from each surface
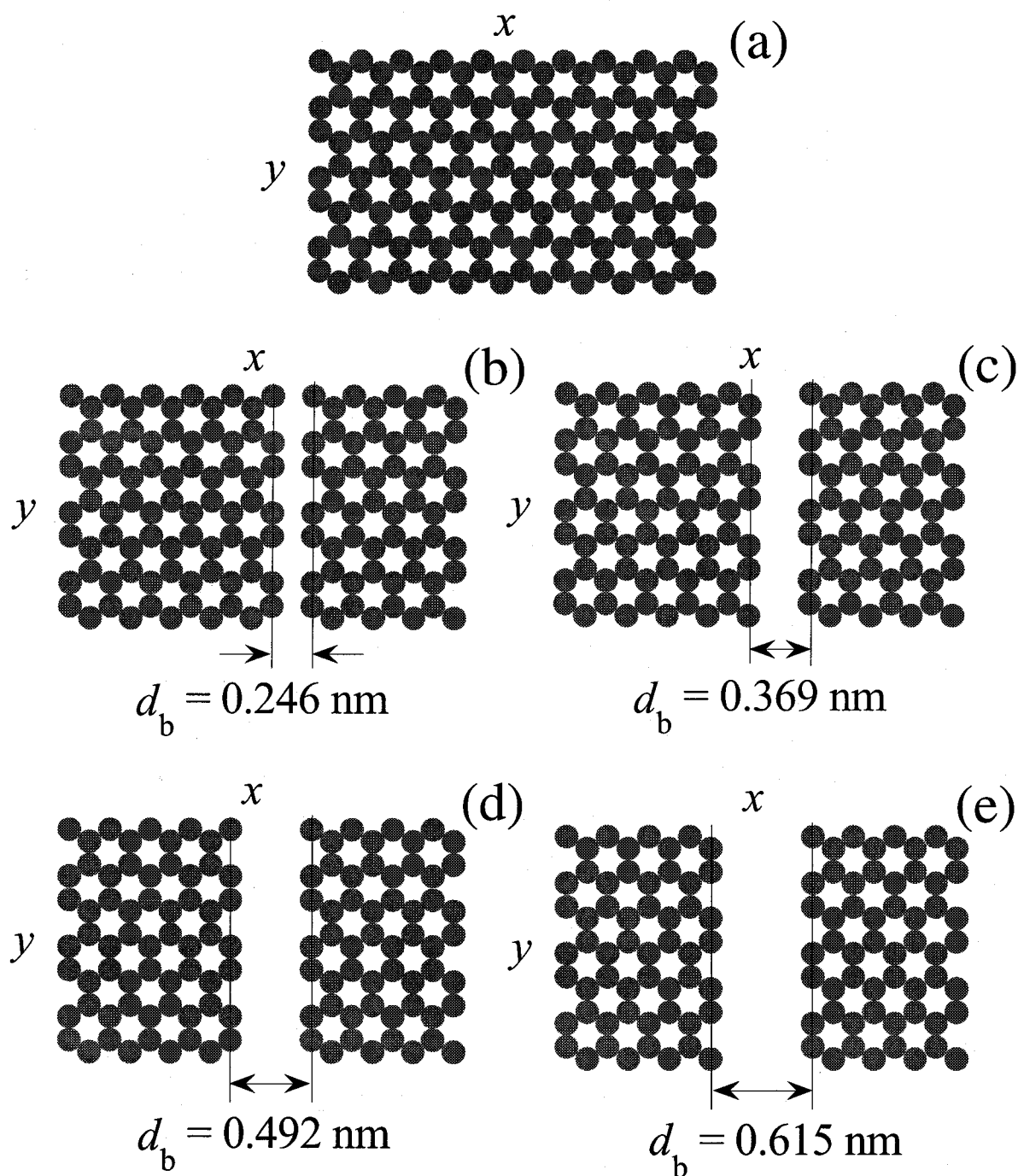
Figure 4-3 Schematic diagrams of configurations of carbon atoms on first layer; $\Delta E_B/kT_0$ = (a) 0.0, (b) 1.10, (c) 1.94, (d) 2.56, and (e) 2.98, $T_0 = 298$ K
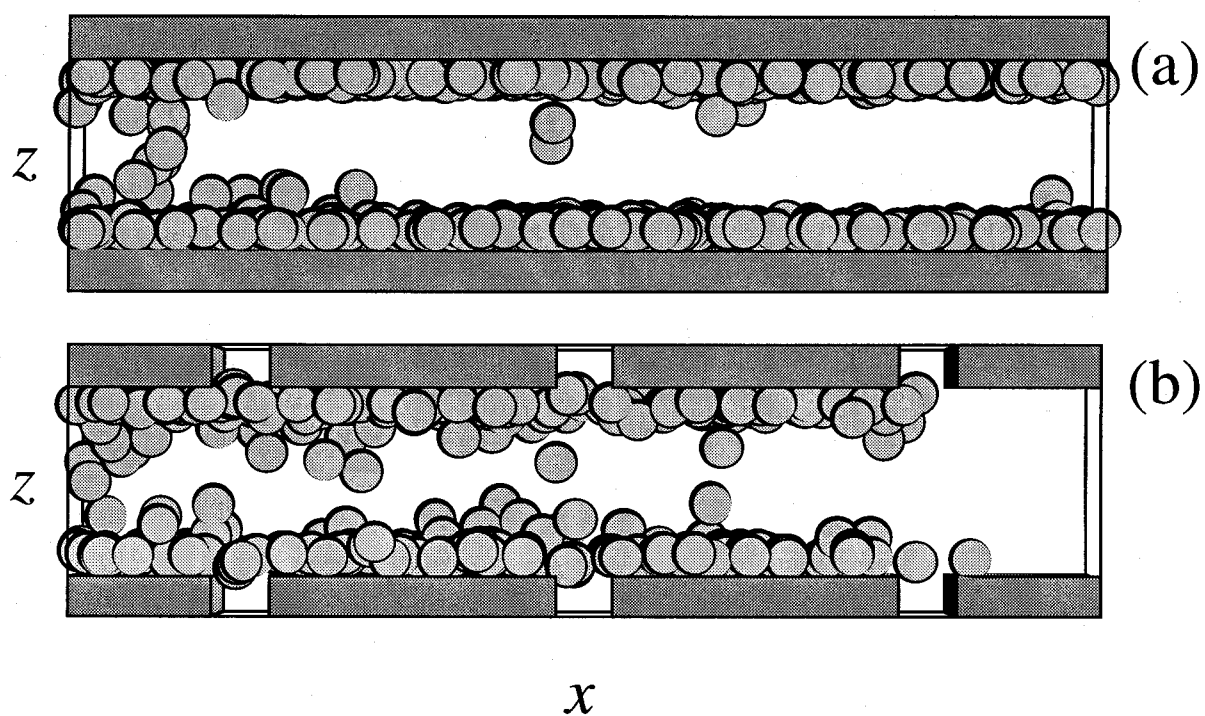
Figure 4-4 Snapshots for pure ethane gas permeating through slit-shaped carbon membrane with belt-like potential barrier; $\Delta E_B/kT$ = (a) 0.0 and (b) 2.98
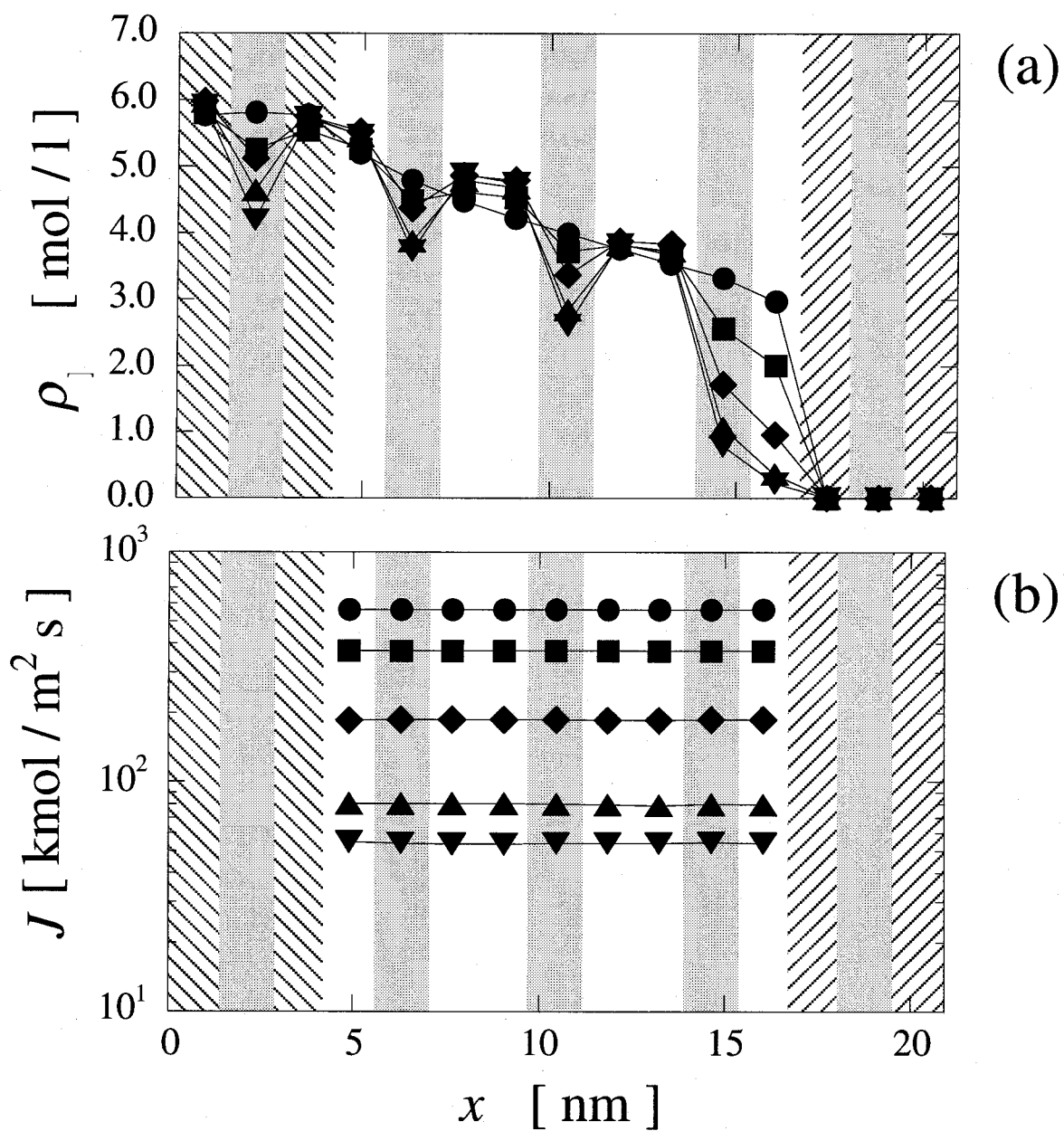
Figure 4-5 Profiles of (a) densities and (b) molar fluxes for permeation of pure ethane gas through carbon membranes with various belt-like potential barriers; $\Delta E_B/kT = $ (●) 0.0, (■) 1.10, (◆) 1.94, (▲) 2.56 and (▼) 2.98
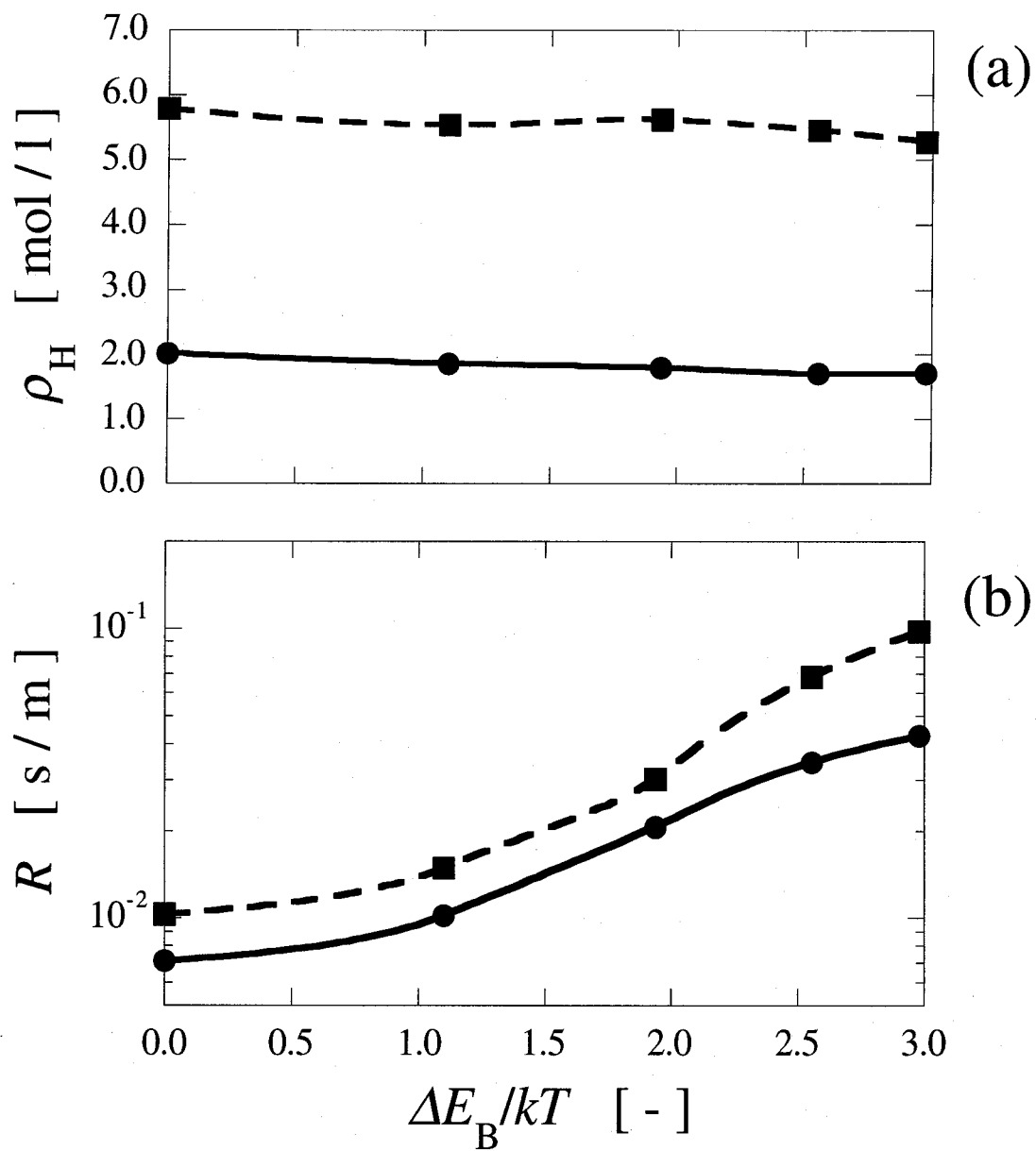
Figure 4-6   Effect of potential barrier on (a) density at H-region and (b) permeate
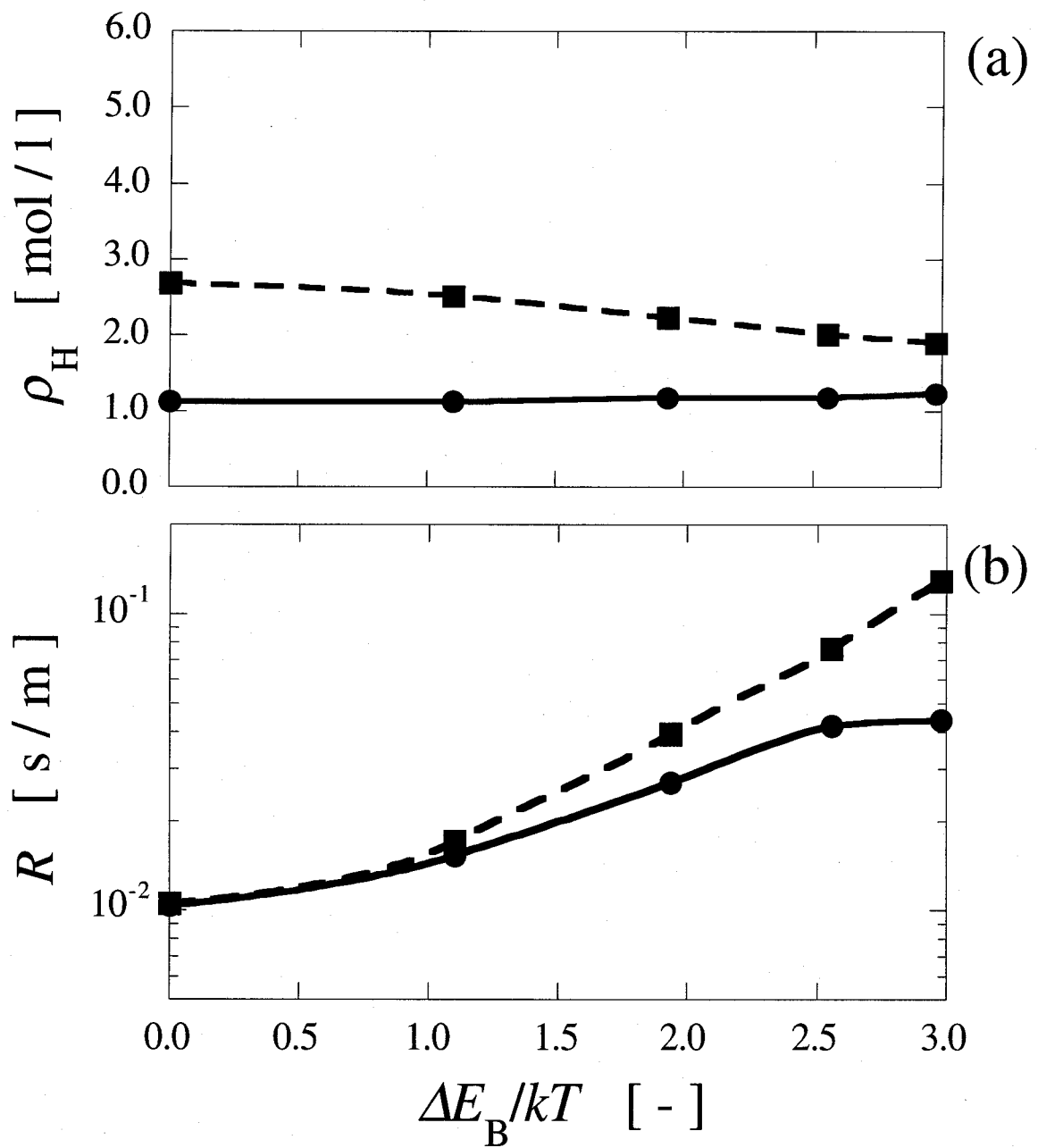resistance for permeation of pure gas; (●) methane, (■) ethane

Figure 4-7   Effect of the potential barrier on (a) density at H-region and (b) permeate resistance for permeation of mixed gas; (●) methane, (■) ethane
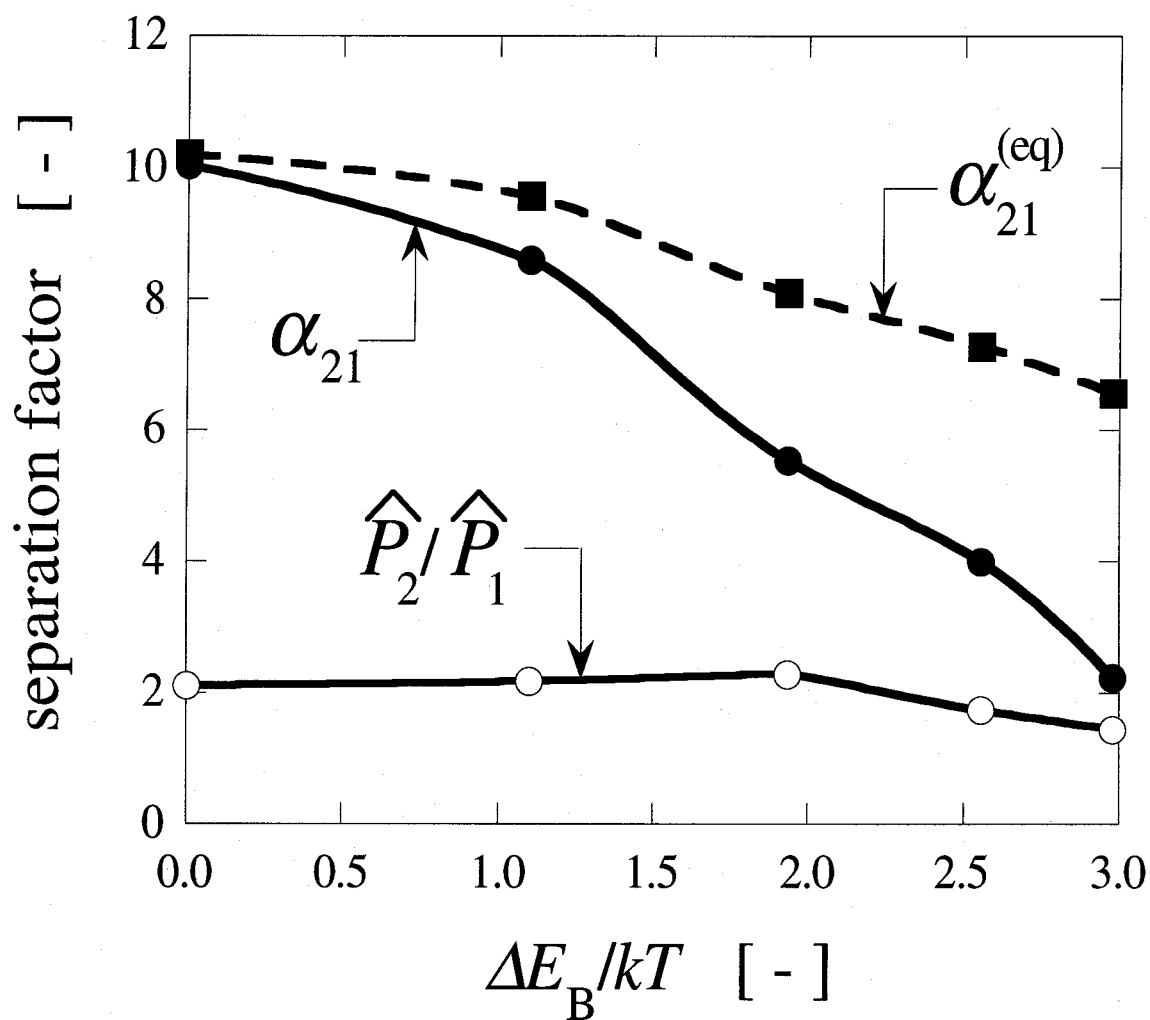
Figure 4-8   Effect of potential barrier on separation factors in case of belt-like
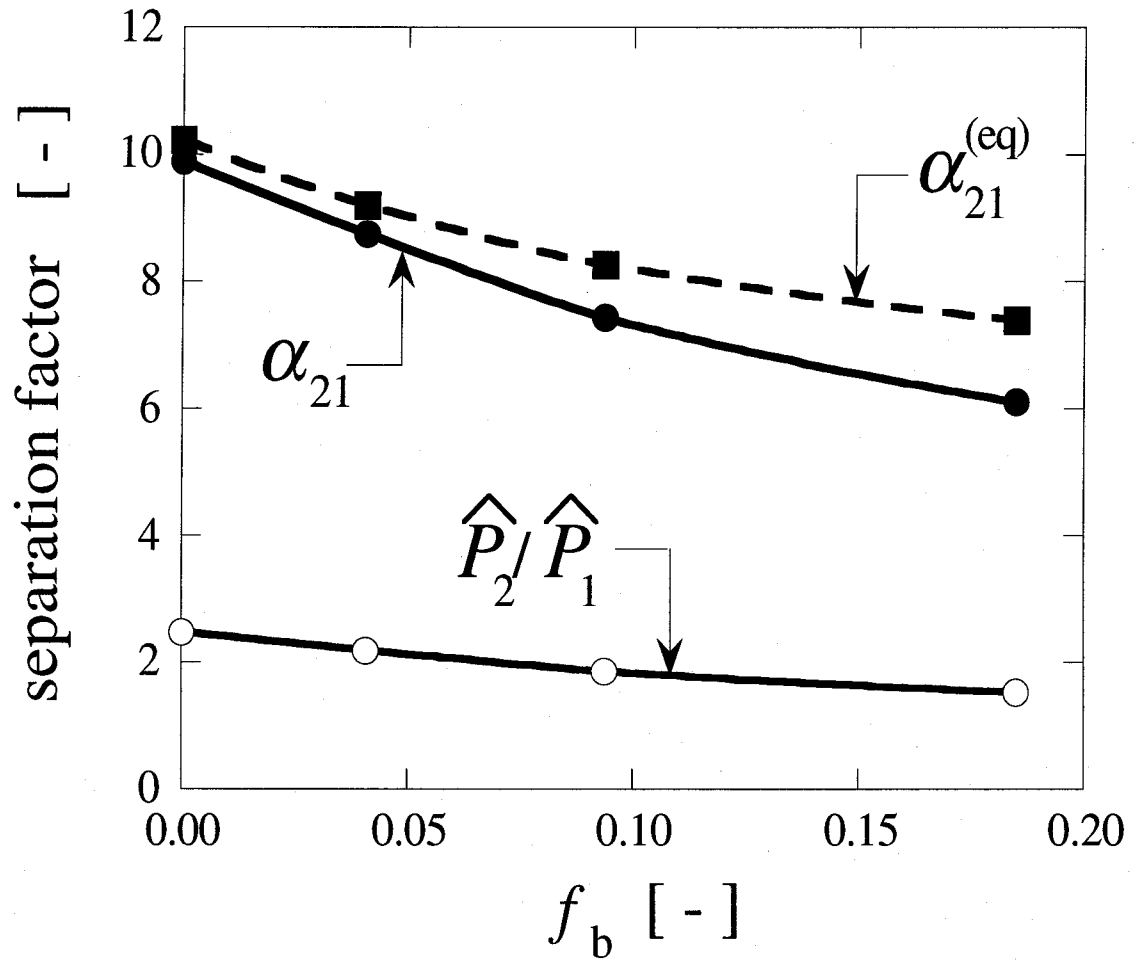heterogeneous surface; L_{mem} = 12.54 nm

Figure 4-9   Effect of site fraction on the separation factors in case of random heterogeneous surface; W_p = 2.347 nm, T = 298 K, ΔP = 0.5 MPa, L_{mem} = 25.58 nm, [chapter 3]
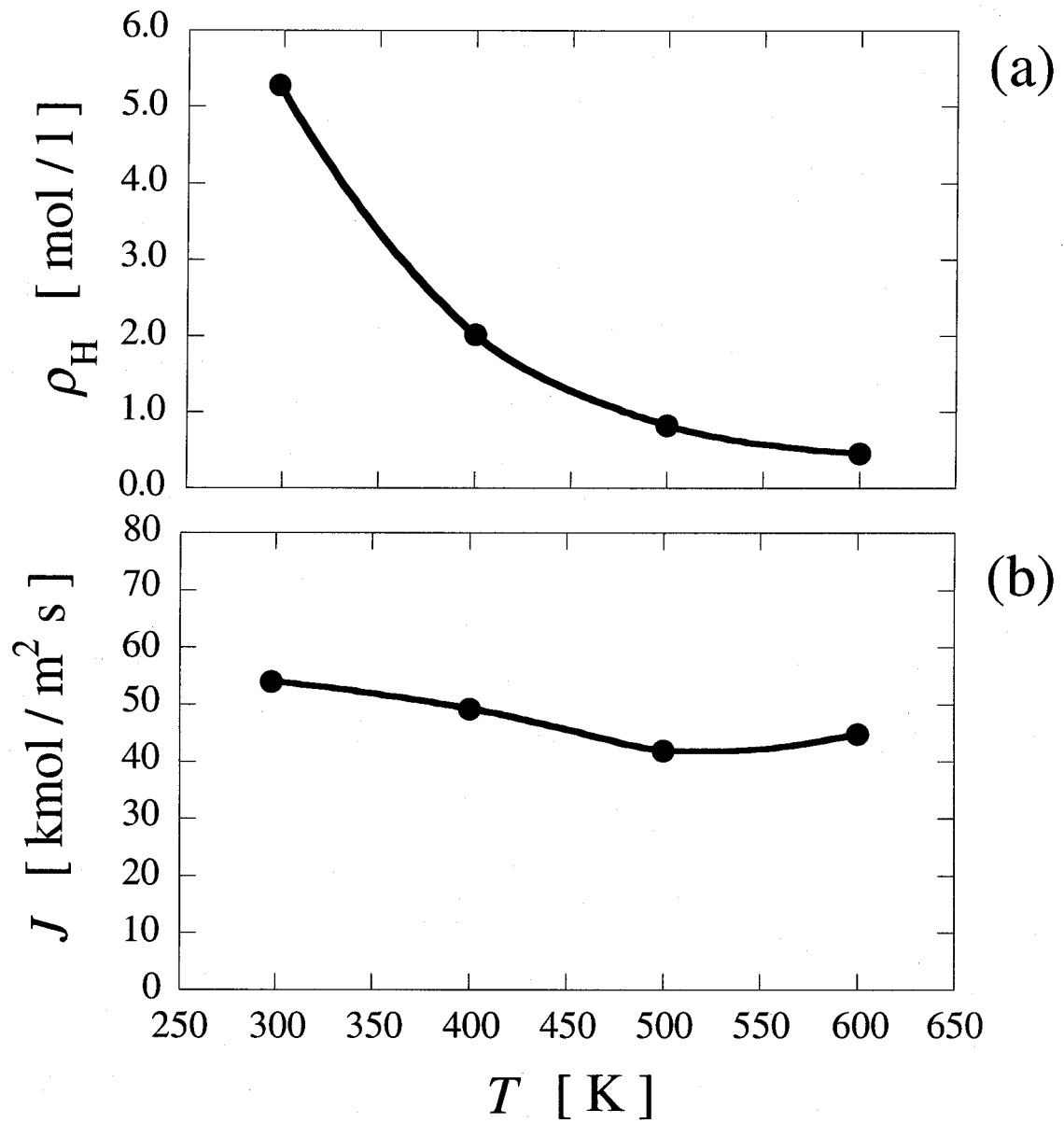
Figure 4-10 Effect of temperature on (a) density at H-region and (b) molar flux
for pure ethane gas through carbon membrane with the belt-like
potential barrier; ΔE_B = 7.38 kJ/mol

Chapter 5
Gas Permeation across Carbon Membranes
with Different Pore Shapes
Composed of Micro-Graphite Crystallites

5.1 Introduction

In the previous chapters, simulations of gas permeation through carbon membranes were carried out for slit-shaped pores composed of homogeneous surfaces (Chapter 2), random heterogeneous surfaces (Chapter 3), or belt-like heterogeneous surfaces (Chapter 4) in order to investigate the effects of surface heterogeneity on permeability and separation factors. The random or belt-like heterogeneous surfaces were made by removing carbon atoms of the first layer of graphite basal planes at random or in a line vertically to the permeating direction, respectively. The simulations were conducted under the assumption that the density at the feed side of the membrane was in equilibrium with the feed gas and that at the exit side was kept at zero corresponding to zero pressure at the permeate side. The simulation results indicated that for the two heterogeneous surfaces adsorption equilibrium at the feed side changed only a little while the permselectivity of methane and ethane through the membranes sharply decreased with increasing surface heterogeneity. It was also suggested that the separation mechanism could change from the adsorption equilibrium control to the permeation rate control with an increase in the potential barriers for surface diffusion.

Real carbon membranes are considered to be composed of parallel stacked carbon sheets (micro-crystallites) and amorphous carbon domains [Kusakabe, 1998], which suggests that there exist many types of pores different in shape.

However, studies on permeation or diffusion through non-slit shaped pores have been limited [Steele, 1997]. In the present work, the author focuses on the pore shape effects on the permeation and separation of gases by using three model pores different in shape, named as diamond, zigzag and straight paths, which are composed of micro-crystallites of graphite basal planes.

5.2 Simulation Method

Figure 5-1 shows a schematic diagram of a simulation cell for the μVT-NEMD method used in the present work. The simulation cell consists of two mirror-image symmetric boxes in order to satisfy the periodic boundary condition in the permeating (x-) direction. Each symmetric box has three regions: two are density-controlling, the H-region (high density) and L-region (low density), and one is free of control, the M-region located between the H-region and the L-region. A membrane is disposed at the center of the M-region. Throughout a simulation run, the density (ρ_H) in the H-region is kept constant at a specified value, which is calculated from the pressure (P_H) and the temperature (T) of a feed gas, while the density (ρ_L) in the L-region is kept at zero (i.e. $P_L = 0$). In the H-region, the insertion and destruction algorithms of the μVT-MC method [Allen and Tildesley, 1987; Frenkel and Smit, 1996] are implemented for maintaining the density to be constant. The chemical potentials of gaseous components, which are necessary in the μVT-MC algorithm, are calculated under the assumption that the gases are ideal. The velocities of inserted molecules are allotted to certain values around the average velocity corresponding to the specified temperature by use of random numbers on the Gaussian distribution. The insertion and destruction operations are carried out for each 20 MD steps. Molecular translation and rotation velocities are rescaled independently after inser-

tion and destruction operations so as to keep the temperature of each region classified as above at a specified value T. Molecules spontaneously move from the H-region to the L-region through a conventional molecular dynamics (leap-frog) algorithm, and a non-equilibrium steady state is obtained in the M-region. The MD time step we adopted was 2.0 fs.

In the present work, three carbon membranes with different pore shape composed of micro-graphite basal planes are proposed as model membranes, and the methane (CH_4) and the ethane (C_2H_6) are chosen as permeation gases. The spherical Lennard-Jones (LJ) potential model is used for the CH_4 molecules, while the C_2H_6 molecules are modeled by two interaction sites located at the center of the carbon atoms. All interactions of molecule-molecule and molecule-carbon atoms of each membrane are described by the 12-6 LJ potential given as

$$\phi_{ij}(r) = 4\varepsilon_{ij}\left[\left(\frac{\sigma_{ij}}{r}\right)^{12} - \left(\frac{\sigma_{ij}}{r}\right)^{6}\right]$$

(5-1)

where r is the distance between interaction centers, i and j, which are allotted among CH_4 molecules, sites of C_2H_6, or carbon atoms, and σ_{ij} and ε_{ij} are potential parameters for the pair i and j. The LJ parameters for CH_4, $-CH_3$ and C are summarized in **Table 5-1** along with a bond length of carbons in the C_2H_6 molecule. The pure LJ parameters for the CH_4 and $-CH_3$ were taken from Jorgensen et al. [1974], and those for the carbon atom were taken from the work of Steele [1974]. The cross parameters were calculated from the Lorentz-Bertherot rule. The cut-off distance for calculations of the intermolecular interactions was set at 3.5 x σ_{CH3}, and the long-range correction was not applied. In the simulations,

the bond length of the C_2H_6 molecule and configurations of the carbon atoms of each membrane are fixed at the initial conditions.

The simulation cell is divided into subcells. The density $(\rho_k^{(L)})$ of component k in the L-th subcell is calculated as

$$\rho_k^{(L)} = \langle N_k^{(L)} \rangle / V_{SC} N_A, \quad (V_{SC} = XL_{SC} \times YL \times ZL) \tag{5-2}$$

where superscript (L) denotes subcell number L, $N_k^{(L)}$ is the number of molecules of component k in the L-th subcell, V_{SC} the volume of a subcell, N_A the Avogadro constant and XL_{SC} the distance in the x-direction of a subcell. The permeation flux $(J_k^{(L)})$ of component k in the L-th subcell is also calculated as

$$J_k^{(L)} = \langle \rho_k \bar{v}_{x,k} \rangle^{(L)} \tag{5-3}$$

where ρ_k is the instantaneous density of component k and $\bar{v}_{x,k}$ the instantaneous average molecular velocity of component k in the x-direction. In addition to the NEMD simulations, equilibrium simulations were conducted to obtain the equilibrium densities of CH_4 and C_2H_6 for the three membranes by setting the densities of the L-regions equal to those of the H-regions.

5.3 Membrane Models

The carbon membranes with three different pore shapes composed of micro-graphite crystallites are made in a computer, i.e. a diamond path (DP), a zigzag path (ZP) and a straight path (SP). **Figures 5-2a** to **5-2c** show cross-sections of pore structures for the three carbon membranes. The DP membrane

shown in Fig. 5-2a has two independent pores with different entrances: a large mouth (pore A) and a small mouth (pore B). The pores of the DP membrane are characterized by diamond-shaped pillar cages connected by linear windows in the x-direction. The cages and windows of the DP membrane may resemble those of zeolites though the latter cages have windows in three directions. The ZP membrane is designed to have zigzag pores whose pore sizes are all the same. The SP membrane has straight pores, which have been called the slit-shaped pores. It is noted that three carbon membranes have pores extended in the y-direction. The minimum pore width (W_p), which is defined as the smallest pore size, is set at 0.5 nm for the three carbon membranes. The distances between pore mouths depicted in Fig. 5-2 are defined as the membrane thickness (XL_{mem}). The values of XL_{mem} for the DP, ZP and SP membranes are 6.3 nm, 4.6 nm and 5.2 nm, respectively. The disparate values for the thickness are due to the different arrangement of micro-graphite crystallites whose unit size was fixed as 2.7 nm x 3.4 nm x 1.3 nm for the DP and ZP membranes.

Figures 5-3a to **5-3c** show potential surfaces for a CH_4 molecule in the three carbon membranes, where the darker the shade, the deeper the potential energy. In Fig. 5-3a for the DP membrane, the potential energies near pore walls are deeper than those in the middle of the cages. When a CH_4 molecule in a cage moves toward the x-direction along the deepest potential surface, there exist a potential barrier at the window that connects the adjacent cages. The deepest potential energy in the DP cage is -15 kJ/mol at the corners (or inside of elbows) of a cage and the largest potential barrier for molecular migration through cages is 9 kJ/mol, where the potential barrier is defined as the difference between the deepest potentials at the windows and the corner. In Fig. 5-3b for the ZP membrane, the potential energies near the surfaces of micro-graphite edges are slightly shallower than those at surfaces of the micro-graphite planes due to

the lower density of carbon atoms, which causes the potential barriers to molecular diffusion inside the ZP membrane. The minimum potential energy in the ZP pore is -16 kJ/mol while the largest potential barrier in the pore is 8 kJ/mol, which is slightly smaller than that of the DP membrane. In Fig. 5-3c for the SP membrane, the potential surface inside the pore is deep and almost flat in the permeating direction. The minimum potential energy in the pore is -16 kJ/mol and the opposite sign becomes the potential barrier when the CH_4 molecules directly go out the membrane, though the potential barrier to go outside the external surface is smaller. There exist the similar barriers in the cases of the DP and ZP membranes at the membrane exit. The potential barriers for a C_2H_6 molecule are larger than those for the CH_4 due to stronger adsorption of the C_2H_6 molecule.

5.4 Results and Discussion

Simulations have been carried out for pure and mixed-gas permeation through three carbon membranes with different pore shapes: the diamond path (DP), the zigzag path (ZP), and the straight path (SP). The pure gases are methane (CH_4) and ethane (C_2H_6), and the mixed-gas is an equimolar mixture of CH_4 (1) and C_2H_6 (2), i.e. $y_1 = 0.5$. In all simulations, the temperature (T) is set at 300 K. The pressure at the H-regions (P_H) for pure gas permeation is set at 0.5 MPa, and for the mixed-gas permeation, the partial pressures of each component at the H-regions ($P_{k,H}$) are set at 0.5 MPa. **Figures 5-4a** to **5-4c** show snapshots for the mixed-gas permeation through the DP, ZP and SP membranes, respectively. In these figures, the permeating direction is from the left to the right-hand side. There are always many molecules gathering at surfaces of the micro-graphite planes, while relatively few molecules are seen at surfaces of the micro-graph-

ite edges. It is noted that the C_2H_6 molecules are enriched in pores much more than the CH_4 molecules since the former molecules are adsorbed more strongly than the latter molecules.

5.4.1 Density profiles

Figures 5-5a and **5-5b** show density profiles in the M-region for (a) pure and (b) mixed-gases permeation of CH_4 and C_2H_6 through the pore A of the DP carbon membrane. The gray region indicates the inside of the membrane and the permeating direction is from the left to the right. Inside the membrane, there are three peaks that correspond to the locations having the deepest potential energies in three cages shown in Figs. 5-2a and 5-3a. The peaks for C_2H_6 (broken lines) are always higher than those for CH_4 (solid lines) due to the difference in the adsorption power. The peaks of CH_4 and C_2H_6 inside the membrane decrease toward the permeate direction. This observation indicates that there are resistances to permeation inside the membrane. In the case of the mixed-gas permeation, the density of CH_4 becomes much lower than that for the pure gas permeation, while the density of C_2H_6 does not change at all. This has been known as the competitive adsorption of strong adsorbed molecules, C_2H_6, which suppresses the adsorption of CH_4.

For pore B, as shown in **Figs. 5-6a** and **5-6b**, the density peaks of C_2H_6 and CH_4 decrease slightly more than those inside pore A, which indicates that permeation resistances inside pore B are larger than those inside pore A. This difference may be ascribed to the asymmetric arrangement of pore walls in the cages of the DP membrane.

Density profiles for the ZP membrane are plotted in **Figs 5-7a** and **5-7b**. The peak shape of the two profiles for CH_4 and C_2H_6 becomes a little complex

due to a combination of two different pore surfaces: the edge-edge and the plane-plane of micro-graphite crystallites. Two density valleys inside the membrane correspond to pore surfaces composed of the micro-graphite edges. A distinguishable feature of the density profiles in the ZP membrane is a sudden decrease in densities of CH_4 and C_2H_6 in the last channel connecting to the membrane exit, which leads to the conclusion that molecules can go out to the external surface of the membrane with very low potential barrier at the pore mouth. As shown in Fig. 5-2b, the pore mouth of the ZP membrane has the plane surface directly extended from the inside channel, which may bring the low potential barriers for molecules to enter or exit. In the case of the mixed-gas permeation, the density of CH_4 becomes much lower than that for the pure gas permeation due to the same reason as in the DP membrane.

Figures 5-8a and **5-8b** present density profiles for the SP membrane. Density of C_2H_6 inside the membrane is always larger than that of CH_4. The most distinguishable feature for the SP membrane is that the density profiles of pure CH_4 and C_2H_6 inside the membrane are almost constant. This may be ascribed to the facts that the potential surface in the pore is almost flat and that the potential barrier for permeation only at the membrane exit. In the case of mixed-gas permeation, novel density profiles of CH_4 and C_2H_6 are observed inside the membrane, i.e. the density of CH_4 decreases toward the membrane exit, while that of C_2H_6 increases. This observation may be explained from two characteristics of the SP membrane: the different potential barriers for CH_4 and C_2H_6 molecules at the membrane exit and the high mobilities of the molecules inside the membrane. The explanation is as follows; among the molecules that reach at the membrane exit, the CH_4 molecules go out more frequently than the C_2H_6 molecules since the potential barrier of the CH_4 is lower than that of the C_2H_6. Therefore, at the exit, the C_2H_6 concentration increases and the CH_4 con-

centration decreases. Since the mobilities of CH_4 and C_2H_6 molecules are high inside the SP membrane, opposite gradients in concentration profiles of CH_4 and C_2H_6 are formed under the condition of the same total concentration inside the membrane.

5.4.2 Permeation resistance and separation factor

The simulation value of permeation flux of component k (J_k) is given by averaging the fluxes of $J_k^{(L)}$, which are calculated through Eq. (5-3), over the subcells in the M-region. The experimental flux J_k is usually expressed by the permeability ($\hat{P}_k$) and the partial pressure difference ($P_{k,H} - P_{k,L}$) at two sides of a membrane.

$$J_k = \frac{\hat{P}_k}{XL_{mem}}\left(P_{k,H} - P_{k,L}\right)$$

(5-4)

An alternative expression for the permeation rate may be the permeation resistance (R) based on the difference of the densities in the membrane ($q_{k,H} - q_{k,L}$) as a driving force.

$$J_k = \frac{1}{R_k}\left(q_{k,H} - q_{k,L}\right)$$

(5-5)

where $q_{k,H}$ and $q_{k,L}$ are the amounts of component k inside the membrane (adsorption) in equilibrium with the feed gas at P_H and the permeate gas at P_L, respectively. In this study, q_k is calculated as

$$q_k = \frac{N_{k,\text{mem}}/N_A}{V_{\text{mem}}}, \quad (V_{\text{mem}} = XL_{\text{mem}} \times YL \times ZL) \tag{5-6}$$

where $N_{k,\text{mem}}$ is the number of molecules of component k inside a membrane, N_A Avogadro's constant, and V_{mem} the membrane volume. The permeation resistance R_k is conventionally related to the permeability $(\hat{P}_k)$ by use of the adsorption equilibrium coefficient K_k $(= q_k/P_k)$ as

$$R_k = \frac{K_k XL_{\text{mem}}}{\hat{P}_k} \tag{5-7}$$

The permeation resistance R_k is the overall resistance consisting of the sum of resistances of the external fluid films, the molecular entrance, the inside diffusion and the molecular exit. The physical significance of the R_k is that it represents the resistance in term of molecular migrations inside the membrane by separating the adsorption equilibrium term included in the permeability.

Table 5-2 summarizes the simulation results for J, q, R and $\hat{P}$ for pure gas permeation along with the ideal permselectivity $(\hat{P}_2/\hat{P}_1)$. The values of q of C_2H_6 are always larger than those of CH_4 due to larger adsorption power, though the values of q for CH_4 and C_2H_6 happen to be almost identical for the SP membrane at the feed gas pressure 0.5 MPa. Furthermore, the q becomes in order of DP < ZP < SP membranes. This is because the average potential energies inside the membranes are deeper in the order of q. For the three membranes, the values of R of C_2H_6 are always larger than those of CH_4, which may be ascribed to the larger mass and the larger potential barriers for C_2H_6 than those for CH_4. For

the DP and ZP membranes, the values of $\hat{P}$ of C_2H_6 are slightly larger than those of CH_4, while the $\hat{P}$ of C_2H_6 is smaller than that of CH_4 for the SP membrane. These results indicate that the ratio of adsorptions q_2/q_1 (or K_2/K_1) is slightly larger than the ratio of permeation resistances R_2/R_1 for the DP and ZP membranes, while the reverse relation is observed for the SP membrane.

Table 5-3 shows J, q and R for mixed-gas permeation along with the separation factors α_{21} and $\alpha_{21}^{(eq)}$ and the resistance ratio R_2/R_1. The separation factor α_{21} is defined by the permeation fluxes (J_1, J_2) and the mole fractions of the feed gas (y_1, y_2) as

$$\alpha_{21} \equiv \frac{J_2/J_1}{y_2/y_1} \tag{5-8}$$

where subscripts 1 and 2 denote CH_4 and C_2H_6, respectively. The adsorption equilibrium separation factor $\alpha_{21}^{(eq)}$ is defined by the equilibrium densities in the membrane (q_k) and the mole fraction in the feed gas (y_k) as

$$\alpha_{21}^{(eq)} = \frac{q_2/q_1}{y_2/y_1} = \frac{K_2}{K_1} \tag{5-9}$$

For each membrane in Table 5-3, it is found that the q of CH_4 is significantly smaller than that of C_2H_6, while the latter values are almost the same as those for pure gas adsorption. The decrease in q of CH_4 is called the competitive adsorption of the C_2H_6 molecule as stated previously.

As for the permeation resistance (R) in the mixed-gas, two factors are considered to influence the R of CH_4: (1) the increase in R due to the increase in

the total density in the pore (total density effect) and (2) the decrease in R due to the decrease in the effective potential barrier for CH_4 (effective potential barrier effect) because the strong adsorption regions might have been occupied by the C_2H_6 molecules. In Table 5-3 for the mixed-gas permeation, the value for R of CH_4 through the DP membrane is almost the same as that of CH_4 given in Table 5-2, which may suggest that the above two factors would compensate for each other. However, for the SP membrane, the value for R of CH_4 in the mixed-gas permeation decreases to the level of four tenths of R in the pure gas permeation. This observation is hard to explain by the above two factors. The third factor that have influenced on the decrease of R of CH_4 for the SP membrane may be the increase in the driving force (i.e. the density gradient) of CH_4 in the pore as shown in Fig. 5-8b. The similar tendency is observed for the R of CH_4 through the ZP membrane in comparison with Tables 5-2 and 5-3.

In all the three membranes, the separation factors, α_{21}, are always smaller than the adsorption equilibrium separation factors, $\alpha_{21}^{(eq)}$, but they are larger than the ideal separation factors, $\hat{P}_2/\hat{P}_1$, as shown in Table 5-2. The separation factor α_{21} defined by Eq. (5-8) is related to the adsorption equilibrium separation factor $\alpha_{21}^{(eq)}$ and the ratio of the permeation resistances R_2/R_1 obtained in the mixed-gas permeation as

$$\alpha_{21} = \frac{K_2/K_1}{R_2/R_1} = \frac{\alpha_{21}^{(eq)}}{R_2/R_1} \qquad (5\text{-}10)$$

The $\alpha_{21}^{(eq)}$ increases in order of DP, ZP and SP membranes, which is the same order of increasing q (or K) of C_2H_6. The simulated values of R_2/R_1 are always greater than unity and the increasing order is shown as DP $\cong$ ZP $<$ SP. There-

fore, the α_{21} cannot be greater than the $\alpha_{21}^{(eq)}$ for the DP, ZP and SP membranes as shown in Table 5-3.

It is important to have some guiding principles for better membrane structures that have higher separation factor α_{21} for a specified mixture composed of component 1 and 2, where component 2 is supposed to be adsorbed more strongly than component 1, i.e. $K_2/K_1 > 1$. The ratio K_2/K_1 for the mixed gas is determined from the adsorption equilibrium where the competitive adsorption becomes important when the total surface coverage in adsorption becomes large as it usually meets at the feed side of a membrane. The ratio R_2/R_1 for the mixed gas may become larger than unity as given in Table 5-3 since the potential barriers for permeation of molecules that are adsorbed more strongly (component 2) are apt to become higher than those of molecules less adsorbed (component 1). Therefore, the first target to get high α_{21} is to decrease the ratio R_2/R_1. When the molecular mass and size of component 2 is larger than those of component 1, as in the case of CH_4 (1) and C_2H_6 (2), a flat surface of pore wall (like the SP membrane) with low potential barrier at the membrane exit (like the ZP membrane) would be desirable. When the kinetic molecular size of component 2 is small, there would be some pore structures that enable the ratio R_2/R_1 to be smaller than unity. Future investigation for such structures would be desirable.

5.5 Summary

The molecular simulations have been performed on the permeation of pure and mixed-gases through three carbon membranes with different pore shapes: the diamond path (DP), the zigzag path (ZP) and the straight path (SP), composed of micro-graphite crystallites. The DP membrane has windows and

cages like zeolites, the ZP membrane has zigzag pores, and the SP membrane has straight pores.

In the case of the DP and ZP membranes, the permeation rates of CH_4 and C_2H_6 were suppressed by the potential barriers inside the membranes, while the permeation of two gases through the SP membrane was controlled by the potential barrier only at the membrane exit.

The permeation rates for the three membranes were described by separating the factors into the adsorption equilibrium and the permeation resistance. In the case of pure gas permeation, the permeation rates for the DP and ZP membranes were influenced more by the adsorption than the permeation resistance, while those for the SP membrane were suppressed by the permeation resistance at the membrane exit. In the case of mixed-gas permeation, the permeation rates for all the three membranes depended on the degree of the competitive adsorption.

In each membrane, the separation factor of the C_2H_6 (2) to the CH_4 (1) were larger than the ideal separation factor, $\hat{P}_2/\hat{P}_1$ and smaller than the adsorption equilibrium separation factor, $\alpha_{21}^{(eq)}$, which were calculated from the densities inside the membrane in equilibrium with the feed gas. This result is ascribed to the suppression of the permeation rate for C_2H_6 gas due to larger potential barriers. Since the separation factor α_{21} is expressed as $\alpha_{21}^{(eq)}/(R_2/R_1)$, a plausible structure of fascinating membrane is suggested so as to have a high value of $\alpha_{21}^{(eq)}$ and simultaneously a small value of R_2/R_1. The significance of the permeation resistance at the membrane exit was also suggested.

Nomenclature

J	= permeation flux	[mol m^{-2} s^{-1}]
K	= adsorption equilibrium coefficient	[mol m^{-3} Pa^{-1}]
N_A	= Avogadro constant	[mol^{-1}]
N_{mem}	= number of molecules inside the membrane	[-]
P	= pressure	[Pa]
$\hat{P}$	= permeability	[mol m m^{-2} s^{-1} Pa]
q	= equilibrium density inside a membrane	[mol m^{-3}]
R	= permeation resistance	[s m^{-1}]
T	= temperature	[K]
$\bar{v}$	= average of molecular velocity	[m]
V_{mem}	= volume of membrane	[m^3]
W_p	= pore width	[m]
XL, YL, ZL	= lengths of simulation cell in x, y and z-directions	[m]
XL_{mem}	= membrane thickness	[m]
y	= molar fraction of feed gas	[-]
α_{21}	= selectivity defined by permeate flux	[-]
ε	= LJ energy parameter	[J]
ρ	= density	[mol m^{-3}]
σ	= LJ size parameter	[m]

<Subscripts>

1	= methane
2	= ethane
H	= H-region of simulation cell
L	= L-region of simulation cell

k $\quad$ = component k

<Superscripts>

(eq) $\quad$ = equilibrium state

(L) $\quad$ = L-th subcell

References

Allen, M.P. and D.J. Tildesley; Computer Simulation of Liquids, Clarendon Press, Oxford, 1987

Frenkel, D. and B. Smit; Understanding Molecular Simulation, From Algorithm to Applications, Academic Press, San Diego, 1996

Jorgensen, W.L., J.D. Madura and C.J. Swenson; "Optimized intermolecular potential functions for liquid hydrocarbons," *J. Am. Chem. Soc.*, **106**, 6638-6646 (1984)

Kusakabe, K., M. Yamamoto and S. Morooka; "Gas permeation and micropore structure of carbon molecular sieving membranes modified by oxidation," *J. Mem. Sci.*, **149**, 59-67 (1998)

Steele, W.A.;The interaction of gases with solid surfaces, Pergamon Press, Oxford, England (1974)

Steele, W.A.; "Computer simulation of surface diffusion in adsorbed phases," *Studies Sur. Sci. Cat.*, **104**, 451-485 (1997)

Table 5-1   Potential parameters for the 12-6 Lennard-Jones potential and a bond length for a C_2H_6 molecule

site or atom	σ [nm]	ε [kJ / mol]	Reference
CH_4	0.3730	1.230	[Jorgensen, 1984]
CH_3	0.3775	0.866	[Jorgensen, 1984]
C (graphite)	0.3400	0.233	[Sttele, 1974]

	Bond length [nm]	Reference
CH_3-CH_3	0.153	[Jorgensen, 1984]

Table 5-2   Permeation fluxes (J), equilibrium densities (q), permeation resistances (R), permeabilities $(\hat{P})$ and ideal separation factors $(\hat{P}_2/\hat{P}_1)$ for pure gas permeation through membranes with the diamond (DP), zigzag (ZP) and straight (SP) paths; $\Delta P = 0.5$ MPa, $T = 300$ K

		J	q	R	$\hat{P}$	$\hat{P}_2/\hat{P}_1$
		[kmol/m² s]	[kmol/m³]	[s/m]	[10⁻¹² mol m/m² s Pa]	[-]
DP	CH_4	6.8	1.0	0.15	86	1.1
	C_2H_6	7.4	2.0	0.27	93	
ZP	CH_4	7.0	1.8	0.26	65	1.3
	C_2H_6	9.0	3.0	0.33	83	
SP	CH_4	16	3.2	0.21	160	0.63
	C_2H_6	10	3.5	0.35	100	

Table 5-3 Permeation fluxes (J), equilibrium densities (q), permeation resistances (R), separation factors (α_{21}, $\alpha_{21}^{(eq)}$) and resistance ratios (R_2/R_1) for mixed-gas permeation through membranes with the diamond (DP), zigzag (ZP) and straight (SP) paths; $\Delta P_k = 0.5$ MPa, $T = 300$ K

		J	q	R	α_{21}	$\alpha_{21}^{(eq)}$	R_2/R_1
		[kmol/m² s]	[kmol/m³]	[s/m]	[-]	[-]	[-]
DP	CH_4	4.4	0.62	0.14	1.5	3.2	2.1
	C_2H_6	6.6	1.9	0.29			
ZP	CH_4	3.7	0.56	0.15	2.4	4.3	2.0
	C_2H_6	8.8	2.6	0.30			
SP	CH_4	4.5	0.39	0.087	2.2	8.3	3.8
	C_2H_6	10	3.3	0.33			
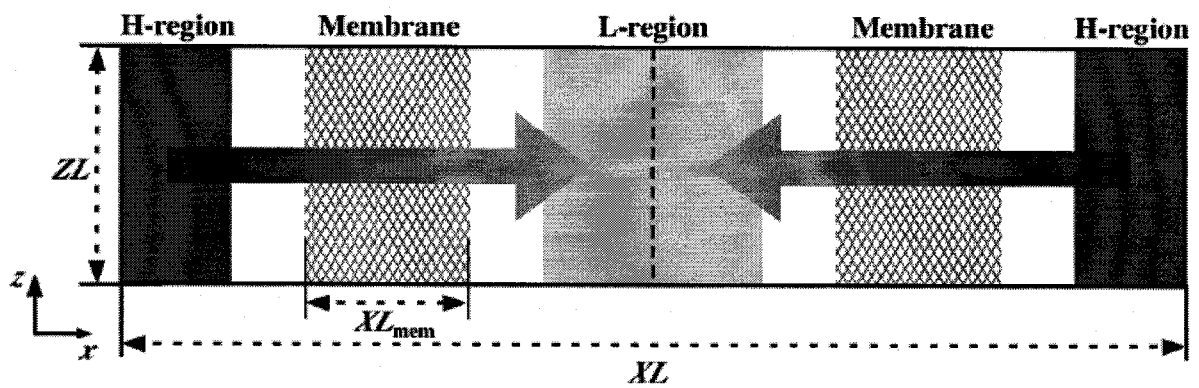
Figure 5-1   Schematic diagram of a simulation cell for the μVT-NEMD method
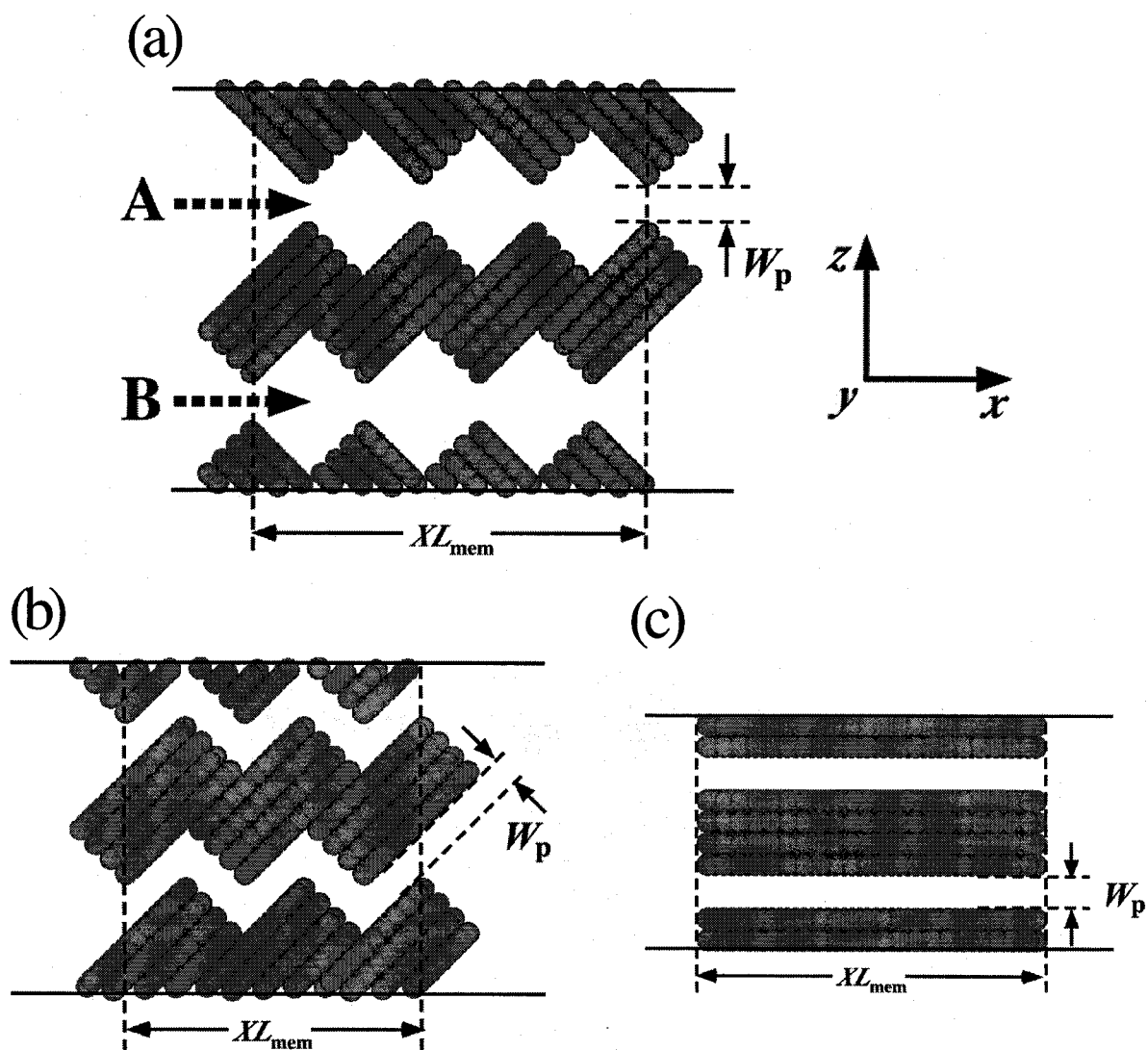
Figure 5-2   Schematic diagrams of membrane models; (a) diamond path, (b) zigzag path and (c) straight path
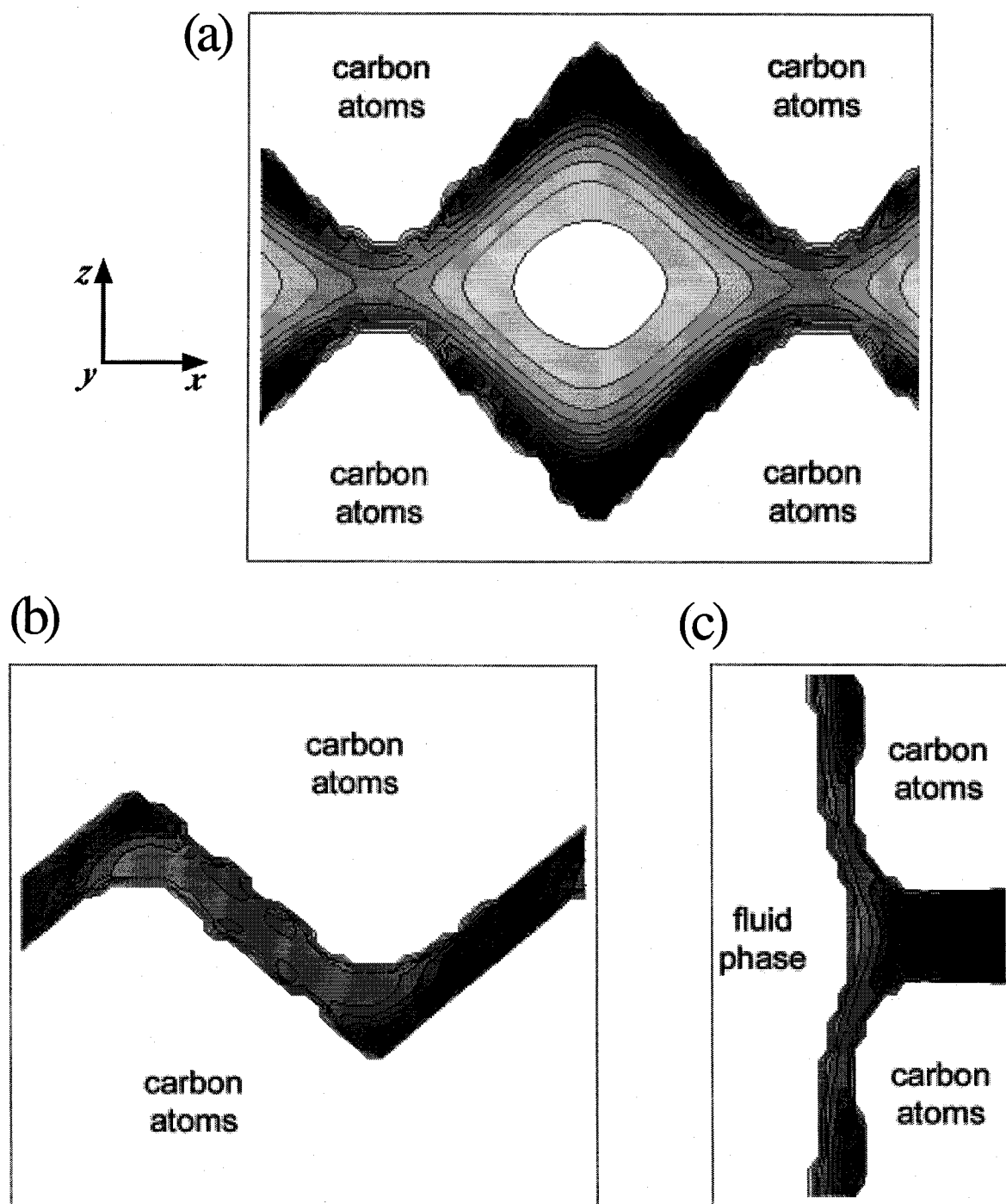
Figure 5-3   Potential energy surfaces for a CH_4 molecule; (a) diamond path, (b) zigzag path and (c) straight path; the darker the shade, the deeper the potential energy
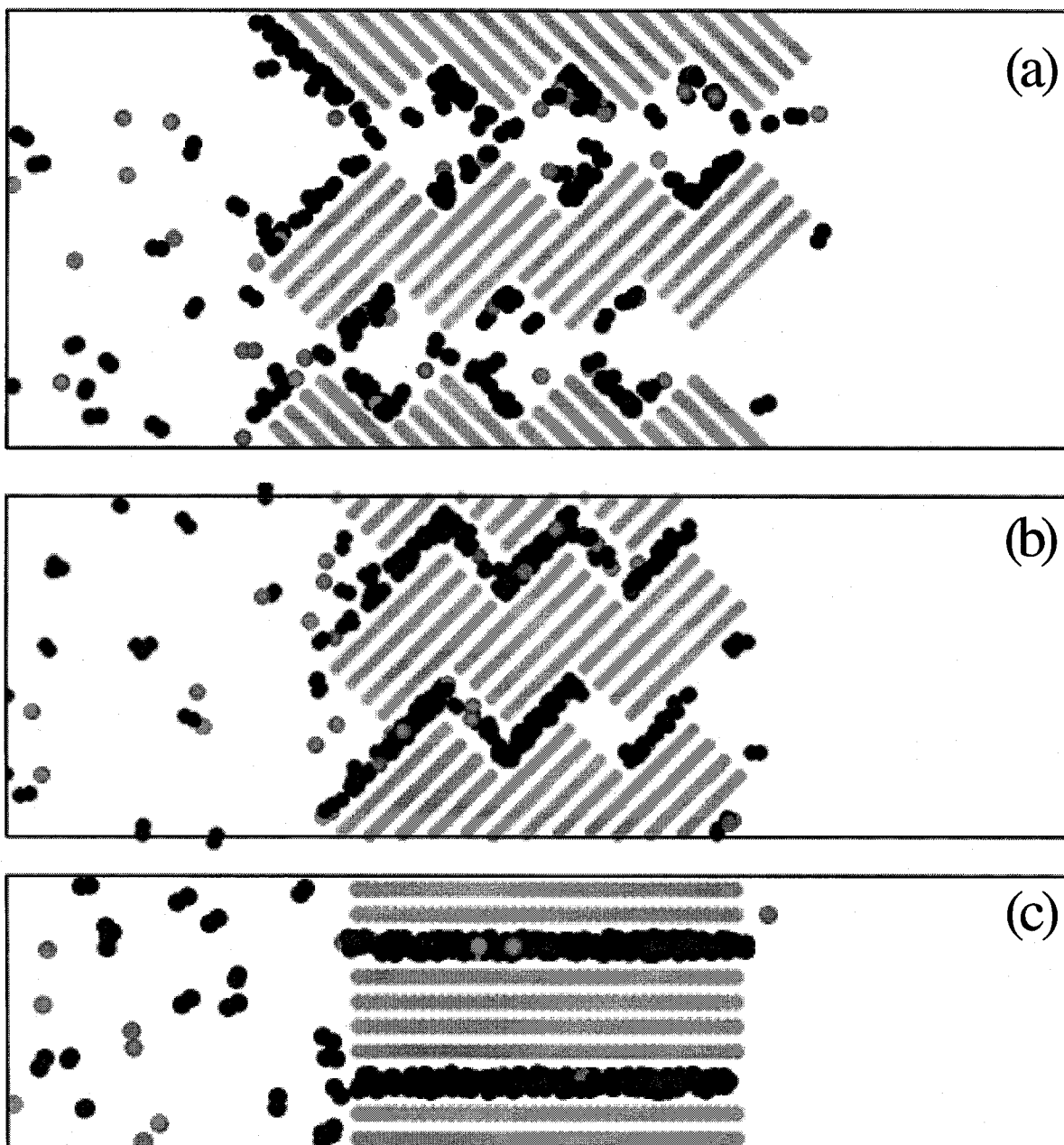
Figure 5-4   Snapshots for mixed gas permeation of CH_4 ($y_1 = 0.5$, gray molecules) and C_2H_6 (black molecules); (a) diamond path, (b) zigzag path and (c) straight path; $\Delta P_k = 0.5$ MPa, $T = 300$ K
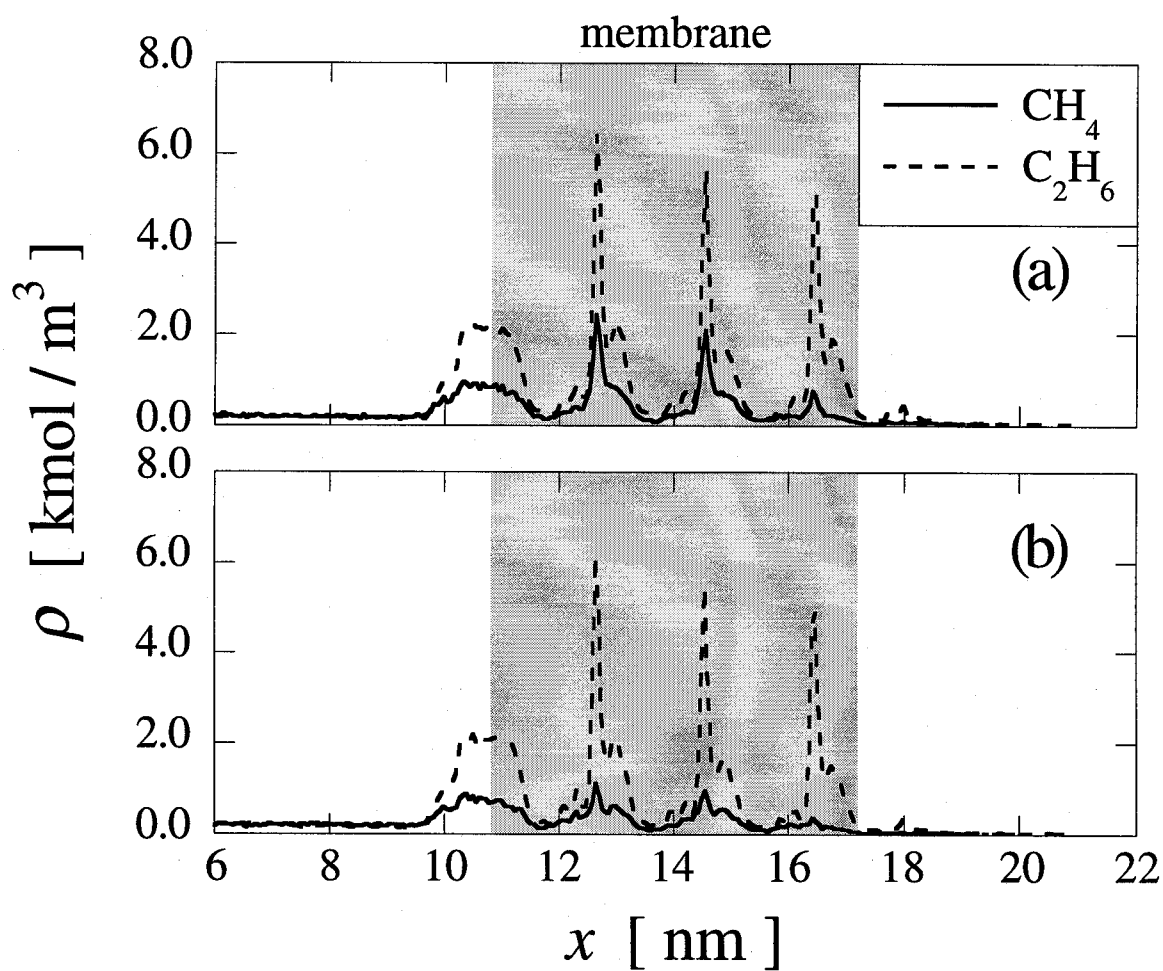
Figure 5-5 Density profiles in the M-region for (a) pure and (b) mixed-gas permeation through pore A of the diamond path membrane; solid lines denote CH_4 and broken lines C_2H_6; $\Delta P = 0.5$ MPa for pure gases, $\Delta P_k = 0.5$ MPa for mixed gas, $T = 300$ K
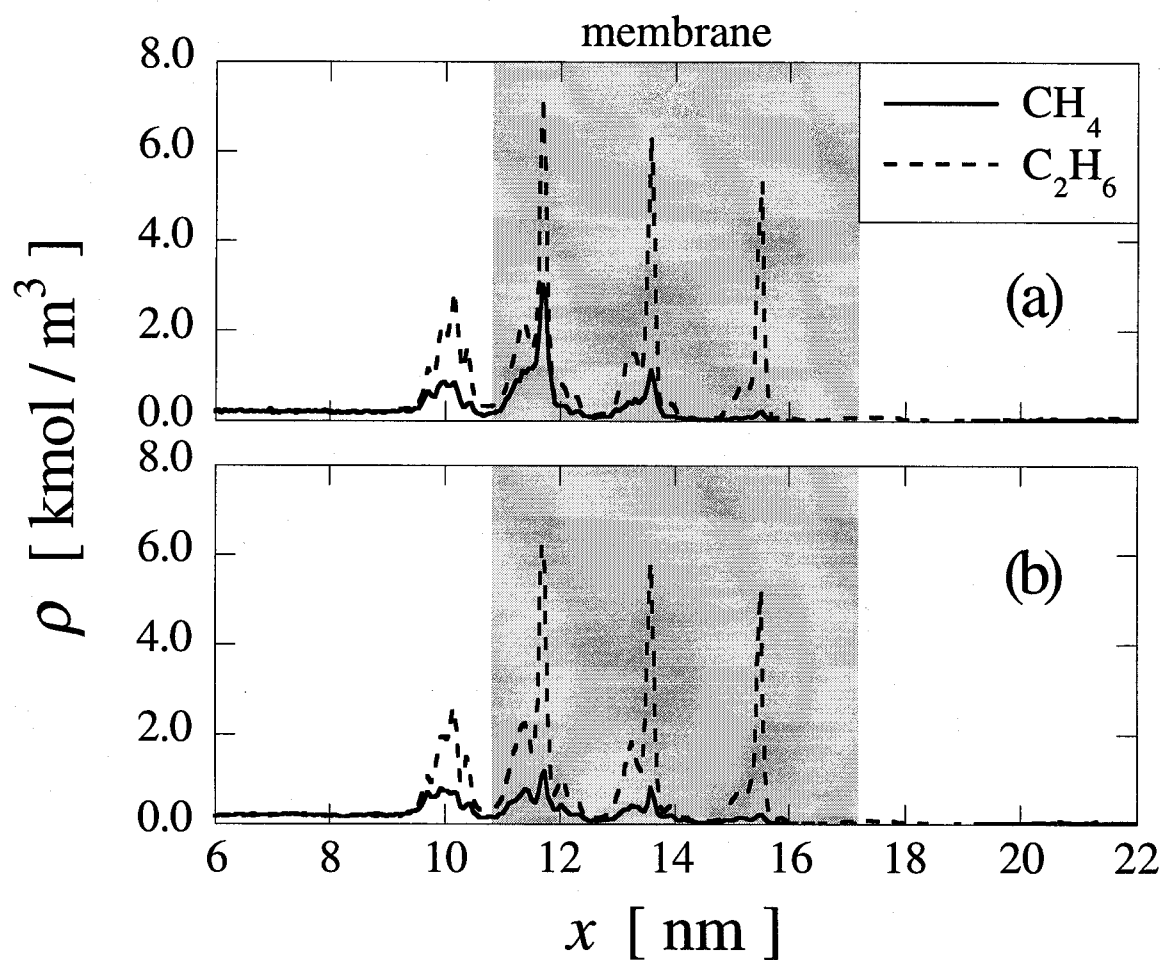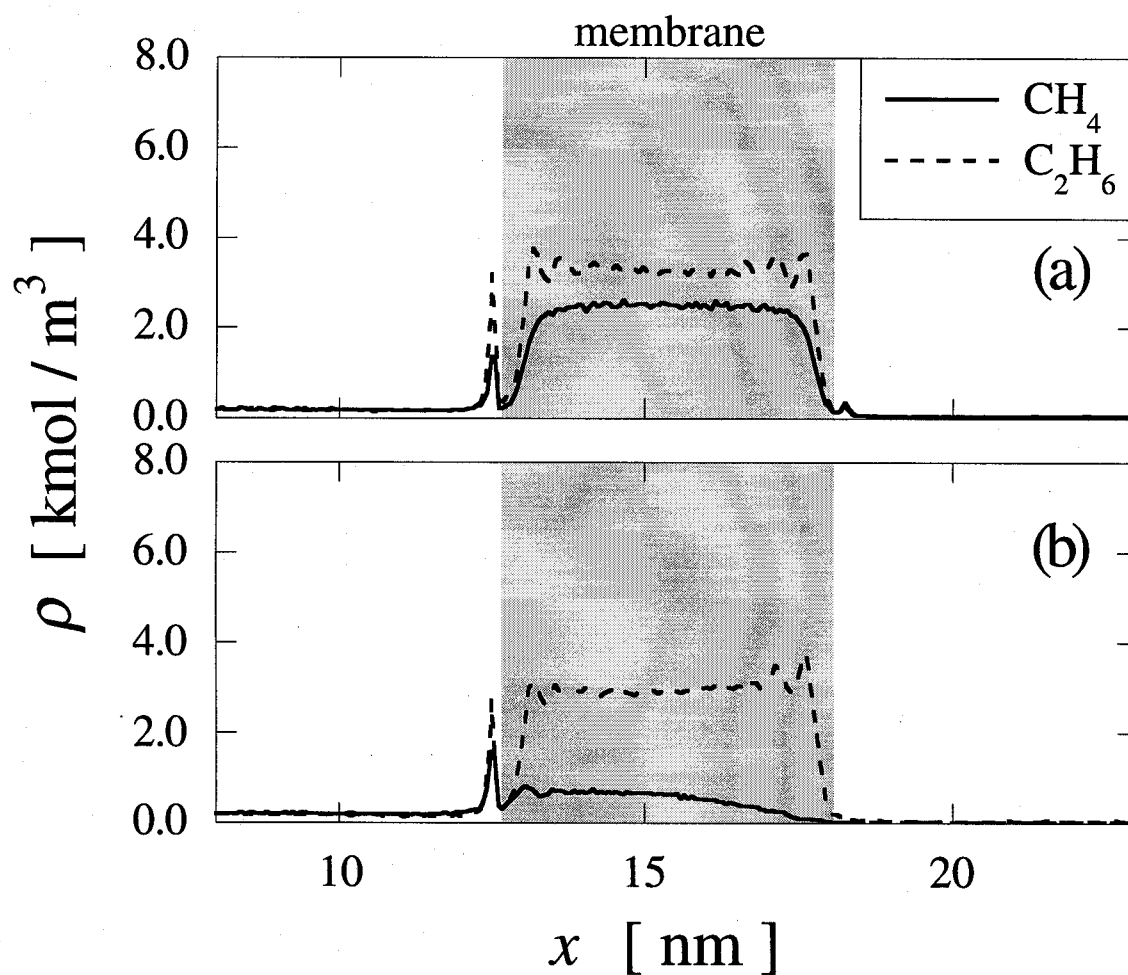
Figure 5-6 Density profiles in the M-region for (a) pure and (b) mixed-gas permeation through pore B of the diamond path membrane; solid lines denote CH_4 and broken lines C_2H_6; $\Delta P = 0.5$ MPa for pure gases, $\Delta P_k = 0.5$ MPa for mixed gas, $T = 300$ K
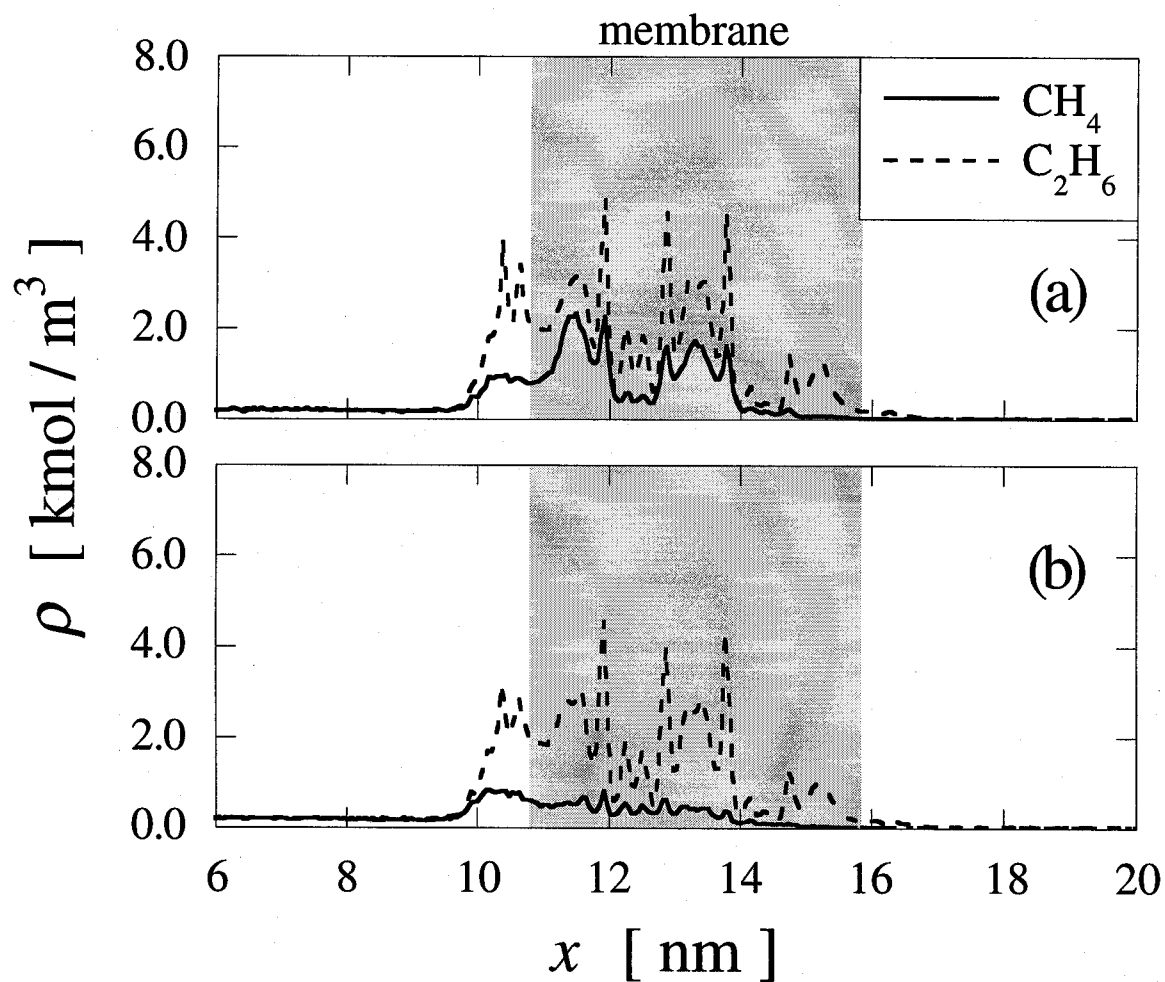
Figure 5-7 Density profiles in the M-region for (a) pure and (b) mixed-gas permeation through the zigzag path membrane; solid lines denote CH_4 and broken lines C_2H_6; $\Delta P = 0.5$ MPa for pure gases, $\Delta P_k = 0.5$ MPa for mixed gas, $T = 300$ K

Figure 5-8 Density profiles in the M-region for (a) pure and (b) mixed-gas
permeation through the straight path membrane; solid lines denote
CH_4 and dotted lines C_2H_6; $\Delta P = 0.5$ MPa for pure gases, $\Delta P_k = 0.5$
MPa for mixed gas, $T = 300$ K

Chapter 6
General Conclusions

Throughout this work, a novel molecular simulation technique, the μVT-NEMD method, was developed and used for studies of gas permeation through carbon membranes with slit-shaped pores different in surface heterogeneity or with pores different in shape.

In Chapter 1, background knowledge for gas permeation through inorganic membranes was first summarized and then the fundamentals of the molecular simulation method, in particular so call the boundary-driven NEMD methods, were reviewed. A short review was provided on the molecular simulation studies of gas permeation through inorganic membranes so far published by the late 1999.

The μVT-NEMD method described in Chapter 2 is one version of the boundary-driven NEMD frameworks proposed by Hafskjold et al. [1993] in the sense that two control regions in the simulation cell are maintained to have different densities but that still the cell is constructed to meet the periodic boundary condition. Some comments will be given here on the present status of the μVT-NEMD method among other boundary-driven NEMD techniques.

The μVT-NEMD method developed in this work resembles three NEMD methods, the DCV-GCMD method by Heffelfinger and Swol [1994], the GCMD method by MacElroy [1994], the GCMD method by Cracknell et al. [1995] since all the methods use the ideas of two control regions and combination of the MD method and the grand canonical MC method. The major differences of the μVT-NEMD method with three other methods are found later to be in two points: (1) constant density (μVT-NEMD) or constant chemical potential (other GCMDs) that is kept in a control region, (2) mirror-image arrangement of two

boxes (μVT-NEMD) or only two control regions (other GCMDs) in the simulation cell. The density control algorithm can save CPU time since the μVTMC operation works only when the number of molecules in the control regions exceeds or decreases from the specified values. Another important advantage of the density control algorithm is found that it enables the simulation of mixed-gas permeation by specifying the total number of molecules at the permeation side where the composition of the permeate gas cannot be specified before permeation started. The simulation performance of the two methods, the μVT-NEMD and the DCV-GCMD methods, were compared in the CPU times and fluctuations in permeation fluxes for a model system of pure silica zeolite [Nitta and Furukawa, 2000].

In Chapter 2, effects of the pore size and temperature on the permeation rate and separation factor were investigated for the slit-shaped carbon membranes with flat pore walls. The dynamic behavior of gas molecules inside the pore was found to be characterized as the selective adsorption followed by the surface flow, which was also observed in Chapters 3 to 5. At a constant feed pressure condition, the permeation fluxes for pure- and mixed-gases decreased with increasing temperature or the pore size because of the decrease in the pore density which was in equilibrium with a feed gas. In the case of mixed-gas permeation, the competitive adsorption played an important role for enhanced selectivity of more adsorptive substance, C_2H_6 in case of a mixture of CH_4 and C_2H_6. The role of the competitive adsorption became more significant as the temperature lowered. In comparison with experimental results, the permeation fluxes were found to be extraordinarily large. The flat surface presumed in the present work was considered as the major reason for the large fluxes.

In Chapter 3, the permeation simulations were carried out for the slit-shaped carbon membrane with random heterogeneous surfaces, which were made

by randomly removing a certain number of carbon atoms of the first graphite basal plane. Permeating molecules were found more frequently in the center region of the pore with an increase in the surface heterogeneity since molecules were apt to climb potential barriers made by heterogeneous sites. The mass-transfer coefficients (k) were found to decrease significantly with a small increase in the surface heterogeneity because of an increase in frequency of direction changes due to molecular collisions onto heterogeneous sites. The k of CH_4 for pure gas permeation was larger than that of C_2H_6, while the k of CH_4 for mixed-gas permeation decreased and became almost identical to that of C_2H_6. This is because CH_4 molecules collided with surrounding C_2H_6 molecules in such a way that the k becomes almost the same as that of C_2H_6. The permeability ($\hat{P}$) decreased with increasing site fraction of the potential barriers (f_b). However, it is still three order times larger in magnitude than the estimated values of $\hat{P}$ for experimentally synthesized carbon membranes. Therefore, real carbon membranes may have structures that provide much larger resistances to permeation of gases than the resistances obtained in the present random heterogeneous surface model.

In Chapter 4, effects of surface heterogeneity on gas permeation were investigated by modeling slit-shaped carbon membranes with belt-like heterogeneous surfaces, which were made by removing carbon atoms on the first layer of the graphite basal plane in a line vertically to the permeation direction. The belt-like heterogeneous surface had unavoidable potential barriers for permeation. In the case of high potential barrier surfaces, many molecules were found in the central region of a pore near the belt-like potential barriers since they had to climb up and down. The permeation resistance (R) increased almost exponentially with an increase in the potential barrier of each gas. The R for C_2H_6 was always larger than that for CH_4 since the potential barrier for C_2H_6 was

larger. In the case of a binary system, the R curves for CH_4 and C_2H_6 were became the same when $\Delta E_B/kT$ was less than 1.0; almost the same result had been obtained in the case of random heterogeneous surfaces. This may indicate that permeation rate of each mixed component are determined by the total density in the pore when the surface heterogeneity is weak, regardless of random or belt-like heterogeneous surfaces. However, in the case of belt-like heterogeneous surfaces, a large decrease in R for CH_4 in the mixed gas permeation was observed when the potential barrier was high.

The separation factor was influenced by the permeation rates in the pore as well as the adsorption equilibrium. The temperature dependence of the permeation flux for C_2H_6 had a minimum point where T was approximately 510 K. This observation may be interpreted as follows: at lower temperatures, the controlling factor of gas permeation may be adsorption density at the feed side, which decreases monotonically with increasing temperature. On the other hand, at higher temperatures, the increase of mass-transfer rate causes the increase in the permeation flux.

In Chapter 5, the permeation of pure and mixed-gases were simulated for three carbon membranes with different pore shapes: diamond path (DP), zigzag path (ZP), and straight path (SP). The DP membrane has windows and cages like zeolites, the ZP membrane has zigzag pores, and the SP membrane has straight pores. The permeation rates for the three membranes were described by separating the factors into the adsorption equilibrium and the permeation resistance. In the case of pure gas permeation, the permeation rates for the DP and ZP membranes were influenced more by the adsorption than the permeation resistance, while those for the SP membrane were suppressed by the permeation resistance at the membrane exit. In the case of mixed-gas permeation, the permeation rates for all the three membranes depended on the degree of the

competitive adsorption.

In each membrane, the separation factor of the C_2H_6 (2) to the CH_4 (1) were larger than the ideal separation factor, $\hat{P}_2/\hat{P}_1$ and smaller than the adsorption equilibrium separation factor, $\alpha_{21}^{(eq)}$, which were calculated from the densities inside the membrane in equilibrium with the feed gas. This result is ascribed to the suppression of the permeation rate for C_2H_6 gas due to larger potential barriers. Since the separation factor α_{21} is expressed as $\alpha_{21}^{(eq)}/(R_2/R_1)$, a plausible structure of fascinating membrane is suggested so as to have a high value of $\alpha_{21}^{(eq)}$ and simultaneously a small value of R_2/R_1. The significance of the permeation resistance at the membrane exit was also suggested.

Reference

Cracknell, R.F., D. Nicholson and N. Quirke; "Direct molecular dynamics simulation of flow down a chemical potential gradient in a slit-shaped micropore," *Phys. Rev. Lett.*, **74**, 2463-2466 (1995)

Nitta, T. and S. Furukawa; "Simulation performance of a non-equilibrium molecular dynamics method using density difference as driving force," *Mol. Sim.*, (2000) *in press*

Hafskjold, B., T. Ikeshoji and S.K. Ratkje; "On the molecular mechanism of thermal diffusion in liquids," *Molec. Phys.*, **80**, 1389-1412 (1993)

Heffelfinger, G.S. and F. van Swol; "Diffusion in Lennard-Jones fluids using dual control volume grand canonical molecular dynamics simulation (DCV-GCMD)," *J. Chem. Phys.*, **100**, 7548-7552 (1994)

MacElroy, J.M.D.; "Nonequilibrium molecular dynamics simulation of diffusion and flow in thin microporous membranes," *J. Chem. Phys.*, **101**, 5274-5280 (1994)

List of Publications

Furukawa, S., T. Shigeta and T. Nitta; "Non-equilibrium molecular dynamics for simulating permeation of gas mixtures through nanoporous carbon membrane," *J. Chem. Eng. Japan*, **29**, 725-728 (1996)

Furukawa, S. and T. Nitta; "Computer simulation studies on gas permeation through nanoporous carbon membranes by non-equilibrium molecular dyanmics," *J. Chem. Eng. Japan*, **30**, 116-122 (1997)

Furukawa, S., K. Hayashi and T. Nitta; "Effects of surface heterogeneity on gas permeation through slit-like carbon membranes by non-equilibrium molecular dynamics simulation," *J. Chem. Eng. Japan*, **30**, 1107-1112 (1997)

Furukawa, S., T. Sugahara and T. Nitta; "Non-equilibrium MD studies on gas permeation through carbon membranes with belt-like heterogeneous surfaces, *J. Chem. Eng. Japan*, **32**, 223-228 (1999)

Furukawa, S. and T. Nitta; "Non-equilibrium molecular dynamics simulation studies on gas permeation across carbon membranes with different pore shape composed of micro-graphite crystallites," *J. Mem. Sci.*, (2000) submitted

Other Related Papers

Furukawa, S. and T. Nitta; "Molecular simulation studies of gas permeation through carbon membranes," *Membrane*, **23**, 80-86 (1998)

Nitta, T. and S. Furukawa; "Simulation performance of a non-equilibrium molecular dynamics method using density difference as driving force," *Mol. Sim.*, (2000) *in press*

Proceedings

Furukawa, S. and T. Nitta; "Computer Simulation of Permeation of Gas Mixtures through Carbon Membranes Using Non-Equilibrium Molecular Dynamics," *The 1996 Int. Congress on Membranes and Membrane Processes*, Yokohama, S-6-2-1 (1996)

Furukawa, S., K. Hayashi and T. Nitta; "Effects of Surface Heterogeneity on Gas Permeations through Slitlike Carbon Membranes by Non-Equilibrium Molecular Dynamics Simulations," *Second Joint China / USA Chemical Engineering Conference*, Beijing (1997)

Furukawa, S., T. Sugahara and T. Nitta; "NEMD Studies of Surface Heterogeneity Effects on Gas Permeation through Carbon Membranes," *Fifth Int. Conference on Inorganic Membranes*, Nagoya, P-131 (1998)

Furukawa, S. and T. Nitta; "Computer Simulation Studies on Gas Permeation through Carbon Membranes at Feed and Permeate Sides," *Fifth Int. Conference on Inorganic Membranes*, Nagoya, P-132 (1998)

Furukawa, S. and T. Nitta; "Non-Equilibrium Molecular Dynamics Simulation Studies on Gas Permeation through Carbon Membranes Composed of Micro-Graphite," *The 1999 Int. Congress on Membranes and Membrane Processes*, Toronto, Poster-59 (1999)

Acknowledgment